UNIVERSITY OF TWENTE.

Faculty of Science and Technology
Faculty of Electrical Engineering, Mathematics and Computer Science

Computational Materials Science
Mathematics of Computational Science

Computational methods in quantum mechanics with applications in spintronic calculations

Author
M.S. Rang

Supervisors
Prof. Dr. P.J. Kelly
Prof. Dr. ir. J.J.W. van der Vegt

April 20, 2020

CONTENTS

1. INTRODUCTION

Energy consumption by and heat dissipation in central processing units (CPUs) are factors limiting the progress of computing technology. The heat produced by CPUs limits the further miniaturization, so even though one can fit billions of transistors on one chip, the total computational power is limited. If one could use the electron spin, rather than its charge, as the carrier of information, the heating problem would be suppressed, as spin currents do not suffer from the same energy dissipation (Joule heating) problem. Another great improvement would be that the energy consumption of the processor units would go down significantly.

This is easier said than done. Electronics based on electron spin, or “spintronics” is a relatively young field, and our lack of knowledge still prohibits any extensive use of spintronics in devices. There are exceptions to this, most notably the giant magnetoresistance (GMR) effect, which is the operating principle of hard disk drives. There are still many unknowns with regard to spin currents in materials, which must be answered if spintronics is to be more widely implemented.

This report focuses on a few spintronic properties of a particular material, namely platinum (Pt). Platinum has a large spin-orbit coupling, which is to say the orbital degrees of freedom couple strongly to the spin degrees of freedom, which in turn means that effects caused by electron spin are more noticeable. This, together with platinum (Pt) being a conductor, makes it a prime example in the study of spintronics. In order to do calculations, the Twente “MTO transport code” is used. Ways to expand and improve the code are also subject matter of this report, in fact, two thirds of the work is focused on these methods, in both a computational and mathematical sense. In the report, the formalisms used in the calculations are discussed first. Then, a few new results are derived, which were subsequently implemented in a computational code. The results section reports the values found through calculation, as well as some computational tests for the newly implemented methods. Finally, the conclusions and recommendations give a final overview of the project, and give recommendations for future research.

2. SCATTERING

In order to do first-principles calculations on solids, which are calculations which do not rely on model parameters, but only on fundamental constants like c and $\hbar$, one must consider the quantum mechanical nature of the electrons involved. As the size of the device (experimental or theoretical) gets smaller, the wave mechanics of the electrons become more and more important. This is what we compute with the Twente MTO Transport code: the possible transport of electrons through a material as the quantum mechanical wave functions of the material allows (or prohibits).

In words, the scheme works like this. We set up an infinite crystal, and compute the Bloch wave functions within it. We use these to construct wave functions which travel in a certain direction. We call this the left lead. Then, we calculate how these constructed waves travel through a scattering region of a given material, as determined by the electronic wave functions determined by the atoms in the material. A crucial property of the scattering region is that in this region we apply disorder of various kinds. It is this disorder which leads to scattering of the electronic states and all of the physics this entails.

Finally, a right lead is constructed, which is similar in its function to the left lead, although instead of incoming waves, here the transmitted waves from the scattering region are matched onto the permissible outgoing states, which are determined by the electronic properties of the right lead. An illustration of the geometry can be seen in fig. 2.1.

In principle, the electronic properties of the leads do not really matter, as they are only used as a basis to construct incoming and outcoming waves. The interesting physics happens in the scattering region, where the behaviour of the electrons is determined by the atomic composition. It is from there that we can extract useful information about the spintronic and electronical properties of the material. An obvious one is the resistivity ρ, which determines how the current through a material depends on the voltage one applies, or vice versa. In terms of spintronics, there are two important parameters, the spin-flip diffusion length l_{sf}, which is a measure of the length an electron on average travels before its spin is flipped, and the spin Hall angle Θ_H, which is the conversion rate of electronic current to perpendicular spin current.

2.1 Formalism

The following is largely borrowed from [9]. Let us consider a two-terminal system for our scattering problem, where the geometry consists of two leads made from a perfect crystal, and a scattering region sandwiched between them, where we apply disorder. The disorder can be of various kinds: thermal (small displacements of the atoms with respect to their equilibrium position), chemical (either as an alloy or in the form of impurities or vacancies) or structural (crystallographic defects,

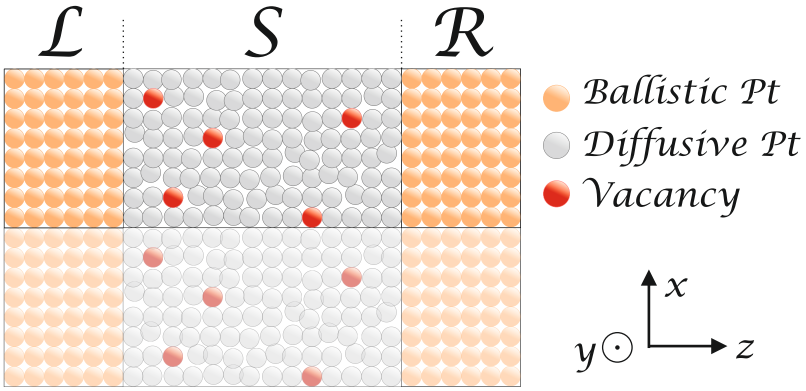

Fig. 2.1: Schematic of the input geometry of the Twente TB-MTO-ASA transport code. The atoms are arranged in a perfect crystal within the left and right leads, but thermal disorder and vacancy defects are present in the scattering region.

grain boundaries, etc.). The scattering matrix is made up of matrices of transmisssion and reflection probability amplitudes as follows

$$\mathbf{S} = \begin{pmatrix} \mathbf{r}_{\mathcal{L}\mathcal{L}} & \mathbf{t}_{\mathcal{R}\mathcal{L}} \\ \mathbf{t}_{\mathcal{L}\mathcal{R}} & \mathbf{r}_{\mathcal{R}\mathcal{R}} \end{pmatrix} , \tag{2.1.1}$$

where the matrix $\mathbf{t}_{\mathcal{R}\mathcal{L}}$ consists of transmission probability amplitudes between each Bloch state in the left lead and in the right lead. This matrix alone is enough to find the conductance of the system, given by the Landauer-Büttiker formalism as

$$G = \frac{e^2}{h} \operatorname{Tr}\{\mathbf{t}\mathbf{t}^\dagger\} . \tag{2.1.2}$$

The transmission and reflection probability amplitude matrices can be found from first principles by Ando's wave-function matching (WMF) technique. The central equation of the formalism is the single-particle time-independent Schrödinger equation.

$$(\mathbf{H} - E\mathbf{I})\,\mathbf{\Psi} = 0 \tag{2.1.3}$$

In the above, E is some specified energy, which in our case will always be the Fermi energy and $\mathbf{I}$ is the identity matrix. The vector $\mathbf{\Psi}$ contains coefficients of the wave function in some localized basis, in our case the tight-binding linear muffin-tin orbitals (TB-LMTOs). The Hamiltonian $\mathbf{H}$ contains all the 'hopping' information, as well as on-site energies. The solutions of the SE in the perfectly crystalline leads are left and right propagating Bloch states and they will function as boundary conditions in the scattering theory.

Leads

The periodicity of the leads allows us to construct the Bloch states if we know the solution of the SE in a single layer, repeated periodically to construct an infinite crystal. We can then write the

Schrödinger equation for the i'th layer within an ideal lead as

$$\left(E\mathbf{I}-\mathbf{H}_i\right)\mathbf{\Psi}_i+\sum_{l=1}^{N}\left(\mathbf{B}_l\mathbf{\Psi}_{i+l}+\mathbf{B}_l^\dagger\mathbf{\Psi}_{i-l}\right)=0\,. \tag{2.1.4}$$

Here $\mathbf{H}_i := \mathbf{H}_{i,i}$ is the on-layer term, consisting of matrix elements between atoms within layer i, $\mathbf{B}_l := \mathbf{H}_{i,i+l}$ is the hopping from layer i to layer $i+l$ and $\mathbf{B}_l^\dagger := \mathbf{H}_{i,i-l}$ is the hopping from layer i to layer $i-l$. Hermiticity of the Hamiltonian and translational invariance guarantee that $\mathbf{H}_{i,i+l}^\dagger = \mathbf{H}_{i+l,i} = \mathbf{H}_{i,i-l}$, which allows us to simplify the expression to just $\mathbf{B}_l$ and its hermitian conjugate.

Furthermore, the translation symmetry allows us to equate the wave function between two neighbouring layers in another way. The Bloch wave function can be decomposed into a cell (or layer, in our case) periodic part, and a complex Bloch factor λ, such that

$$\mathbf{\Psi}_l=\lambda\mathbf{\Psi}_{l-1}\,. \tag{2.1.5}$$

Inserting this in the Schrödinger equation for the leads, we find the generalised eigenvalue problem

$$\left(E\mathbf{I}-\mathbf{H}_0\right)\mathbf{\Psi}_0+\sum_{l=1}^{N-1}\left(\mathbf{B}_l\mathbf{\Psi}_l+\mathbf{B}_l^\dagger\mathbf{\Psi}_{-l}\right)+\mathbf{B}_n^\dagger\mathbf{\Psi}_{-N}=-\lambda\mathbf{B}_n\mathbf{\Psi}_{N-1} \tag{2.1.6}$$

$$\mathbf{\Psi}_l=\lambda\mathbf{\Psi}_{l-1}\,\forall l\in\left[-N+1,N-1\right]\,, \tag{2.1.7}$$

where we have set $i=0$ without loss of generality. The solutions of this equation can be separated into two classes, one with right-going and one with left-going states. Both classes contain propagating Bloch states and non-propagating evanescent states, characterised by the Bloch factor λ. Denoting right-going states by a $+$ and left-going by a $-$, we find that there are only N_o (the number of atom-centered orbital states within each layer) Bloch factors which correspond to a translation of a right- (or left-)going state to a neighboring layer. All other translational Bloch factors correspond to more distant layers, which does not provide any extra information. Each $\lambda(\pm)$ corresponds to N eigenvectors in the generalized eigenvalue problem, so for each $\lambda(\pm)$ we select the one corresponding to $l=0$. This gives us N_o eigenvectors $\mathbf{u}_m(\pm)$, which we gather in an $N_o\times N_o$ matrix

$$\mathbf{U}(\pm)=\begin{pmatrix}\mathbf{u}_1(\pm) & \ldots & \mathbf{u}_{N_o}(\pm)\end{pmatrix}\,. \tag{2.1.8}$$

An arbitrary wave function can be decomposed into any complete basis, and our left-going and right-going wave functions together form the eigenvectors of a Hermitian matrix, so they constitute a complete set. Hence we can write

$$\mathbf{\Psi}=\mathbf{\Psi}(+)+\mathbf{\Psi}(-)=\mathbf{U}(+)\mathbf{C}(+)+\mathbf{U}(-)\mathbf{C}(-)\,, \tag{2.1.9}$$

where the $\mathbf{C}$ vector are the expansion coefficents. This allows us to express the translation of an arbitrary wave function over any number of layers l, since we know the Bloch factors $\lambda(\pm)$ corresponding to each propagating state between neighbouring layers. That is, we have

$$\mathbf{C}_{i+1}(\pm)=\mathbf{\Lambda}(\pm)\mathbf{C}_i(\pm)\,, \tag{2.1.10}$$

where $\mathbf{\Lambda}(\pm)$ is a diagonal matrix with entries $\lambda(\pm)$. Combining the above, we have

$$\begin{aligned}\mathbf{\Psi}_{i+1} &= \mathbf{U}(+)\mathbf{C}_{i+1}(+) + \mathbf{U}(-)\mathbf{C}_{i+1}(-)\\ &= \mathbf{U}(+)\mathbf{\Lambda}(+)\mathbf{C}_i(+) + \mathbf{U}(-)\mathbf{\Lambda}(-)\mathbf{C}_i(-)\\ &= \mathbf{U}(+)\mathbf{\Lambda}(+)\mathbf{U}^{-1}(+)\mathbf{\Psi}_i(+) + \mathbf{U}(-)\mathbf{\Lambda}(-)\mathbf{U}^{-1}(-)\mathbf{\Psi}_i(-)\\ &= \mathbf{F}(+)\mathbf{\Psi}_i(+) + \mathbf{F}(-)\mathbf{\Psi}_i(-)\,.\end{aligned}$$

Here $\mathbf{F}(\pm)$ are Ando's translational matrices

$$\mathbf{F}(\pm) = \mathbf{U}(\pm)\mathbf{\Lambda}(\pm)\mathbf{U}^{-1}(\pm)\,. \tag{2.1.11}$$

For hopping between arbritrary layers, we have

$$\mathbf{\Psi}_{i+l} = \mathbf{F}^l(+)\mathbf{\Psi}_i(+) + \mathbf{F}^l(-)\mathbf{\Psi}_i(-)\,, \tag{2.1.12}$$

which gives us the full solution for the lead. Here $\mathbf{F}^l$ denotes $mathbfF$ to the power l.

2.2 Scattering region

Within the language used earlier, the scattering region takes the form of a giant meta-layer sandwiched between the leads, which each consists of an infinite number of layers. When considering the Schrödinger equation for the system, we note there must be some finite number of lead-layers $N+1$ which directly interact with the scattering region. That is, in the left lead, for any layer with index $-(N+j)$ where $j>0$, we can use the solution found in the last subsection to write

$$\begin{aligned}\mathbf{\Psi}_{\mathcal{L},-N-j} &= \mathbf{\Psi}_{\mathcal{L},-N-j}(+) + \mathbf{\Psi}_{\mathcal{L},-N-j}(-) && (2.2.1)\\ &= \mathbf{F}_{\mathcal{L}}^{-j}(+)\mathbf{\Psi}_{\mathcal{L},-N}(+) + \mathbf{F}_{\mathcal{L}}^{-j}(-)\mathbf{\Psi}_{\mathcal{L},-N}(-) && (2.2.2)\\ &= \left[\mathbf{F}_{\mathcal{L}}^{-j}(+) - \mathbf{F}_{\mathcal{L}}^{-j}(-)\right]\mathbf{\Psi}_{\mathcal{L},-N}(+) + \mathbf{F}_{\mathcal{L}}^{-j}(-)\mathbf{\Psi}_{\mathcal{L},-N}\,, && (2.2.3)\end{aligned}$$

where wave function in the left lead in the $-N-j$'th layer is denoted by $\mathbf{\Psi}_{\mathcal{L},-N-j}$. Similarly, we will use the subscript $\mathcal{S}$ to denote the scattering region and $\mathbf{R}$ for the right lead.

For the layers with index $n \in [-N, 0]$ of the left lead, the Schrödinger equation reads

$$(E\mathbf{I} - \mathbf{H}_{\mathcal{L},n})\,\Psi_{\mathcal{L},n} + \sum_{l=1}^{-n}\mathbf{B}_{\mathcal{L},l}\Psi_{\mathcal{L},n+l} + \mathbf{B}_{\mathcal{LS},n}\Psi_S + \sum_{l=1}^{N}\mathbf{B}_{\mathcal{L},l}^{\dagger}\Psi_{\mathcal{L},n-l} = 0\,. \tag{2.2.4}$$

The first term contains the on-layer contributions, the second term is the hopping from layer n to all layers with a higher (closer to 0) index, the third term is all hopping from layer n to the scattering region, and the last term is any hopping from layer n to any layer with a lower (i.e. more negative) index. It is within this term that we can use (2.2.3). The Schrödinger equation becomes

$$\begin{aligned}&(E\mathbf{I} - \mathbf{H}_{\mathcal{L},n})\,\mathbf{\Psi}_{\mathcal{L},n} + \sum_{l=1}^{-n}\mathbf{B}_{\mathcal{L},l}\mathbf{\Psi}_{\mathcal{L},n+l} + \mathbf{B}_{\mathcal{LS},n}\mathbf{\Psi}_S +\\ &+ (1-\delta_{N,-n})\sum_{l=1}^{N+n}\mathbf{B}_{\mathcal{L},l}^{\dagger}\mathbf{\Psi}_{\mathcal{L},n-l} + \sum_{l=N+n+l}^{N}\mathbf{B}_{\mathcal{L},l}^{\dagger}\mathbf{F}_{\mathcal{L}}^{-l+N+n}(-)\mathbf{\Psi}_{\mathcal{L},-N} \qquad (2.2.5)\\ &= -\sum_{l=N+n+1}^{N}\mathbf{B}_{\mathcal{L},l}^{\dagger}\left[\mathbf{F}_{\mathcal{L}}^{-l+N+n}(+) - \mathbf{F}_{\mathcal{L}}^{-l+N+n}(-)\right]\mathbf{\Psi}_{\mathcal{L},-N}(+)\,,\end{aligned}$$

where $\mathbf{B}_{\mathcal{LS},n}$ is the hopping matrix from layer n to the scattering region. The Schrödinger equation for the right lead is similar, but simpler, since in the right lead, only right-moving states can exist, so for any layer with index $N+j$ where $j > 0$, we have

$$\mathbf{\Psi}_{\mathcal{R},N+j} = \mathbf{F}_{\mathcal{R}}^{j}(+)\mathbf{\Psi}_{\mathcal{R},N} \,. \tag{2.2.6}$$

The Schrödinger equation for the layers of the right lead with index $n < N+j$ becomes

$$\begin{aligned}(E\mathbf{I} - \mathbf{H}_{\mathcal{R},n}) + \sum_{l=1}^{n} \mathbf{B}_{\mathcal{R},l}^{\dagger}\mathbf{\Psi}_{\mathcal{R},n-l} + \mathbf{B}_{\mathcal{RS},n}^{\dagger}\mathbf{\Psi}_{\mathcal{S}} + (1-\delta_{N,n}) \sum_{l=1}^{N-n} \mathbf{B}_{\mathcal{R},l}\mathbf{\Psi}_{\mathcal{R},n+l} \\ + \sum_{l=N-n+1}^{N} \mathbf{B}_{\mathcal{R},l}\mathbf{F}_{\mathcal{R}}^{l-N+n}(+)\mathbf{\Psi}_{\mathcal{R},N} = 0 \,.\end{aligned} \tag{2.2.7}$$

Finally, the Schrödinger equation for the states within the scattering region is

$$(E\mathbf{I} - \mathbf{H}_{\mathcal{S}})\,\mathbf{\Psi}_{\mathcal{S}} + \sum_{l=0}^{N-1} \left[\mathbf{B}_{\mathcal{LS},l}^{\dagger}\mathbf{\Psi}_{\mathcal{L},-l} + \mathbf{B}_{\mathcal{RS},l}\mathbf{\Psi}_{\mathcal{R},l}\right] = 0 \,. \tag{2.2.8}$$

These are all the equations needed to fully solve the system, with one final boundary condition being

$$\mathbf{\Psi}_{\mathcal{L},-N}(+) = \mathbf{U}_{\mathcal{L}}(+) \,. \tag{2.2.9}$$

That is, the incoming states are the right-going eigenstates of the left lead. The final set of equations is an inhomogeneous set of linear equations which is relatively sparse, thanks to the TB-LMTOs. The reflection and transmission matrices can be extracted as

$$\mathbf{\Psi}_{\mathcal{L},-N}(-) = \mathbf{U}_{\mathcal{L}}(-)\mathbf{r} \tag{2.2.10}$$

$$\mathbf{\Psi}_{\mathcal{R},N}(+) = \mathbf{U}_{\mathcal{R}}(+)\mathbf{t} \,, \tag{2.2.11}$$

or rather, in usable form

$$\mathbf{r} = \mathbf{U}_{\mathcal{L}}^{-1}(-)\left[\mathbf{\Psi}_{\mathcal{L},-N} - \mathbf{U}_{\mathcal{L}}(+)\right] \tag{2.2.12}$$

$$\mathbf{t} = \mathbf{U}_{\mathcal{R}}^{-1}(+)\mathbf{\Psi}_{\mathcal{R},N} \,. \tag{2.2.13}$$

The reflection matrix contains two components, where the transmission matrix only contains one. The reason for this is that while the right lead only contains right-going states, the left lead contains the incoming states as well as the reflected ones.

2.3 Currents

One vital part of the transport code is the interatomic currents, as well as the layer-averaging algorithms it contains. Through the hopping Hamiltonians (which we have to construct anyway), we can in a remarkably simple fashion extract the interatomic (spin) currents from the scattering region. For more details, see [13].

Let us consider an atom P within the scattering region. The TB-LMTO method has as its basis a set of localised orbitals, such that we can associate every basis function with one particular atom.

We write all basis functions localised on P as $|\Psi_P\rangle$. The current at P is simply equal to the change of the electron density in time

$$\begin{aligned}\frac{\partial}{\partial t}n_P = \frac{\partial}{\partial t}\langle\Psi_P|\Psi_P\rangle &= \frac{\partial}{\partial t}\int \Psi_P(\mathbf{r})^\dagger\Psi_P(\mathbf{r})d\mathbf{r}\\ &= \int \frac{\partial\Psi_P(\mathbf{r})^\dagger}{\partial t}\Psi_P(\mathbf{r})d\mathbf{r} + \int \Psi_P(\mathbf{r})^\dagger\frac{\partial\Psi_P(\mathbf{r})}{\partial t}d\mathbf{r}\\ &= \left\langle \frac{\partial}{\partial t}\Psi_P\middle|\Psi_P\right\rangle + \left\langle \Psi_P\middle|\frac{\partial}{\partial t}\Psi_P\right\rangle\,.\end{aligned}$$

Now remembering the time dependent Schrödinger equation, which is

$$i\hbar\frac{\partial}{\partial t}\Psi = \hat{H}\Psi\,, \tag{2.3.1}$$

we find an equation for the charge current, solely in terms of the Hamiltonian $\hat{H}$ and the wave function Ψ_P

$$\frac{\partial}{\partial t}n_P = \frac{1}{i\hbar}\left[\langle\Psi_P|\hat{H}|\Psi\rangle - \langle\Psi|\hat{H}|\Psi_P\rangle\right]\,. \tag{2.3.2}$$

We also know, by conservation of charge, that the current at atom P must necessarily equal the sum of all currents between atoms P and every other atom, or in equation form

$$\frac{\partial}{\partial t}n_P = \sum_Q j_c^{PQ}(\Psi_P,\Psi_Q)\,, \tag{2.3.3}$$

and indeed, the equation for the current (2.3.2) fits such a form, when we decompose the Hamiltonian $\hat{H}$ into atom-to-atom blocks $\hat{H}_{PQ}$

$$j_c^{PQ} = \frac{1}{i\hbar}\left[\langle\Psi_P|\hat{H}_{PQ}|\Psi_Q\rangle - \langle\Psi_Q|\hat{H}_{QP}|\Psi_P\rangle\right]\,. \tag{2.3.4}$$

The derivation of the expression for the spin currents is very similar. The spin density on each atom is $s_{\alpha,P} := \langle\Psi_P|\sigma_\alpha|\Psi_P\rangle$, with σ_α the Pauli matrices, so that the spin currents become

$$\frac{\partial}{\partial t}s_{\alpha,P} = \left\langle\frac{\partial}{\partial t}\Psi_P\middle|\sigma_\alpha|\Psi_P\rangle + \langle\Psi_P|\sigma_\alpha\middle|\frac{\partial}{\partial t}\Psi_P\right\rangle \tag{2.3.5}$$

$$= \frac{1}{i\hbar}\left[\langle\Psi_P|\sigma_\alpha\hat{H}|\Psi\rangle - \langle\Psi|\hat{H}\sigma_\alpha|\Psi_P\rangle\right]\,, \tag{2.3.6}$$

which we decompose into interatomic spin currents in the exact same way

$$j_{s\alpha}^{PQ} = \frac{1}{i\hbar}\left[\langle\Psi_P|\sigma_\alpha\hat{H}_{PQ}|\Psi_Q\rangle - \langle\Psi_Q|\hat{H}_{QP}\sigma_\alpha|\Psi_P\rangle\right]\,. \tag{2.3.7}$$

We note that these currents are actually current *densities*, so to find the actual current, we multiply the current densities, which we gather in a tensor $\tilde{j}^{PQ}$ by a volume $V_{PQ} = A_{PQ}|\mathbf{d}_{PQ}|$, where A_{PQ} is an arbitrary cross section which cancels in the integration, $\mathbf{d}_{PQ}$ is the vector pointing from P to Q and $\mathbf{j}^{PQ} = (j_{sx}^{PQ}, j_{sy}^{PQ}, j_{sz}^{PQ}, j_c^{PQ})^T$ is the currents vector.

$$\tilde{j}^{PQ}V_{PQ} = \begin{pmatrix} j_{sx}^{PQ}d_x & j_{sx}^{PQ}d_y & j_{sx}^{PQ}d_z\\ j_{sy}^{PQ}d_x & j_{sy}^{PQ}d_y & j_{sy}^{PQ}d_z\\ j_{sz}^{PQ}d_x & j_{sz}^{PQ}d_y & j_{sz}^{PQ}d_z\\ j_c^{PQ}d_x & j_c^{PQ}d_y & j_c^{PQ}d_z \end{pmatrix} = \mathbf{j}^{PQ}\otimes\mathbf{d}_{PQ} \tag{2.3.8}$$

When we group together a group of atoms and call them a layer, there are plenty of interatomic currents between two layers. To ensure that we divide up the current properly between the layers, we define a parameter

$$\beta_{QP,l} = \begin{cases} 0 & \text{if Q is inside layer } l \\ d_{Q,l}/d_z & \text{if Q is outside layer } l \end{cases}, \tag{2.3.9}$$

where $d_{Q,l}$ is the distance in the z direction between atom Q and the outer boundary of layer l, and d_z is the distance in the z direction between Q and P. For the spin currents, we need to linearly interpolate between $j^{PQ}_{s\alpha}$ and $j^{QP}_{s\alpha}$ since the spin current is in general not conserved between two atoms.

$$\mathbf{j}^{PQ}(\lambda) = \lambda \mathbf{j}^{PQ} - (1-\lambda)\mathbf{j}^{QP} \qquad \lambda \in [0,1] \tag{2.3.10}$$

The part of $\tilde{j}^{PQ}V_{PQ}$ that belongs to layer l then equals

$$\int_{\beta_{QP,l}}^{1-\beta_{PQ,l}} \mathbf{j}^{PQ}(c) \otimes \mathbf{d}_{PQ} dc = \frac{1}{2}\left[(1-\beta_{PQ,l})^2 - \beta^2_{QP,l}\right] \mathbf{j}^{PQ} \otimes \mathbf{d}_{PQ} + \frac{1}{2}\left[(1-\beta_{QP,l})^2 - \beta^2_{QP,l}\right] \mathbf{j}^{QP} \otimes \mathbf{d}_{QP} \,. \tag{2.3.11}$$

The average current density tensor within layer l is

$$\tilde{j}_l = \frac{1}{V_l} \sum_{P,Q} \frac{1}{2}\left[(1-\beta_{PQ,l})^2 - \beta^2_{QP,l}\right] \mathbf{j}^{PQ} \otimes \mathbf{d}_{PQ} \,. \tag{2.3.12}$$

Dividing the scattering region into layers seems unnecessary, but is actually very important to obtain reasonable currents. Obtaining accurate interatomic currents is a very powerful tool, which allows us to directly observe spin currents. The small basis set resulting from the TB-LMTOs allows us to go to very large systems of thousands of atoms, which means we can calculate spin currents for length scales resembling real experimental samples, albeit only in one cartesian direction.

3. LMTO FORMALISM

This section of the thesis is a summary of the physics and mathematics that go into the code. None of the derivations done here were originally done by the author, and only serve to illuminate the black box that is the LMTO-ASA transport code. Nevertheless, it is important to understand what is going on under the hood when one wants to perform high-fidelity calculations. When implementing new features into the code, this becomes even more important. This section is structured as follows. First, in section 3.1, we introduce the reader to the concept of a Muffin-Tin Orbital (MTO), which form a set of basis functions for the quantum mechanical wave function we use to perform calculations. A short section on Spin-Orbit Coupling (SOC) section 3.3 follows, which we treat as a perturbation on the MTO Hamiltonian. The SOC interaction is an essential to the computation of spintronic properties, as without it, the spin degrees of freedom are independent of the orbital degrees of freedom. Finally, in section 3.4 we describe the Exact Muffin-Tin Orbital (EMTO) basis, which is the basis used in the latest version of the transport code.

3.1 Muffin-tin Orbitals

We want to be able to study diffusive transport at room temperature in transition metals (TM) and TM heterostructures, which will translate into being able to consider "scattering regions" containing 10000 atoms and more. We need to describe the quantum mechanical wave function Ψ in a minimal basis set, otherwise the scattering problem becomes intractable. Furthermore, it is convenient to have a localised basis, i.e. every element of the basis set can be associated with one atom. This way the range of interaction is limited to nearest neighbours or next-nearest neighbours only, which results in a Hamiltonian that is sparse. This will speed up the computations as compared to a dense Hamiltonian, since there exist sparse-matrix solvers that are much more efficient than their dense-matrix counterparts.

Tight-binding muffin-tin orbitals (TB-MTOs) [2] satisfy both requirements. To generate the basis, one divides the crystal into muffin tin (MT) spheres, and an interstitial region. Within the MT spheres, the potential is assumed to be spherically symmetric, so that we can solve the Schrödinger equation through separation of variables. In the interstitial region, the potential is assumed to be constant (zero, in the so-called "atomic sphere approximation" to be discussed below). The equation which governs all behaviour within the one-electron formalism is the time-independent Schrödinger equation (TISE)

$$\frac{-\hbar^2}{2m}\nabla^2\psi + \hat{V}\psi = E\psi\,. \tag{3.1.1}$$

The SE can then be separated in real space between the MT spheres and the interstitial. The ∇^2 operator is the Laplacian. Within the assumption that the potential $V(r,\theta,\phi) = V(r)$ is spherically symmetric, we can separate the angular variables θ, ϕ from the radial variable r. That is, we can write the wave function ψ as a product of radial and angular parts.

$$\psi(\mathbf{r}) = \phi(r)Y(\theta,\phi)\,. \tag{3.1.2}$$

The Laplacian in spherical coordinates is

$$\nabla^2 f = \frac{1}{r}\frac{\partial^2}{\partial r^2}(rf) + \frac{1}{r^2\sin\theta}\frac{\partial}{\partial\theta}\left(\sin\theta\frac{\partial f}{\partial\theta}\right) + \frac{1}{r^2\sin^2\theta}\frac{\partial^2 f}{\partial\phi^2}\,.$$

Omitting the algebra (it is straightforward but lengthy) we can separate the equation into a left hand side, which is only dependent on r, and a left hand side, which is only dependent on θ,ϕ. This leads to two equations, a radial one and an angular one.

$$\frac{1}{R(r)}\left[\frac{d}{dr}\left(r^2\frac{dR(r)}{dr}\right) + \frac{2mr^2}{\hbar^2}\left(E - V(r)\right)R(r)\right] = \lambda\,, \tag{3.1.3}$$

$$-\frac{\partial Y(\theta,\phi)}{\partial\phi^2} = \sin\theta\frac{\partial}{\partial\theta}\left(\sin\theta\frac{\partial Y(\theta,\phi)}{\partial\theta}\right) + \lambda\sin^2\theta\, Y(\theta,\phi)\,. \tag{3.1.4}$$

Employing separation of variables again, we have $Y(\theta,\phi) = \Theta(\theta)\Phi(\phi)$, which we use to rewrite the angular equation to

$$-\frac{1}{\Phi(\phi)}\frac{\partial^2\Phi(\phi)}{\partial\phi^2} = \frac{1}{\Theta}\left(\sin\theta\frac{\partial}{\partial\theta}\left(\sin\theta\frac{\partial\Theta(\theta)}{\partial\theta}\right) + \lambda\sin^2\theta\,\Theta(\theta)\right) = m^2\,.$$

We have chosen to write the arbitrary constant as m^2 so we have a simple form for $\Phi(\phi)$:

$$\frac{\partial\Phi(\phi)}{\partial\phi^2} + m^2\Phi(\phi) = 0$$

The spherical system gives a boundary condition for this equation as $\Phi(\phi+2\pi) = \phi(\phi)$. This is one of the first differential equations one learns to solve as an undergraduate student. The solutions are given by

$$\Phi(\phi) = e^{im\phi}\,.$$

The boundary condition gives $\Phi(\phi+2\pi) = e^{im(\phi+2\pi)} = \Phi(\phi) = e^{im\phi}$, so the only allowed values of m are integers, since those are the only values that satisfy $e^{2\pi mi} = 1$. The solutions to the differential equation are quantised. Within quantum mechanics literature, m is known as the magnetic quantum number. Having found a solution for $\Phi(\phi)$, we can now solve for $\Theta(\theta)$. Inserting the solution and rewriting gives

$$\frac{1}{\sin\theta}\frac{\partial}{\partial\theta}\left(\sin\theta\frac{\partial\Theta(\theta)}{\partial\theta}\right) + \left(\lambda - \frac{m^2}{\sin^2\theta}\right)\Theta(\theta) = 0\,. \tag{3.1.5}$$

The constant λ must be a positive integer for this equation to be solvable. In fact, we have $\lambda = l(l+1)$, where l is the angular quantum number, which represents the angular momentum. l also restricts the allowed values of m as $m = -l, -l+1, ..., l-1, l$. Roughly speaking, one can say that l determines the amplitude of the angular momentum, and m determines where it points.

Finally, we can write down the radial Schrödinger equation, since we have an expression for λ we can put into the right hand side of (3.1.3).

$$\left[\frac{d}{dr}r^2\frac{d}{dr}+\frac{2mr^2}{\hbar^2}\left(E-V(r)\right)-l(l+1)\right]R(r)=0 \tag{3.1.6}$$

The solutions to the angular equations (3.1.5) are very well known. They are the so-called spherical harmonics $Y_{lm}(\theta,\phi)$. The radial SE will be solved numerically from the origin out, up to the muffin-tin radius.

The solution of the TISE for a spherically symmetric potential can be constructed as the sum of products of spherical harmonic and solutions to the radial Schrödinger equation. This is a vital step in the LMTO formalism. By dividing space into regions where the potential is spherically symmetric, and regions where the potential is constant, the solutions to the one-particle Schrödinger equation are known analytically and perhaps more importantly, constitute a complete basis set. In practice, we have to truncate the l expansion for the orbitals, but luckily, even $l=2$ is a very good approximation. This is largely based on physical reasoning; depending on the atom species being studied, different atomic orbitals contribute to the electronic behaviour at the Fermi level. For example, for transition metals (of which platinum is one) the d-orbitals are very important, which are precisely the $l=2$ orbitals. Choosing the $l=3$ basis for Pt has some effect on the spin Hall angle, but not on the spin flip diffusion length, as shown in [13].

The MT spheres of the muffin-tin are expanded in size until they fill the volume of the crystal. Additionally, we set the kinetic energy of the solution to the wave equation in the interstitial region (which now has zero volume) to zero. This method is called the atomic spheres approximation (ASA), and throughout this report, this is the potential we use for any large calculations. The ASA is not sufficiently accurate for all systems, particularly for systems with low symmetry, or open systems. Close packed crystals such as the face-centered cubic (fcc) lattice are approximated quite well by the ASA, so for the case of Pt there are no problems. One particular method of more accurately representing the atomic potential by a sum of spherically symmetric potentials is called the Overlapping Muffin Tin Approximation (OMTA) and is the subject of a later section of this report. The OMTA unfortunately does not work for the conventional LMTOs.

3.2 LMTOs within the ASA

In the atomic sphere approximation (ASA), there exist only regions of space where the potential is zero ($V=0$) and regions where the potential is spherically symmetric ($V=V(r)$). Let us for the moment consider a single atom. One can numerically solve the radial Schrödinger equation inside the atomic sphere at energy ε to find the so-called partial wave

$$\phi_{Rlm}(\varepsilon,\mathbf{r}_R)=\phi_{Rl}(\varepsilon,r_R)Y_{lm}(\hat{\mathbf{r}}_R)\,, \tag{3.2.1}$$

where R is the atomic position, l is the angular quantum number, m is the magnetic quantum number, $\hat{\mathbf{r}}_R$ is a unit vector, $\mathbf{r}_R:=\mathbf{r}-\mathbf{R}$ and $r_R:=|\mathbf{r}-\mathbf{R}|$. The function $Y_{lm}(\hat{\mathbf{r}}_R)$ is the spherical harmonic. A continuous and differentiable orbital is constructed by attaching at the boundary of the atomic sphere a “tail”, a linear combination of solutions to the Laplace equation.

$$J^0_{RL}(\mathbf{r}_R) := (r_R/\omega)^l \, [2(2l+1)]^{-1} \, Y_L(\hat{\mathbf{r}}_R) \,, \tag{3.2.2}$$

$$K^0_{RL}(\mathbf{r}_R) := (r_R/\omega)^{-l-1} \, Y_L(\hat{\mathbf{r}}_R) \,. \tag{3.2.3}$$

Here we have used the abbrevation $L := lm$. ω is a length scale, usually the radius of the atomic sphere. The radial functions are matched in terms of the logarithmic derivative (where ϕ' is the radial derivative) at s, which is the radius of the atomic sphere (from here on we drop the atomic position R if it does not give rise to ambiguity).

$$D_l(\varepsilon, s) := \frac{s\phi'_l(\varepsilon, s)}{\phi_l(\varepsilon, s)} \,. \tag{3.2.4}$$

Defining the so-called “potential function”

$$P^0_l(\varepsilon) = 2(2l+1)\left(\frac{\omega}{s}\right)^{2l+1} \frac{D_l(\varepsilon) + l + 1}{D_l(\varepsilon) - l} \tag{3.2.5}$$

and normalization

$$N^0_l(\varepsilon) = \frac{2l+1}{l - D_l}\left(\frac{\omega}{s}\right)^{l+1} \frac{1}{\phi_l(\varepsilon, s)} \,, \tag{3.2.6}$$

the matching condition on the radial interstitial wave function (i.e. for $r \geq s$) becomes

$$N^0_l(\varepsilon)\phi_l(\varepsilon, r) = K^0_l(r) - P^0_l(\varepsilon) J^0_l(r) \,. \tag{3.2.7}$$

However, we see see that this expression diverges for $r \to \infty$, so to construct a function which is everywhere continuous, differentiable and regular, we simply subtract the term with $J^0_l(r)$ from the partial wave in the interstitial region as well as the atomic sphere. This is the MTO.

$$\chi^0_L(\varepsilon, \mathbf{r}_R) = \begin{cases} N^0_l(\varepsilon)\phi_l(\varepsilon, \mathbf{r}) + P^0_l(\varepsilon) J^0_l(\mathbf{r}) & r \leq s \,, \\ K^0_L(\mathbf{r}) & r \geq s \,. \end{cases} \tag{3.2.8}$$

The tail $K^0_{RL}(\mathbf{r}_R)$ can be expanded in a closed form around any other site R' in terms of $J^0_{R'L'}(\mathbf{r}_{R'})$

$$K^0_{RL} = -\sum_{L'} J^0_{R'L'}(\mathbf{r}_{R'}) S^0_{R'L',RL} \,. \tag{3.2.9}$$

The coefficients $S^0_{R'L',RL}$ are known as the canonical structure constants. They are canonical in the sense that they only depend on the crystal structure, not on lattice parameters, atomic sphere potentials or energy. The augmentation of the partial wave with $J^0_L(\mathbf{r})$ means that the MTO is no longer a solution of the Schrödinger equation within its own sphere. However, when we use the expansion (3.2.9), we find that the linear combination of MTOs on different sites does solve the Schrödinger equation. This wave function,

$$\Psi(\varepsilon, \mathbf{r}) = \sum_{R,L} \chi^0_{RL}(\varepsilon, \mathbf{r}_R) C^0_{RL} \tag{3.2.10}$$

recovers the partial wave solution implemented in the very beginning, but only when the tails of all other MTOs cancel the $J^0_{RL}(\mathbf{r}_R)$ augmentation of the MTO at R. This requirement is called the "tail-cancellation" condition:

$$\sum_{R',L'} \left[P^0_{RL}(\varepsilon)\delta_{RR'}\delta_{LL'} - S^0_{RL,R'L'}\right] C^0_{R'L'} = 0\,. \tag{3.2.11}$$

If the crystal is assumed to be infinitely large through periodic boundary conditions, the wave function becomes periodic and we can transform the equation from real space to (momentum) k-space. Solving this equation gives the band structure of the material at hand. When performing a band structure calculation, the energy dependence must be taken care of. Normally this is done by linearising the tail-cancellation condition around particular energies ε_ν. For the transport problem, we are only interested in the behaviour at the Fermi energy, so we can just use the equation as-is.

The MTOs derived above form a minimal basis, in general one only needs *spd* or *spdf* orbitals to find a satisfactory band structure, but one problem remains. The MTOs have infinite range, such that a transport calculation would be very expensive indeed, as the Hamiltonian would be rather dense. Luckily, a relatively simple method of "screening" the structure constants exists, which transforms our MTOs into tight-binding MTOs, which have very short range. We introduce screening constants α_{Rl}, which alter the potential function and the structure constants as follows.

$$P^\alpha(\varepsilon) = P^0(\varepsilon) + P^0(\varepsilon)\alpha P^\alpha(\varepsilon) = P^0(\varepsilon)\left[1 - \alpha P^0(\varepsilon)\right]^{-1} \tag{3.2.12}$$

and

$$S^\alpha = S^0 + S^0\alpha S^\alpha = S^0(1 - \alpha S^0)^{-1}\,. \tag{3.2.13}$$

The screened tail cancellation becomes

$$\sum_{R',L'} \left[P^\alpha_{RL}(\varepsilon)\delta_{RR'}\delta_{LL'} - S^\alpha_{RL,R'L'}\right] C^0_{R'L'} = 0\,. \tag{3.2.14}$$

Let us first rewrite this equation in vector form

$$\left[\mathbf{P}^\alpha(\varepsilon) - \mathbf{S}^\alpha\right] \cdot \mathbf{C} = 0\,. \tag{3.2.15}$$

If we expand this equation as a Taylor series in ε about ε_ν, we obtain

$$\left[\mathbf{P}^\alpha(\varepsilon_\nu) - \mathbf{S}^\alpha + \dot{\mathbf{P}}^\alpha(\varepsilon_\nu)\left(\varepsilon - \varepsilon_\nu\right) + O\left(\varepsilon - \varepsilon_\nu\right)^2\right] \cdot \mathbf{C} = 0\,,$$

where $\dot{P}$ implies the energy derivative of P, which we can rewrite to an eigenvalue equation

$$-[\dot{\mathbf{P}}^\alpha(\varepsilon_\nu)]^{-1/2}[\mathbf{P}^\alpha(\varepsilon_\nu) - \mathbf{S}^\alpha][\dot{\mathbf{P}}^\alpha(\varepsilon_\nu)]^{-1/2} \cdot \mathbf{C} = \left(\varepsilon - \varepsilon_\nu\right)\mathbf{C} + O\left(\varepsilon - \varepsilon_\nu\right)^2\,.$$

This is an eigenvalue equation which yields the energy, which in the context of Quantum Mechanics means that our operator is a Hamiltonian, up to first order in the energy. In the context of a transport calculation, the energy dependence is of little concern, as we set the energy $\varepsilon = \varepsilon_\nu = \varepsilon_F$ and calculate all of the properties there. The first-order Hamiltonian is

$$\mathbf{h}^\alpha = -[\dot{\mathbf{P}}^\alpha]^{-1/2}[\mathbf{P}^\alpha - \mathbf{S}^\alpha][\dot{\mathbf{P}}^\alpha]^{-1/2}\,, \tag{3.2.16}$$

and the TB-MTOs are

$$|\chi^\alpha_{RL}\rangle = |\phi_{RL}\rangle + \sum_{R'L'} \left|\dot{\phi}_{R'L'}\right\rangle h^\alpha_{R'L",RL}\,, \tag{3.2.17}$$

where $\dot{\phi}$ is the energy derivative evaluated at $\varepsilon = \varepsilon_\nu$.

3.2.1 On the approximations made

The two major approximations in the above are the independent particle approximation and the muffin-tin approximation. The first is necessary to write down a one-particle basis for the wave function at all. The many-body problem is not analytically solvable, and the few methods that exist to approximate the solutions to the many-body problem all use the one-particle wave function as their basis. The many-body effects are included approximately within the DFT framework [5, 4] through the exchange-correlation (x-c) functional, for which we choose the Local Density Approximation (LDA). Many more types of x-c functionals exist, in varying degrees of complexity and computational cost, but we will not discuss them in detail. The LDA can be physically reasoned to be adequate for our purposes, since logically the transport of an electron from one atom to the next is dominated by the local electron density around these atoms, and in practice, the LDA gives reasonable results. When we wish to actually perform transport calculations, there are some more approximations to consider. There is of course the truncation of the expansion in l, but the code lends itself very easily to check for numerical convergence by allowing different values of l. Two more points of attention are the supercell size and the k-point sampling of the Brillouin zone. Detailed numerical convergence tests of these parameters can be found in [13].

3.3 Spin-orbit coupling

One essential part of our calculations is the spin-orbit coupling (SOC), which couples the orbital and the spin degrees of freedom, introducing rich physics in the process, not the least of which is the spin Hall effect (SHE). The angular momentum operator is $\hat{L} = \hat{r} \times \hat{p}$, where r is the position operator and p is the momentum operator. The spin operator $\hat{S}$ is the spin analogue. SOC is a relativistic effect, arising directly when expanding the relativistic quantum mechanical Dirac equation in a power series in $(mc)^{-2}$ to first order.

$$\left[\frac{\hat{p}^2}{2m} + V - \frac{\hat{p}^4}{8m^3c^2} + \frac{\hbar}{4im^2c^2}\left(\nabla V \cdot \hat{p}\right) + \frac{\hbar}{4m^2c^2}\left(\nabla V \times \hat{p}\right) \cdot \hat{S}\right]\psi = E\psi \tag{3.3.1}$$

The relevant term is the last term on the left hand side. The potential V is approximately spherically symmetric in the case of ASA-MTOs, so we can rewrite to

$$\begin{aligned}\hat{H}_{so} &= \frac{\hbar}{4m^2c^2}\left(\frac{1}{r}\frac{dV}{dr}\hat{r} \times \hat{p}\right) \cdot \hat{S} \\ &= \frac{\hbar}{4m^2c^2}\frac{1}{r}\frac{dV(r)}{dr}\hat{L} \cdot \hat{S}\,.\end{aligned}$$

This closely resembles the familiar SOC term $\hat{H}_{so} = \xi \hat{L} \cdot \hat{S}$ one learns in quantum mechanics courses. The MTO potential allows us to treat the coupling parameter fully.

We treat SOC as a perturbation on the earlier derived Hamiltonian matrix so that in the MTO basis, the matrix elements of $\hat{H}_{so}$ become

$$\langle \chi^\alpha | \hat{H}_{so} | \chi^\alpha \rangle = \gamma_1 + \gamma_2 \mathbf{h}^\alpha + \mathbf{h}^\alpha \gamma_2^+ + \mathbf{h}^\alpha \gamma_3 \mathbf{h}^\alpha\,. \tag{3.3.2}$$

The γ-terms are SOC parameters for one-, two-, and three-center terms (omitting the $\frac{\hbar}{4m^2}$ factor)

$$\gamma_1 = \langle\phi|\,\frac{1}{c^2 r}\frac{dV}{dr}\hat{L}\cdot\hat{S}\,|\phi\rangle = \mathbf{K}\otimes\xi\,, \tag{3.3.3}$$

$$\gamma_2 = \langle\phi|\,\frac{1}{c^2 r}\frac{dV}{dr}\hat{L}\cdot\hat{S}|\dot{\phi}^{\alpha}\rangle = \mathbf{K}\otimes\dot{\xi}^{\alpha}\,, \tag{3.3.4}$$

$$\gamma_3 = \langle\dot{\phi}^{\alpha}|\frac{1}{c^2 r}\frac{dV}{dr}\hat{L}\cdot\hat{S}|\dot{\phi}^{\alpha}\rangle = \mathbf{K}\otimes\ddot{\xi}^{\alpha}\,, \tag{3.3.5}$$

where we have introduced a matrix

$$\mathbf{K} = \langle lm\sigma|\,\hat{L}\cdot\hat{S}\,|l'm'\sigma'\rangle\ , \tag{3.3.6}$$

and so-called SOC potential parameters

$$\xi_{l\sigma\sigma'} = \langle\phi_{l\sigma}(r)|\,\frac{1}{c^2 r}\frac{dV^{\sigma\sigma'}(r)}{dr}\,|\phi_{l\sigma'}(r)\rangle\ , \tag{3.3.7}$$

$$\dot{\xi}^{\alpha}_{l\sigma\sigma'} = \langle\phi_{l\sigma}(r)|\,\frac{1}{c^2 r}\frac{dV^{\sigma\sigma'}(r)}{dr}|\dot{\phi}^{\alpha}_{l\sigma'}(r)\rangle\,, \tag{3.3.8}$$

$$\ddot{\xi}^{\alpha}_{l\sigma\sigma'} = \langle\dot{\phi}^{\alpha}_{l\sigma}(r)|\frac{1}{c^2 r}\frac{dV^{\sigma\sigma'}(r)}{dr}|\dot{\phi}^{\alpha}_{l\sigma'}(r)\rangle\,. \tag{3.3.9}$$

In practice the last two are calculated slightly differently, through

$$\dot{\xi}^{\alpha}_{l\sigma\sigma'} = \dot{\xi}_{l\sigma\sigma'} + \xi_{l\sigma\sigma'}o^{\alpha}_{l\sigma'}\,, \tag{3.3.10}$$

$$\ddot{\xi}^{\alpha}_{l\sigma\sigma'} = \ddot{\xi}_{l\sigma\sigma'} + \dot{\xi}_{l\sigma\sigma'}\,(o^{\alpha}_{l\sigma} + o^{\alpha}_{l\sigma'}) + \xi_{l\sigma\sigma'}o^{\alpha}_{l\sigma}o^{\alpha}_{l\sigma'}\,, \tag{3.3.11}$$

where $\mathbf{o}^{\alpha} = \langle\phi|\dot{\phi}\rangle$. These parameters can be found by radially integrating over the atomic sphere (this is what the bra-ket notation implies). We see that the screened SOC parameters can be rewritten in terms of the non-screened parameters with additional overlap terms. It is assumed that $V^{\uparrow\downarrow} \approx \frac{1}{2}\left(V^{\uparrow\uparrow} + V^{\downarrow\downarrow}\right)$ since the self-consistent DFT calculation only gives potentials for each spin separately.

The complete Pauli-Schrödinger equation in our formalism is

$$\mathbf{H} = [E_{\nu}\mathbf{I} + \gamma_1] + [\mathbf{h}^{\alpha} + \gamma_2\mathbf{h}^{\alpha} + \mathbf{h}^{\alpha}\gamma_2] + [\mathbf{h}^{\alpha}(\mathbf{o}^{\alpha} + \gamma_3)\mathbf{h}^{\alpha}] \tag{3.3.12}$$

where the brackets indicated one-, two- and three-center terms respectively. In practice, the three-center terms do not influence the resistivity calculation by much, although the spin Hall angle seems to be affected more severely. Nevertheless, the computational cost is reduced by 70% when this term is neglected, which is why we usually do not take it into account. For an idea of the effect of this term on the SHA and resistivity, see [13].

3.4 Exact Muffin-Tin Orbitals

The LMTOs described above form a very efficient minimal basis set, which is highly suitable for transport calculations. Their only drawback is their limitation to close-packed crystal structures whose electronic structures are accurately represented by the ASA. One way out of this issue is to use a more sophisticated basis set, namely the "third generation LMTOs" [1, 10]. The TB-LMTOs defined above are the second generation. The third generation LMTOs can easily be generalised to be an Nth order approximation in the energy dependence, rather than just linear (which would be an NMTO with $N = 1$), like the LMTOs. In our case, however, we can ignore this approximation in the energy, as our whole calculation happens at the Fermi energy. In the literature, Andersen himself uses the term Exact Muffin-Tin Orbital (EMTO) to describe this kind of basis. The outline below is largely borrowed from [10].

3.4.1 Partial waves

The EMTO is constructed slightly differently from the LMTO, but follows the same philosophy. We will again divide the crystal into atomic spheres and an interstitial region. Inside the atomic sphere, the potential is spherically symmetric, and the wave function will be a solution to the Schrödinger equation. For heavy atoms, it is relevant to take into account relativistic effects, so we will use the Dirac equation. Omitting the derivation, the solution to the Dirac equation is

$$\phi(\mathbf{r},\mathbf{s}) = \begin{pmatrix} g(r)\chi(\hat{\mathbf{r}},\mathbf{s}) \\ f(r)\widetilde{\chi(\hat{\mathbf{r}},\mathbf{s})} \end{pmatrix} . \tag{3.4.1}$$

where $\mathbf{s}$ are the spin components. The radial functions $f(r)$ and $g(r)$ are solutions to the coupled differential equations

$$\begin{aligned} cf'(r) &= c\left(\frac{\mathcal{K}-1}{r}\right) f(r) - (E-V)\,g(r) \\ cg'(r) &= -c\left(\frac{\mathcal{K}-1}{r}\right) g(r) + \left(E - V + 2mc^2\right) f(r)\,, \end{aligned}$$

where c is some constant and $\mathcal{K}$ is a spin-orbit coupling term $\mathcal{K} = -\left(\hat{S}\cdot\hat{L} - 1\right)$. We can eliminate $f(r)$ from the two equations, yielding

$$-\frac{1}{2M}\left[g''(r) + \frac{2}{r}g'(r) - \frac{l(l+1)}{r^2}g(r)\right] - \frac{V'(r)g'(r)}{4M^2c^2} + V(r)g(r) - \left[\frac{\mathcal{K}+1}{r}\frac{V'(r)g(r)}{4M^2c^2}\right] = Eg(r)\,, \tag{3.4.2}$$

where $M = m + \frac{E-V}{2c^2}$. The operator containing spin is only present in the very last term on the left hand side. We use the scalar relativistic approximation, which equates to ignoring this term. We will add it back later perturbatively. The solution to the Dirac equation becomes

$$\phi(\mathbf{r},\mathbf{s}) = \begin{pmatrix} g_l(r)Y_{lm}(\theta,\phi)\chi(\mathbf{s}) \\ \frac{1}{2Mc}g_l'(r)Y_{lm}(\theta,\phi)\widetilde{\chi(\mathbf{s})} \end{pmatrix} . \tag{3.4.3}$$

Within the scalar relativistic approximation, the angular momentum l is a good quantum number. We can numerically integrate the radial differential equation to find $g_l(r)$ and $g_l'(r)$, just as in the LMTO case. The resulting function, which is a product of a radial function and a spherical harmonic, is called a *partial wave*.

3.4.2 Screened spherical waves

Now we move on to the interstitial region. In the LMTO case, we assume that $V = 0$ in the interstitial region. Here we allow $V =$ constant so that the Schrödinger equation becomes the Helmholtz equation

$$\nabla^2 \psi = -\left(E - V_{mtz}\right)\psi = -\kappa^2 \psi\,. \tag{3.4.4}$$

There exist many solutions to this equation, the most notable being the plane wave solution $\psi = Ae^{i\mathbf{k}\cdot\mathbf{r}}$, which is the basis of many popular DFT applications. As the title of this section suggests, we will instead use spherical solutions to the wave equation, known to the mathematicians as spherical Bessel functions of the first and second kind, and to physicists as spherical Bessel and Neumann functions. We will go about this in a very specific way, in order to finally obtain a wave function which has desirable properties. These properties include differentiability, continuity, but also short spatial range.

We begin by defining so-called "screening spheres", each sphere having a particular radius a_R and being centered on an atom at $\mathbf{R}$. For each atom, we define a "screened spherical wave" $\psi_{\mathbf{R}L}$ (SSW), which has the boundary conditions

$$\begin{cases} \psi_{\mathbf{R}L}\left(|\mathbf{r} - \mathbf{R}'| = a_{\mathbf{R}'}\right) = Y_L & \text{if } \mathbf{R}' = \mathbf{R}\,, \\ \psi_{\mathbf{R}L}\left(|\mathbf{r} - \mathbf{R}'| = a_{\mathbf{R}'}\right) = 0 & \text{if } \mathbf{R}' \neq \mathbf{R}\,. \end{cases} \tag{3.4.5}$$

i.e. the SSW must be zero at all screening spheres centered at the other atoms, and must equal the spherical harmonic at its own screening sphere. By defining the SSW this way, we ensure that it will be short-ranged, since it must go to zero at the boundary of the screening sphere of every atom (aside from its own), including the nearest neighbours. By making the SSW equal a spherical harmonic on its own sphere, we can easily match it onto the partial wave, which we recall to be a sum of products of a radial function and a spherical harmonic. It is clear the screening spheres are not allowed to overlap, because the value of the SSW cannot be simultaneously equal to zero and the spherical harmonic.

We construct the SSW to be a superposition of spherical waves originating from each sphere.

$$\psi_{\mathbf{R}L}(\mathbf{r}) = \sum_{\mathbf{R}'L'} n_{\mathbf{R}'l'} Y_{L'} M_{\mathbf{R}'L',\mathbf{R}L}\,, \tag{3.4.6}$$

where $n_{\mathbf{R}'l'}$ is the spherical Neumann function centered at $\mathbf{R}'$ with angular momentum character l'. The matrix $M_{\mathbf{R}',L',\mathbf{R}L}$ contains all screening information. The spherical wave $n_{\mathbf{R}l}$ can be expanded into a sum of spherical waves originating at all other sites in the so-called one-center expansion.

$$n_{\mathbf{R}l} Y_{\mathbf{R}L} = n_{\mathbf{R}l} Y_{\mathbf{R}L} \delta_{\mathbf{R},\mathbf{R}'} - \sum_{L'} j_{\mathbf{R}'l'} Y_{\mathbf{R}'L'} S^0_{\mathbf{R}'L',\mathbf{R}L}\,, \tag{3.4.7}$$

where S^0 are the canonical structure constants, which are also present in the LMTO method. Instead of using this expansion, however, we will use a more general expansion, where we allow the spherical waves originating at $\mathbf{R}$ and $\mathbf{R}'$ to be superpositions of spherical Bessel and Neumann functions, rather than only the Neumann function for $\mathbf{R}$ and the Bessel function for $\mathbf{R}'$.

$$\psi_{\mathbf{R}L} = n^\alpha_{\mathbf{R}l} Y_{\mathbf{R}L} \delta_{\mathbf{R}',\mathbf{R}} - \sum_{L'} j^\alpha_{\mathbf{R}l'} Y_{\mathbf{R}'L'} S^\alpha_{\mathbf{R}'L',\mathbf{R}L}\,, \tag{3.4.8}$$

where

$$\begin{cases} n^{\alpha}_{\mathbf{R}l} &= t^{(1)}_{\mathbf{R}l} n_{\mathbf{R}l} + t^{(2)}_{\mathbf{R}l} j_{\mathbf{R}l}\,, \\ j^{\alpha}_{\mathbf{R}l} &= t^{(3)}_{\mathbf{R}l} n_{\mathbf{R}l} + t^{(4)}_{\mathbf{R}l} j_{\mathbf{R}l}\,. \end{cases} \tag{3.4.9}$$

The boundary conditions on the screening spheres give boundary conditions for these functions, i.e. $n^{\alpha}_{\mathbf{R}l}(a_{\mathbf{R}}) = 1$ and $j^{\alpha}_{\mathbf{R}l}(a_{\mathbf{R}}) = 0$. To fully specify $t^{(i)}$ for $i = 1, 2, 3, 4$, we need to specify their radial slope at the $a_{\mathbf{R}}$ spheres, so we choose ${n^{\alpha}_{\mathbf{R}l}}'(a_{\mathbf{R}}) = 0$ and ${j^{\alpha}_{\mathbf{R}l}}'(a_{\mathbf{R}}) = -1/a_{\mathbf{R}}$. The t values are then defined as

$$\begin{pmatrix} t^{(1)} & t^{(2)} \\ t^{(3)} & t^{(4)} \end{pmatrix} = \frac{2a^2_{\mathbf{R}}}{\omega} \begin{pmatrix} j'_{\mathbf{R}l}(a_{\mathbf{R}}) & -n'_{\mathbf{R}'l}(a_{\mathbf{R}}) \\ j_{\mathbf{R}l}(a_{\mathbf{R}})/a_{\mathbf{R}} & -n_{\mathbf{R}l}(a_{\mathbf{R}})/a_{\mathbf{R}} \end{pmatrix}\,. \tag{3.4.10}$$

We find the elements of M and S^{α} by comparing the two decriptions of the SSW. On the one hand, using (3.4.6) and (3.4.7) we expand the SSW $\psi_{\mathbf{R}L}$ about some other site $\mathbf{R}''$.

$$\psi_{\mathbf{R}L} = \sum_{L''} Y_{L''} \left[\sum_{\mathbf{R}'L'} \left[n_{\mathbf{R}''l''} \delta_{\mathbf{R}'',\mathbf{R}'} \delta_{L'',L'} - j_{\mathbf{R}''l''} S^{0}_{\mathbf{R}''L'',\mathbf{R}'L'} \right] M_{\mathbf{R}'L',\mathbf{R}L} \right] \tag{3.4.11}$$

On the other hand, by expanding (3.4.8) by (3.4.9), we have

$$\begin{aligned} \psi_{\mathbf{R}L} = \sum_{L''} Y_{L''} \Big[& n_{\mathbf{R}''l''} \left(t^{(1)}_{\mathbf{R}''l''} \delta_{\mathbf{R}'',\mathbf{R}} \delta_{L'',L'} - t^{(3)}_{\mathbf{R}''l''} S^{\alpha}_{\mathbf{R}''L'',\mathbf{R}'L'} \right) \\ & + j_{\mathbf{R}''l''} \left(t^{(2)}_{\mathbf{R}''l''} \delta_{\mathbf{R}'',\mathbf{R}'} \delta_{L'',L'} - t^{(4)}_{\mathbf{R}''l''} S^{\alpha}_{\mathbf{R}''L'',\mathbf{R}L} \right) \Big]\,. \end{aligned} \tag{3.4.12}$$

Directly comparing the two expressions, we can straightforwardly extract expressions for $M_{\mathbf{R}'L',\mathbf{R}L}$.

$$\begin{aligned} M_{\mathbf{R}'L',\mathbf{R}L} &= \left(t^{(1)}_{\mathbf{R}l} \delta_{\mathbf{R}',\mathbf{R}} \delta_{L',L} - t^{(3)}_{\mathbf{R}'\mathbf{l}'} S^{\alpha}_{\mathbf{R}'L'',\mathbf{R}L} \right)\,, \\ \sum_{\mathbf{R}'L'} S^{0}_{\mathbf{R}''L'',\mathbf{R}'L'} M_{\mathbf{R}'L',\mathbf{R}L} &= -\left(t^{(2)}_{\mathbf{R}l} \delta_{\mathbf{R}'',\mathbf{R}} \delta_{L'',L} - t^{(4)}_{\mathbf{R}''l''} S^{\alpha}_{\mathbf{R}''L'',\mathbf{R}L} \right)\,. \end{aligned}$$

We can eliminate M from these expressions to find a closed form for S^{α},

$$S^{\alpha}_{\mathbf{R}'L',\mathbf{R}L} = \frac{t^{(1)}_{\mathbf{R}l}}{t^{(3)}_{\mathbf{R}}l} \delta_{\mathbf{R}',\mathbf{R}} \delta_{L',L} + \frac{1}{t^{(3)}_{\mathbf{R}'l'}} \left[-\frac{t^{(4)}}{t^{(3)}} - S^{0} \right]^{-1}_{\mathbf{R}'L',\mathbf{R}L} \frac{1}{t^{(3)}_{\mathbf{R}l}} \left(t^{(1)}_{\mathbf{R}l} t^{(4)}_{\mathbf{R}l} - t^{(2)}_{\mathbf{R}l} t^{(3)}_{\mathbf{R}l} \right)\,. \tag{3.4.13}$$

The S^{α} together with n^{α} and j^{α} fully specify each SSW.

3.4.3 *Back-extrapolated partial wave*

It turns out that the partial wave and the screened spherical wave (SSW) alone are not enough to construct the wave function. This is because the spheres are of different radius (s for the partial wave, and $a < s$ for the SSW). Setting $a = s$ is not satisfactory, because then we cannot fill the space with spheres, since then the a spheres overlap, which is not allowed. Using small spheres with $a = s$ is also not desirable, since then the muffin-tin approximation is very poor. The solution is to introduce an additional function, the so-called back-extrapolated partial wave, which solves the Schrödinger equation in the range $a < r < s$ for the flat interstitial potential.

$$\left(-\nabla^2 + (V_{mtz} - E) \right) \varphi_l(r) Y_L = 0\,. \tag{3.4.14}$$

The back-extrapolated partial wave has the boundary condition that it matches the partial wave at $r = s$ in slope as well as value. The partial wave and back-extrapolated partial wave are normalised such that $\varphi(a_{\mathbf{R}}) = 1$, so that the back-extrapolated partial wave automatically continuously matches the SSW at the screening sphere.

3.4.4 Kinked partial wave

We have constructed a wave function which is continuous, but has kinks (points where the derivative is discontinuous) at each $a_{\mathbf{R}}$ sphere. The kinked partial wave (KPW) is

$$\Phi_{\mathbf{R}L} = (\phi_l - \varphi_l)\, Y_L + \psi_{\mathbf{R}L}\,, \tag{3.4.15}$$

where ϕ is the partial wave, φ is the back-extrapolated partial wave and ψ is the screened spherical wave (SSW). The wave function is constructed as a linear combination of KPWs, where analogous to the tail-cancellation condition for LMTOs, a new set of equations arises, called the kink-cancellation conditions. This set of equations is the result of forcing the constructed MTOs to be continuous and differentiable, which results in a linear equation where the KPWs cancel each others kinks. As in the LMTO case, this set of equations becomes the backbone of the computational scheme. When we set the energy, the Hamiltonian identically equals the kink matrix, which is defined as

$$K_{\mathbf{R}L,\mathbf{R}'L'} = a_{\mathbf{R}}\left(D^{\alpha}\delta_{\mathbf{R},\mathbf{R}'} - S^{\alpha}_{\mathbf{R}L,\mathbf{R}'L'}\right)\,, \tag{3.4.16}$$

where $D^{\alpha} = a_{\mathbf{R}} \left.\frac{\partial \varphi_{\mathbf{R}l}}{\partial r}\right|_{a_{\mathbf{R}}}$ is the logarithmic derivative of the back-extrapolated partial wave at $a_{\mathbf{R}}$.

3.4.5 Kink cancellation condition and the Hamiltonian

The kinked partial waves as a basis present some interesting qualities. The converning equation, which in the TB-MTOs was the tail-cancellation condition $[\mathbf{P} - \mathbf{S}] \cdot \mathbf{v} = 0$, now becomes the kink-cancellation condition

$$\mathbf{K}(E) \cdot \mathbf{v} = 0\,, \tag{3.4.17}$$

where $\mathbf{v}$ are the coefficients of the total wave function on the KPW basis, i.e.

$$\Psi(E) = \sum_{\mathbf{R}L} \Phi_{\mathbf{R}L}(E) v_{\mathbf{R}L}\,. \tag{3.4.18}$$

We can move from the kink-cancellation condition (which is equivalent to a set of KKR equations) to the more useful Hamiltonian formalism through the same trick we employed in the 2nd generation LMTO method. The kink matrix is energy-dependent, which is inconvenient, so we Taylor expand it to obtain a Hamiltonian,

$$\begin{aligned}
\mathbf{K}(E) \cdot \mathbf{v} &= 0\,,\\
\left[\mathbf{K}(E_\nu) + (E - E_\nu)\,\dot{\mathbf{K}}(E_\nu) + O(E - E_\nu)^2\right] \cdot \mathbf{v} &= 0\,,\\
\mathbf{K}(E_\nu) \cdot \mathbf{v} &\approx -\,(E - E_\nu)\,\dot{\mathbf{K}}(E_\nu) \cdot \mathbf{v}\,,\\
\left[\mathbf{K}(E_\nu) - E_\nu \dot{\mathbf{K}}(E_\nu)\right] \cdot \mathbf{v} &\approx -E\dot{\mathbf{K}}(E_\nu) \cdot \mathbf{v}\,,
\end{aligned}$$

which allows us to directly write down a Hamiltonian form,

$$\hat{H}^{\mathrm{e}} = \mathbf{K}(E_\nu) - E_\nu \dot{\mathbf{K}}(E_\nu)\,, \tag{3.4.19}$$

$$\hat{O}^{\mathrm{e}} = -\dot{\mathbf{K}}\,. \tag{3.4.20}$$

More concisely, if we impose $E = E_\nu$ (as we do in a transport calculation), the matrix elements of $\hat{H}^{\mathrm{e}} - E\hat{O}^{\mathrm{e}}$ simply become

$$\langle \Phi |\, \hat{H}^{\mathrm{e}} - E\hat{O}^{\mathrm{e}}\, | \Phi \rangle = \mathbf{K}(E_\nu)\,. \tag{3.4.21}$$

Not only does the kink matrix $\mathbf{K}$ represent the kinks in the wave function that need to be cancelled, on the basis of KPWs, the matrix elements of the Hamiltonian are identical to $\mathbf{K}$. This means that solving the kink-cancellation condition (the KKR equations) is equivalent to diagonalizing the Hamiltonian.

Because the energy-dependent KPW basis can be used to solve the muffin-tin problem exactly at some particular energy E_ν, this basis is also called the Exact Muffin Tin Orbital (EMTO) method.

The above has one more important implication. It means that we are not obliged to linearize the MTO in the energy, as we did in the 2nd generation. If we set the energy $E = E_\nu$, we have a large enough energy window in which the KPW evaluated at $E = E_\nu$ provides an adequate basis, without having to include its energy derivative. This has been reinforced by (as of writing, unpublished) calculations where a linearized MTO basis was used. The energy-independent, linearized MTO based on the KPWs is

$$|\chi\rangle = |\Phi(E_\nu)\rangle - \left|\dot{\Phi}(E_\nu)\right\rangle \dot{\mathbf{K}}^{-1}(E_\nu)\mathbf{K}(E_\nu) \tag{3.4.22}$$

where $-\dot{\mathbf{K}}^{-1}(E_\nu)\mathbf{K}(E_\nu)$ is the first-order Hamiltonian, equivalent to $\mathbf{h}^\alpha$ in the 2nd generation LMTO. In the following, we will need the overlaps between Φ and $\dot{\Phi}$, which are

$$\begin{aligned} \langle \Phi | \Phi \rangle &= -\dot{\mathbf{K}}\,, \\ \left\langle \Phi \middle| \dot{\Phi} \right\rangle &= -\frac{1}{2}\ddot{\mathbf{K}}\,, \\ \left\langle \dot{\Phi} \middle| \dot{\Phi} \right\rangle &= -\frac{1}{6}\dddot{\mathbf{K}}\,. \end{aligned} \tag{3.4.23}$$

The KPWs satisfy

$$\left[\hat{H}_{\mathrm{mt}} - E_\nu\right] |\Phi\rangle = 0\,,$$

where $\hat{H}_{\mathrm{mt}}$ is the muffin-tin Hamiltonian $\hat{H}_{\mathrm{mt}} = -\frac{\hbar}{2m}\nabla^2 + \sum_{\mathbf{R}} v_{\mathbf{R}}(\mathbf{r} - \mathbf{R})$. If we take the energy derivative of this equation, we find the action of the muffin-tin Hamiltonian on the $\dot{\Phi}$ states,

$$\begin{aligned} \frac{d}{dE}\left[\hat{H}_{\mathrm{mt}} - E_\nu\right] |\Phi\rangle &= 0\,, \\ \left[\hat{H}_{\mathrm{mt}} - E_\nu\right] \left|\dot{\Phi}\right\rangle - |\Phi\rangle &= 0\,, \\ \left[\hat{H}_{\mathrm{mt}} - E_\nu\right] \left|\dot{\Phi}\right\rangle &= |\Phi\rangle\ . \end{aligned}$$

The above is sufficient to find the matrix elements of $\hat{H}_{\mathrm{mt}} - E_\nu$ on the basis of the LMTOs. Omitting the algebra, we have

$$\langle\chi|\, \hat{H}_{\mathrm{mt}} - E_\nu \,|\chi\rangle = \mathbf{K} - \frac{1}{2}\mathbf{K}\dot{\mathbf{K}}^{-1}\ddot{\mathbf{K}}\dot{\mathbf{K}}^{-1}\mathbf{K}\,. \tag{3.4.24}$$

Omitting the second term into the matrix elements is equivalent to disregarding the energy dependence of the basis functions. That is, if for the energy window of interest, the KPWs are sufficiently energy-independent, the energy derivatives of the kink matrix vanish, and we are left with just the kink matrix elements.

Testing of the 2nd generation LMTO code also allowed us to omit the $\mathbf{h}^\alpha\mathbf{o}^\alpha\mathbf{h}^\alpha$ term in the matrix elements on the LMTO basis, but the implication here is much bigger. Here, the omission of the second term implies that we do not have to consider the energy derivative of the KPWs at all, where in the 2nd generation method, we still had to include them in the SOC matrix elements.

3.4.6 Angular momentum & spin matrix elements

In the Derivations section, we will present final expressions which include spin-orbit coupling matrix elements. Here we briefly discuss their properties. The expressions are of the form

$$\langle lm\sigma|\, \hat{L}\cdot\hat{S} \,|l'm'\sigma'\rangle \ , \tag{3.4.25}$$

which, being eigenstates of the $\hat{L}_z$ and $\hat{S}_z$ operators, can be written as closed expressions. For the sake of completeness, we will do the full derivation (it is not very long). Let us expand the inner product and rewrite $\hat{L}_{x,y}$ and $\hat{S}_{x,y}$ in terms of $\hat{L}_\pm$ and $\hat{S}_\pm$. These are called the raising and lowering operators and are given by

$$\hat{L}_\pm = \hat{L}_x \pm i\hat{L}_y\,, \tag{3.4.26}$$

$$\hat{S}_\pm = \hat{S}_x \pm i\hat{S}_y\,. \tag{3.4.27}$$

These expressions can be rewritten to

$$\hat{L}_x = \frac{1}{2}\left(\hat{L}_+ + \hat{L}_-\right)\ , \tag{3.4.28}$$

$$\hat{L}_y = \frac{-i}{2}\left(\hat{L}_+ - \hat{L}_-\right)\ , \tag{3.4.29}$$

$$\hat{S}_x = \frac{1}{2}\left(\hat{S}_+ + \hat{S}_-\right)\ , \tag{3.4.30}$$

$$\hat{S}_y = \frac{-i}{2}\left(\hat{S}_+ - \hat{S}_-\right)\ . \tag{3.4.31}$$

The inner product $\hat{L}\cdot\hat{S}$ then becomes

$$\begin{aligned}\hat{L}\cdot\hat{S} &= \hat{L}_z\hat{S}_z + \hat{L}_x\hat{S}_x + \hat{L}_y\hat{S}_y \\ &= \hat{L}_z\hat{S}_z + \frac{1}{4}\left(\hat{L}_+ + \hat{L}_-\right)\left(\hat{S}_+ + \hat{S}_-\right) - \frac{1}{4}\left(\hat{L}_+ - \hat{L}_-\right)\left(\hat{S}_+ - \hat{S}_-\right) \\ &= \hat{L}_z\hat{S}_z + \frac{1}{2}\hat{L}_+\hat{S}_- + \frac{1}{2}\hat{L}_-\hat{S}'_+,.\end{aligned}$$

The action of $\hat{L}_\pm$, $\hat{L}_z$, $\hat{S}_\pm$ and $\hat{S}_z$ on a general state $|lmsm_s\rangle$ is given by

$$\begin{aligned}
\hat{L}_\pm |lmsm_s\rangle &= \hbar\sqrt{l(l+1)-m(m\pm 1)}\,|l(m\pm 1)sm_s\rangle && (3.4.32)\\
\hat{L}_z |lmsm_s\rangle &= \hbar m\,|lmsm_s\rangle && (3.4.33)\\
\hat{S}_\pm |lmsm_s\rangle &= \hbar\sqrt{s(s+1)-m_s(m_s\pm 1)}\,|lms(m_s\pm 1)\rangle && (3.4.34)\\
\hat{S}_z |lmsm_s\rangle &= \hbar m_s\,|lmsm_s\rangle \ . && (3.4.35)
\end{aligned}$$

The action of the $\hat{L}\cdot\hat{S}$ operator is

$$\begin{aligned}
\hat{L}\cdot\hat{S}\,|lmsm_s\rangle &= \hbar^2 m m_s\,|lmsm_s\rangle\\
&+\frac{1}{2}\hbar^2\sqrt{l(l+1)-m(m+1)}\sqrt{s(s+1)-m_s(m_s-1)}\,|l(m+1)s(m_s-1)\rangle\\
&+\frac{1}{2}\hbar^2\sqrt{l(l+1)-m(m-1)}\sqrt{s(s+1)-m_s(m_s+1)}\,|l(m-1)s(m_s+1)\rangle \ .
\end{aligned} \tag{3.4.36}$$

At this point we set our value for the spin $s=\frac{1}{2}$, $m_s=\pm\frac{1}{2}$ and rewrite $\sigma := m_s$ to have uniform notation over the document.

$$\begin{aligned}
\hat{L}\cdot\hat{S}\,|lm\sigma\rangle &= \hbar^2 m\sigma\,|lm\sigma\rangle\\
&+\frac{1}{2}\hbar^2\sqrt{l(l+1)-m(m+1)}\sqrt{\frac{3}{4}-\sigma(\sigma-1)}\,|l(m+1)(\sigma-1)\rangle\\
&+\frac{1}{2}\hbar^2\sqrt{l(l+1)-m(m-1)}\sqrt{\frac{3}{4}-\sigma(\sigma+1)}\,|l(m-1)(\sigma+1)\rangle \ .
\end{aligned} \tag{3.4.37}$$

Orthogonality of the states $|lm\sigma\rangle$ ensures that most matrix elements are zero. Left-multiplying by $\langle l'm'\sigma'|$ gives

$$\begin{aligned}
\langle l'm'\sigma'|\,\hat{L}\cdot\hat{S}\,|lm\sigma\rangle &= \hbar^2 m\sigma\delta_{l',l}\delta_{m',m}\delta_{\sigma',\sigma} && (3.4.38)\\
&+\frac{1}{2}\hbar^2\sqrt{l(l+1)-m(m+1)}\delta_{l',l}\delta_{m',m+1}\delta_{\sigma',\sigma-1} && (3.4.39)\\
&+\frac{1}{2}\hbar^2\sqrt{l(l+1)-m(m-1)}\delta_{l',l}\delta_{m',m-1}\delta_{\sigma',\sigma+1}\,. && (3.4.40)
\end{aligned}$$

As an example, let us consider the $l=1$ states. In matrix representation, the $\hat{L}\cdot\hat{S}$ operator can be written as

$$\hat{L}\cdot\hat{S} = \hbar^2\begin{pmatrix}
\frac{-1}{2} & & & & \frac{1}{\sqrt{2}} & \\
 & 0 & & & & \frac{1}{\sqrt{2}}\\
 & & \frac{1}{2} & & & \\
 & & & \frac{1}{2} & & \\
\frac{1}{\sqrt{2}} & & & & 0 & \\
 & \frac{1}{\sqrt{2}} & & & & \frac{-1}{2}
\end{pmatrix}\,, \tag{3.4.41}$$

where the empty entries are all zero, and we have ordered based on spin first, and on m second, i.e. $\{\sigma,m\}=\{\frac{-1}{2},-1\}$, $\{\frac{-1}{2},0\}$, $\{\frac{-1}{2},1\}$, $\{\frac{1}{2},-1\}$, $\{\frac{1}{2},0\}$, $\{\frac{1}{2},1\}$. More generally, we can write the matrix as

$$\hat{L}\cdot\hat{S} = \hbar^2\begin{pmatrix}
\hat{L}_z\hat{S}_z & \frac{1}{2}\hat{L}_-\hat{S}_+\\
\frac{1}{2}\hat{L}_+\hat{S}_- & \hat{L}_z\hat{S}_z
\end{pmatrix}\ . \tag{3.4.42}$$

In the EMTO and LMTO code, we always work with real spherical harmonics ("cubic" harmonics), which are linear combinations of the complex spherical harmonics which directly correspond to the $|lm\rangle$ states mentioned above. The transformation from complex spherical harmonics to real ones is

$$Y_{lm} = \begin{cases} \frac{i}{\sqrt{2}} \left(Y_l^m - (-1)^m Y_l^{-m} \right) & \text{if } m < 0\,, \\ Y_l^0 & \text{if } m = 0\,, \\ \frac{1}{\sqrt{2}} \left(Y_l^{-m} + (-1)^m Y_l^m \right) & \text{if } m > 0\,, \end{cases} \tag{3.4.43}$$

which allow us to express the transformation from complex harmonics to real ones via a matrix, e.g. for $l = 1$

$$T_{Y_1^m \to Y_{1m}} = \begin{pmatrix} \frac{i}{\sqrt{2}} & 0 & \frac{i}{\sqrt{2}} \\ 0 & 1 & 0 \\ \frac{1}{\sqrt{2}} & 0 & \frac{-1}{\sqrt{2}} \end{pmatrix} . \tag{3.4.44}$$

The conventional *spdf*-etc atomic states are in fact assembled out of complex spherical harmonics in this way. Because it is a basis transformation, the matrix is unitary, meaning its Hermitian conjugate and its inverse are the same

$$T_{Y_{lm} \to Y_l^m} = T^{-1}_{Y_l^m \to Y_{lm}} = T^{\dagger}_{Y_l^m \to Y_{lm}} = \begin{pmatrix} \frac{-i}{\sqrt{2}} & 0 & \frac{1}{\sqrt{2}} \\ 0 & 1 & 0 \\ \frac{-i}{\sqrt{2}} & 0 & \frac{-1}{\sqrt{2}} \end{pmatrix} . \tag{3.4.45}$$

We can use these properties to construct the $\hat{L} \cdot \hat{S}$ matrix in the Y_{lm} basis of real spherical harmonics, which the EMTO and LMTO codes use.

4. GALERKIN METHOD

Rather than the physically motivated schemes presented in the previous section, the current section is concerned with a more mathematically involved scheme for solving Schrödinger's equation. Indeed, rather than starting from the Schrödinger equation and approximating our way to a feasible scheme, we consider the equation as-is. This gives much flexibility with regards to the potentials for which one can solve the quantum mechanical problem, although there is a considerable tradeoff in efficiency. This section is largely based on [11, 7, 15].

4.1 Local discontinuous Galerkin

The local discontinuous Galerkin method we will we discussing is one in a class of finite-element methods for solving partial differential equations. The idea is simple: one divides the region of interest into a discrete set of elements and solves two separate problems. The first being the differential equation for each element, and secondly the problem of connecting all the finite elements together. Let us consider the 1D Schrödinger equation.

$$iu_t + u_{xx} - Vu = 0\,, \tag{4.1.1}$$

on some domain $x \in [0, a]$. Here, a subscript denotes a derivative with respect to that variable. We divide the interval $[0, a]$ into a mesh of N new intervals $I_j = [x_{j-\frac{1}{2}}, x_{j+\frac{1}{2}}]$, where $j = 1, 2, ..., N$. Let us call these new intervals 'cells'. Each cell has a width of $\Delta x = x_{j+\frac{1}{2}} - x_{j-\frac{1}{2}}$ and a center $x_j = \left(x_{j-\frac{1}{2}} - x_{j+\frac{1}{2}}\right)/2$. The crux of the Galerkin method is to construct the solution of the partial differential equation for the whole domain as a combination of solutions in each cell. Specifically, the solution within each cell shall be some carefully constructed polynomial function. The functions exist in the space

$$\mathbb{V}_{\Delta x} := \{v : v \in P^{(k)}(I_j) \text{ for } x \in I_j, j = 1, 2, ..., N\}\,. \tag{4.1.2}$$

Although we are now armed with a systematically improvable basis set, there is still no clear computational scheme. In order to arrive at one, some modifications to the Schrödinger equation must be made. Rather than solving the partial differential equation as presented, we will multiply it by some test function v, and integrate over the domain.

$$i\int u_t v dx + \int u_{xx} v dx - \int V u v dx = 0 \tag{4.1.3}$$

The function v is called a test function. If we restrain ourselves to finding u which solves this equation for any function v, we are solving the same problem the original PDE poses. This equation is called the *weak form* of the original PDE. It is less restrictive than the original equation, as the integral as an operator dismisses any null sets from the functions.

As we have divided our domain into cells, the integrals of (4.1.2) can be split into equations for each cell separately. This is where the *local discontinuous* part of the scheme comes in. Since we solve the integrals for each cell separately, a choice must be made in how one handles the interfaces between the cells. An obvious choice is to force the function to be continuous, so that the function value at the rightmost point of I_j equals the function value at the leftmost point of I_{j+1}. In reality, this turns out to be an unnecessarily harsh restriction, which the local discontinuous Galerkin method lifts. Instead of forcing a continuity, the method carefully constructs a 'numerical flux' which determines the behaviour at the cell interfaces. As stated earlier, we are only considering solutions u which are part of the polynomial space for I_j. Instead of allowing v to be any function, let us restrict v to the same function space.

In order to properly discretize the problem, let us transform it into a set of first-order problems, rather than a single second-order problem. If we simply set

$$p = u_x \tag{4.1.4}$$

the final problem is the following.

Find $u, p \in \mathbb{V}_{\Delta x}$, $\forall v, w \in \mathbb{V}_{\Delta x}$, such that

$$\begin{aligned} i\int_{I_j} u_t v dx - \int_{I_j} p v_x dx + \hat{p}v|_{j-\frac{1}{2}}^{j+\frac{1}{2}} - \int_{I_j} V u v dx = 0 \\ \int_{I_j} p w dx + \int_{I_j} u w_x dx - \hat{u}w|_{j-\frac{1}{2}}^{j+\frac{1}{2}} = 0\,, \end{aligned} \tag{4.1.5}$$

where the hats denote the numerical fluxes.

The ± superscripts denote the function values at the interfaces. The minus superscript indicates the function value at the leftmost point of the right cell, and the plus superscript denotes the rightmost point of the left cell. In principle, one can freely choose the numerical fluxes (as long as one can prove that the resulting scheme is stable and consistent). We choose a particular set of fluxes which has been shown to be stable and accurate. One notices that we have to choose a flux not only for the function itself, but also for its derivative. One choice of fluxes is a purely symmetrical one:

$$\begin{aligned} \hat{u} &= \left(u^+ + u^-\right)/2\,, \\ \hat{p} &= \left(p^+ + p^-\right)/2\,, \end{aligned} \tag{4.1.6}$$

but this choice turns out not to be stable for all cases. Interestingly, a very stable flux is

$$\begin{aligned} \hat{u} &:= u^- \\ \hat{p} &:= p^+ \end{aligned} \tag{4.1.7}$$

i.e. an upwind flux for the function value and a downwind flux for the derivative. The proof of stability for this choice can be found in [11].

As stated before, the solution inside each cell is a polynomial. The usual choice for constructing this function is to use Lagrange basis functions, which automatically satisfy orthogonality in the sense that $\lambda_i(x_j) = \delta_{ij}$, where λ_i is a Lagrange polynomial and x_j is some point on the grid within any given cell. Logically, the solution depends on the choice of grid, so choosing one is not trivial. The properties of different grid choices and the mathematics behind them are beyond the scope of this report. We will use a grid based on Legendre-Gauss-Lobatto quadrature points as proposed in [3].

Extending the scheme to two dimensions is relatively simple. The 2D Schrödinger equation is

$$iu_t + u_{xx} + u_{yy} - Vu = 0\,, \tag{4.1.8}$$

which can be transformed into a set of first-order problems in much the same way as the 1D equation. We set $p = u_x$ and $q = u_y$ and formulate the weak form.

$$\begin{aligned} i\int_K u_t v\,dxdy + \int_K p_x v\,dxdy + \int_K q_y v\,dxdy - \int_K Vuv\,dxdy &= 0 \\ \int_K pw\,dxdy - \int_K u_x w\,dxdy &= 0 \\ \int_K qz\,dxdy - \int_K u_y z\,dxdy &= 0\,. \end{aligned} \tag{4.1.9}$$

In the above, v, w and z are test functions, and K is a given cell. After we integrate by parts, we find the final problem.

$$\begin{aligned} i\int_K u_t v\,dxdy - \int_K p v_x\,dxdy - \int_K q v_y\,dxdy - \int_K Vuv\,dxdy + \int_{\partial K} p\hat{}_{n_x} v\,ds + \int_{\partial K} q\hat{}_{n_y} v\,ds &= 0\,, \\ \int_K pw\,dxdy + \int_K u w_x\,dxdy - \int_{\partial K} u\hat{}_{n_x} w\,ds &= 0\,, \\ \int_K qz\,dxdy + \int_K u z_y\,dxdy - \int_{\partial K} u\hat{}_{n_y} w\,ds &= 0\,. \end{aligned} \tag{4.1.10}$$

The similarities between the 1D and 2D scheme are immediately obvious. It is mostly the surface integrals that change, since rather than one point on each boundary, we now have to consider the actual surface integral. If we consider square cells, the basis functions remain the same, only with an added dimension. The solution to the partial differential equation is then approximated as

$$u(x, y) \approx u^h(x, y) = \sum_{i,j} u(x_i, y_j)\ell_i(x)\ell_j(y)\,, \tag{4.1.11}$$

so that we can recycle most 1D routines to work for the 2D case. The fluxes become slightly more involved. For vertical faces between square elements, we still consider right and left sides and choose the fluxes appropriately. Additionally, we have horizontal faces, where we can use the same trick.

$$\begin{aligned} u\hat{}_{n_x} &= u^- n_x\,, \\ u\hat{}_{n_y} &= u^- n_y\,, \\ p\hat{}_{n_x} &= p^+ n_x\,, \\ q\hat{}_{n_y} &= q^+ n_y\,, \end{aligned} \tag{4.1.12}$$

where $(n_x,\ n_y)$ are the outward facing normals along ∂K and the superscript $(+,\ -)$ denotes function on the "left" and "right" sides of the edge respectively.

4.2 Implementation

In order to go from a set of equations to a computational scheme, a few more steps need to be taken. First, let us define the 1D mass and stiffness matrices,

$$\begin{aligned} \mathcal{M}_{ij} &= \int_I \ell_i(x)\ell_j(x)dx \\ \mathcal{S}_{ij} &= \int_I \ell_i(x)\frac{\partial \ell_j}{\partial x}dx\,. \end{aligned} \tag{4.2.1}$$

If we insert our approximation to the solution, as well as inserting the test function $\ell_j(x)$, we can write our 1D problem in terms of matrix-vector multiplications.

$$\begin{aligned} i\mathcal{M}\frac{d\mathbf{u}}{dt} - \mathcal{S}\mathbf{p} + \int_{\partial I_j} \hat{n}\cdot\hat{\mathbf{p}}\,ds - \mathcal{M}V\mathbf{u} &= 0 \\ \mathcal{M}\mathbf{p} + \mathcal{S}\mathbf{u} - \int_{\partial I_j} \hat{n}\cdot\hat{\mathbf{u}}\,ds &= 0\,. \end{aligned} \tag{4.2.2}$$

The unknowns are $\mathbf{u}$ and $\mathbf{p}$ respectively. V is a diagonal matrix containing the potentials $V(x_i)$.

$$\begin{aligned} \frac{d\mathbf{u}}{dt} &= -iV\mathbf{u} - i\mathcal{M}^{-1}\mathcal{S}\mathbf{p} + i\mathcal{M}^{-1}\int_{\partial I_j} \hat{n}\cdot\hat{\mathbf{p}}\,ds \\ \mathbf{p} &= -\mathcal{M}^{-1}\mathcal{S}\mathbf{u} + \mathcal{M}^{-1}\int_{\partial I_j} \hat{n}\cdot\hat{\mathbf{u}}\,ds \end{aligned} \tag{4.2.3}$$

Omitting the derivation which can be found in [3], let us define the matrix $\mathcal{D}_{ij} = \frac{d\ell_j}{dr}\Big|_{r_i}$ which satisfies

$$\mathcal{D} = \mathcal{M}^{-1}\mathcal{S}\,. \tag{4.2.4}$$

Because of the last step, our algorithm does not have to explicitely calculate the mass and stiffness matrices, but instead only the differentation matrix $\mathcal{D}$. The surface integrals have to be lifted into the correct dimensionality, and require separate treatment. Here, the inverse of the mass matrix is calculated through the generalized Vandermonde matrix, which is related to the Legendre-Gauss-Lobatto grid points which were chosen. To be precise, the Vandermonde matrix contains the function values of the Legendre polynomials on the grid points.

$$\mathcal{V}_{ij} = P_j(x_i)\,. \tag{4.2.5}$$

The polynomial interpolation (that is, the Lagrange polynomials) are related to the Legendre polynomials through the Vandermonde matrix,

$$\mathcal{V}^T\ell = \mathbf{P}\,. \tag{4.2.6}$$

The differentation matrix is calculated through the Vandermonde matrix as well. This is the most convenient way, as the Vandermonde matrix is based on Legendre polynomials, the derivatives of which can again be expressed as Legendre polynomials.

Using the same matrices, we can write down a computational scheme for the 2D problem as well. Using square elements, the integrals over K simply become a product of integrals over the intervals which determine K.

$$\begin{aligned}\int_K u_t v\,dxdy &\implies \sum_{i,j} u(x_i,y_j)\int_{I_x}\ell_i^x(x)\ell_k^x(x)\,dx\int_{I_y}\ell_j^y(y)\ell_m^y(y)dy\\ &= \sum_{i,j} u(x_i,y_j)\mathcal{M}_{ik}^x\mathcal{M}_{jm}^y\end{aligned} \tag{4.2.7}$$

Using a compound index for i and j together then lets us describe the operator as a matrix again.

$$\int_K u_t v\,dxdy \implies \mathcal{M}^x\otimes\mathcal{M}^y\mathbf{u} \tag{4.2.8}$$

The 2D problem can be written as

$$\begin{aligned} i\left(\mathcal{M}^x\otimes\mathcal{M}^y\right)\frac{d\mathbf{u}}{dt} - \left(\mathcal{S}^x\otimes\mathcal{M}^y\right)\mathbf{p} - \left(\mathcal{M}^x\otimes\mathcal{S}^y\right)\mathbf{q} - \left(\mathcal{M}^x\otimes\mathcal{M}^y\right)V\mathbf{u} + \int_{\partial K}\hat{n}_x\cdot\hat{\mathbf{p}}\,ds +&\\ \int_{\partial K}\hat{n}_y\cdot\hat{\mathbf{q}}\,ds &= 0\,,\\ \left(\mathcal{M}^x\otimes\mathcal{M}^y\right)\mathbf{p} + \left(\mathcal{S}^x\otimes\mathcal{M}^y\right)\mathbf{u} - \int_{\partial K}\hat{n}_x\cdot\mathbf{u}\,ds &= 0\,,\\ \left(\mathcal{M}^x\otimes\mathcal{M}^y\right)\mathbf{q} + \left(\mathcal{M}^x\otimes\mathcal{S}^y\right)\mathbf{u} - \int_{\partial K}\hat{n}_y\cdot\mathbf{u}\,ds &= 0\,.\end{aligned} \tag{4.2.9}$$

We remind ourselves of some of the properties of the Kronecker product. First, the product $\mathbf{A}\otimes\mathbf{B}$ is invertible if and only if $\mathbf{A}$ and $\mathbf{B}$ are invertible, in which case

$$\left(\mathbf{A}\otimes\mathbf{B}\right)^{-1} = \mathbf{B}^{-1}\otimes\mathbf{A}^{-1}\,. \tag{4.2.10}$$

We will also use the mixed-product property, which is

$$\left(\mathbf{A}\otimes\mathbf{B}\right)\left(\mathbf{C}\otimes\mathbf{D}\right) = \left(\mathbf{AC}\right)\otimes\left(\mathbf{BD}\right)\,. \tag{4.2.11}$$

Choosing square elements also results in $\mathcal{M}^x = \mathcal{M}^y$, so that we can write

$$\begin{aligned}\left(\mathcal{M}^x\otimes\mathcal{M}^y\right)^{-1}\left(\mathcal{M}^x\otimes\mathcal{S}^y\right) &= \left((\mathcal{M}^y)^{-1}\otimes(\mathcal{M}^x)^{-1}\right)\left(\mathcal{M}^x\otimes\mathcal{S}^y\right)\\ &= \left((\mathcal{M}^y)^{-1}\mathcal{M}^x\right)\otimes\left((\mathcal{M}^x)^{-1}\mathcal{S}^y\right)\\ &= \mathbb{I}\otimes\mathcal{M}^{-1}\mathcal{S}\\ &= \mathbb{I}\otimes\mathcal{D}\end{aligned}$$

and similarly

$$\left(\mathcal{M}^x\otimes\mathcal{M}^y\right)^{-1}\left(\mathcal{S}^x\otimes\mathcal{M}^y\right) = \mathcal{D}\otimes\mathbb{I}\,.$$

The computational scheme for the 2D problem becomes

$$\begin{aligned}
\frac{d\mathbf{u}}{dt} &= -i\left(\mathcal{D}\otimes\mathbb{I}\right)\mathbf{p} - i\left(\mathbb{I}\otimes\mathcal{D}\right)\mathbf{q} - iV\mathbf{u} + i\left(\mathcal{M}^x\otimes\mathcal{M}^y\right)^{-1}\left[\int_{\partial K}\hat{n}_x\cdot\hat{\mathbf{p}}\,ds + \int_{\partial K}\hat{n}_y\cdot\hat{\mathbf{q}}\,ds\right],\\
\mathbf{p} &= -\left(\mathcal{D}\otimes\mathbb{I}\right)\mathbf{u} + \left(\mathcal{M}^x\otimes\mathcal{M}^y\right)^{-1}\int_{\partial K}\hat{n}_x\cdot\mathbf{u}\,ds\,,\\
\mathbf{q} &= -\left(\mathbb{I}\otimes\mathcal{D}\right)\mathbf{u} + \left(\mathcal{M}^x\otimes\mathcal{M}^y\right)^{-1}\int_{\partial K}\hat{n}_y\cdot\mathbf{u}\,ds\,.
\end{aligned} \tag{4.2.12}$$

The only remaining point of interest is the integration over time. For this, we could use a simple fourth order Runge-Kutta scheme. Here, the solution at time $n+1$ can be related to the solution at time n as

$$\mathbf{u}^{n+1} = \mathbf{u}^n + \frac{1}{6}\Delta t\left(\mathbf{k}^{(1)} + 2\mathbf{k}^{(2)} + 2\mathbf{k}^{(3)} + \mathbf{k}^{(4)}\right), \tag{4.2.13}$$

where the coefficients $\mathbf{k}^{(i)}$ are given by

$$\begin{aligned}
\mathbf{k}^{(1)} &= \mathcal{L}(\mathbf{u}^n, t)\\
\mathbf{k}^{(2)} &= \mathcal{L}(\mathbf{u}^n + \frac{1}{2}\Delta t\mathbf{k}^{(1)}, t^n + \frac{1}{2}\Delta t)\\
\mathbf{k}^{(3)} &= \mathcal{L}(\mathbf{u}^n + \frac{1}{2}\Delta t\mathbf{k}^{(2)}, t^n + \frac{1}{2}\Delta t)\\
\mathbf{k}^{(4)} &= \mathcal{L}(\mathbf{u}^n + \Delta t\mathbf{k}^{(3)}, t^n + \Delta t)\,.
\end{aligned} \tag{4.2.14}$$

The $\mathcal{L}$ is a short-hand notation for the right hand side of the relevant equation. This method is widely used, as it is stable and simple. Its large disadvantage is the fact that all vectors $\mathbf{k}^{(i)}$ have to be stored simultaneously, leading to large memory usage. We use a low-memory version [14] of the fourth order Runge-Kutta method (based on a higher order version of the one proposed in [8]), given by

$$\begin{aligned}
\mathbf{p}^{(0)} &= \mathbf{u}^n\\
i\in[1,...,5]: &\begin{cases}\mathbf{k}^{(i)} & = a_i\mathbf{k}^{(i-1)} + \Delta t\mathcal{L}(\mathbf{p}^{(i-1)}, t^n + c_i\Delta t)\\ \mathbf{p}^{(i)} & = \mathbf{p}^{(i-1)} + b_i\mathbf{k}^{(i)}\end{cases}\\
\mathbf{u}^{n+1} &= \mathbf{p}^{(5)}\,.
\end{aligned} \tag{4.2.15}$$

The coefficients a_i, b_i and c_i are tabulated and can be found in table 4.1.

Tab. 4.1: Coefficients of the low-storage explicit Runge-Kutta method [14, 8].

i	a_i	b_i	c_i
1	0	$\frac{1432997174477}{9575080441755}$	0
2	$-\frac{567301805773}{1357537059087}$	$\frac{5161836677717}{13612068292357}$	$\frac{1432997174477}{9575080441755}$
3	$-\frac{2404267990393}{2016746695238}$	$\frac{1720146321549}{2090206949498}$	$\frac{2526269341429}{6820363962896}$
4	$-\frac{3550918686646}{2091501179385}$	$\frac{3134564353537}{4481467310338}$	$\frac{2006345519317}{3224310063776}$
5	$-\frac{1275806237668}{842570457699}$	$\frac{2277821191437}{14882151754819}$	$\frac{2802321613138}{2924317926251}$

5. DERIVATIONS

In the present section, we derive expressions for the Hamiltonian matrix elements of the SOC and non-spherical terms in the potentials in terms of a basis of "Kinked Partial Waves" (KPW). which are not readily available in the literature and present algorithms to solve those problems we have derived expressions for. We use the knowledge presented in the previous section, as well as the expressions derived there, to arrive at schemes which can be readily implemented into the code.

5.1 SOC for KPWs

A Kinked Partial Wave (KPW) Φ consists of three terms. The first is the usual partial wave ϕ, the second is the so-called back-extrapolated partial wave φ, and the third is the screened spherical wave (SSW) ψ. Below, we abbreviate $L := lm$ and neglect any energy dependences, since everything happens at a chosen energy (usually the Fermi energy),

$$|\Phi\rangle = |\phi\rangle - |\varphi\rangle + |\psi\rangle \ . \tag{5.1.1}$$

The partial waves are variable-separated functions, i.e. they are of the form

$$|\phi\rangle = \sum_{L} \phi_l(r) Y_L(\theta,\phi) \tag{5.1.2}$$

$$|\varphi\rangle = \sum_{L} \varphi_l(r) Y_L(\theta,\phi) \, , \tag{5.1.3}$$

where the ϕ_l and φ_l functions are solutions to the radial Schrödinger equation.

The SSW for an atom at $\mathbf{R}$ takes the form

$$\psi_{\mathbf{R}L} = \sum_{\mathbf{R}'L'} \left[n^{\alpha}_{\mathbf{R}'L} Y_{\mathbf{R}'L'} \delta_{\mathbf{R}',\mathbf{R}} \delta_{L',L} - j^{\alpha}_{\mathbf{R}'L} Y_{\mathbf{R}'L'} S^{\alpha}_{\mathbf{R}'L',\mathbf{R}L} \right] \ . \tag{5.1.4}$$

The radial functions n^{α} and j^{α} are linear combinations of spherical Bessel and Neumann functions:

$$n^{\alpha}_{\mathbf{R}L} = t^{(1)}_{\mathbf{R}l} n_l + t^{(2)}_{\mathbf{R}l} j_l \, , \tag{5.1.5}$$

$$j^{\alpha}_{\mathbf{R}L} = t^{(3)}_{\mathbf{R}l} n_l + t^{(4)}_{\mathbf{R}l} j_l \, . \tag{5.1.6}$$

The t_i parameters are determined by the boundary conditions on the SSW. The four t_i parameters together with the unscreened structure constants, which are

$$S^{0}_{\mathbf{R}'L,\mathbf{R}L} = -4\pi \sum_{l''} \frac{2\left(\kappa\omega\right)^{l+l'-l''} (2l''-1)!!}{(2l'-1)!!\,(2l-1)!!} C_{LL'L''} (-1)^{-l} Y_{L''}(\mathbf{R} \,\hat{-}\, \mathbf{R}\ ) n_l(|\mathbf{R}-\mathbf{R}'|) \, , \tag{5.1.7}$$

form the screened structure constants

$$S^{\alpha}_{\mathbf{R}'L,\mathbf{R}L} = \frac{t^{(1)}_{\mathbf{R}l}}{t^{(3)}_{\mathbf{R}l}}\delta_{\mathbf{R}',\mathbf{R}}\delta_{L',L} + \frac{1}{t^{(3)}_{\mathbf{R}'l'}}\left[-\frac{t^{(4)}}{t^{(3)}} - S^0\right]^{-1}_{\mathbf{R}'L,\mathbf{R}L}\frac{1}{t^{(3)}_{\mathbf{R}l}}\left[t^{(1)}_{\mathbf{R}l}t^{(4)}_{\mathbf{R}l} - t^{(2)}_{\mathbf{R}l}t^{(3)}_{\mathbf{R}l}\right] . \tag{5.1.8}$$

The SOC Hamiltonian is of the form

$$\hat{H}_{\mathrm{soc}} = \frac{1}{c^2 r}\frac{dV(r)}{dr}\hat{L}\cdot\hat{S} , \tag{5.1.9}$$

such that the matrix elements we are looking for are

$$\begin{aligned}\langle\Phi|\,\hat{H}_{\mathrm{soc}}\,|\Phi\rangle &= \langle\phi-\varphi+\psi|\,\hat{H}_{\mathrm{soc}}\,|\phi-\varphi+\psi\rangle \\ &= \langle\phi-\varphi|\,\hat{H}_{\mathrm{soc}}\,|\phi-\varphi\rangle + \langle\phi-\varphi|\,\hat{H}_{\mathrm{soc}}\,|\psi\rangle + \langle\psi|\,\hat{H}_{\mathrm{soc}}\,|\phi-\varphi\rangle + \langle\psi|\,\hat{H}_{\mathrm{soc}}\,|\psi\rangle \ .\end{aligned}$$

The first term is relatively simple. It involves an integral over r, θ, ϕ of the product of partial waves, which allows us to split the integral, since the partial waves are explicitely variable-separated.

$$\langle\phi-\varphi|\,\hat{H}_{\mathrm{soc}}\,|\phi-\varphi\rangle = \mathbf{M}\otimes\xi ,$$

where we have defined matrices

$$\mathbf{M}_{lm\sigma,l'm'\sigma'} = \langle lm\sigma|\,\hat{L}\cdot\hat{S}\,|l'm'\sigma'\rangle \ ,$$

and

$$\begin{aligned}\xi_{l\sigma\sigma'} &= \int\left(\phi_{l\sigma}(r) - \varphi_{l\sigma}(r)\right)^{\dagger}\frac{1}{c^2 r}\frac{dV^{\sigma\sigma'}(r)}{dr}\left(\phi_{l\sigma'}(r) - \varphi_{l'\sigma'}(r)\right)r^2 dr \\ &= \langle\phi_{l\sigma} - \varphi_{l\sigma}|\,\frac{1}{c^2 r}\frac{dV^{\sigma\sigma'}(r)}{dr}\,|\phi_{l\sigma'} - \varphi_{l\sigma'}\rangle \ .\end{aligned}$$

This is precisely the scheme in which SOC is implemented in the LMTO code. The first part can be explicitly calculated by integrating over the potential sphere, and the second part are known values (see 3.4.6). Implementing this for the KPWs is straightforward, and almost all of the old code can be copied and pasted to work for the KPWs.

The expansion of any SSW in spherical waves at any other site has been given in (3.4.7). It is

$$\begin{aligned}\psi_{\mathbf{R}L} &= n^{\alpha}_{\mathbf{R}'L}Y_{\mathbf{R}'L}\delta_{\mathbf{R}',\mathbf{R}} - \sum_{L'} j^{\alpha}_{\mathbf{R}'l'}Y_{\mathbf{R}'L'}S^{\alpha}_{\mathbf{R}'L',\mathbf{R}L} \\ &= \left(n_{\mathbf{R}'l}t^{(1)}_{\mathbf{R}'l} + j_{\mathbf{R}'l}t^{(2)}_{\mathbf{R}'l}\right)Y_{\mathbf{R}'L}\delta_{\mathbf{R}',\mathbf{R}} - \sum_{L'}\left(n_{\mathbf{R}'l'}t^{(3)}_{\mathbf{R}'l'} + j_{\mathbf{R}'l'}t^{(4)}_{\mathbf{R}'l'}\right)Y_{\mathbf{R}'L'}S^{\alpha}_{\mathbf{R}'L',\mathbf{R}L} \, .\end{aligned} \tag{5.1.10}$$

In order to find the expression for the SSW originating from $\mathbf{R}$ expressed in spherical waves originating at $\mathbf{R}$, we only have to insert $\mathbf{R}' = \mathbf{R}$. Likewise, we can express the SSW originating in $\mathbf{R}' \neq \mathbf{R}$ into spherical waves originating in $\mathbf{R}$, by substituting $\mathbf{R} \implies \mathbf{R}'$ and $\mathbf{R}' \implies \mathbf{R}$. For completeness, they are

$$\psi_{\mathbf{R}L} = n^{\alpha}_{\mathbf{R}l}Y_{\mathbf{R}L} - \sum_{L'} j^{\alpha}_{\mathbf{R}l'}Y_{\mathbf{R}L'}S^{\alpha}_{\mathbf{R}L',\mathbf{R}L} , \tag{5.1.11}$$

$$\psi_{\mathbf{R}'L} = -\sum_{L'} j^{\alpha}_{\mathbf{R}l'}Y_{\mathbf{R}L'}S^{\alpha}_{\mathbf{R}L',\mathbf{R}'L} \, . \tag{5.1.12}$$

To convince oneself fully that this is the correct expression, let us consider a more complete approach. We start with the most formal expression for the SSW, the sum of spherical Neumann functions originating at every atom.

$$\psi_{\mathbf{R}L} = \sum_{\mathbf{R}'L'} n_{\mathbf{R}'l'} Y_{\mathbf{R}'L'} M_{\mathbf{R}'L',\mathbf{R}L} \,. \tag{5.1.13}$$

Here $n_{\mathbf{R}'l'}$ is the spherical Neumann function of order l' centered at $\mathbf{R}'$. The quantity $M_{\mathbf{R}'L',\mathbf{R}L}$ contains all the screening information and is given by

$$M_{\mathbf{R}'L',\mathbf{R}L} = \left(t^{(1)}_{\mathbf{R}L} \delta_{\mathbf{R}',\mathbf{R}} \delta_{L',L} - t^{(3)}_{\mathbf{R}'L'} S^{\alpha}_{\mathbf{R}'L',\mathbf{R}L} \right) \tag{5.1.14}$$

$$\sum_{\mathbf{R}''L''} S^{0}_{\mathbf{R}'L',\mathbf{R}''L''} M_{\mathbf{R}''L'',\mathbf{R}L} = -\left(t^{(2)}_{\mathbf{R}L} \delta_{\mathbf{R}',\mathbf{R}} \delta_{L',L} - t^{(4)}_{\mathbf{R}'L'} S^{\alpha}_{\mathbf{R}'L',\mathbf{R}L} \right) \,. \tag{5.1.15}$$

Now we use the one-center expansion of $n_{\mathbf{R}'L'} Y_{\mathbf{R}'L'}$ to express the sum over $\mathbf{R}'$ in (5.1.13) solely in terms of spherical waves originating at $\mathbf{R}$.

$$n_{\mathbf{R}'L'} Y_{\mathbf{R}'L'} = n_{\mathbf{R}L} Y_{\mathbf{R}L} \delta_{\mathbf{R}',\mathbf{R}} \delta_{L',L} - \sum_{L} j_{\mathbf{R}L} Y_{\mathbf{R}L} S^{0}_{\mathbf{R}L,\mathbf{R}'L'} \,. \tag{5.1.16}$$

Inserting this expansion into the expression for M gives

$$\begin{aligned}
\psi_{\mathbf{R}L} &= \sum_{\mathbf{R}'L'} n_{\mathbf{R}'l'} Y_{\mathbf{R}'L'} M_{\mathbf{R}'L',\mathbf{R}L} \\
&= \sum_{\mathbf{R}'L'} \left[n_{\mathbf{R}L'} Y_{\mathbf{R}L'} \delta_{\mathbf{R}',\mathbf{R}} - \sum_{L''} j_{\mathbf{R}L''} Y_{\mathbf{R}L''} S^{0}_{\mathbf{R}L'',\mathbf{R}'L'} \right] M_{\mathbf{R}'L',\mathbf{R}L} \\
&= \sum_{L'} n_{\mathbf{R}L'} Y_{\mathbf{R}L'} M_{\mathbf{R}L',\mathbf{R}L} - \sum_{L''} j_{\mathbf{R}L''} Y_{\mathbf{R}L''} \sum_{\mathbf{R}'L'} S^{0}_{\mathbf{R}L'',\mathbf{R}'L'} M_{\mathbf{R}'L',\mathbf{R}L} \,.
\end{aligned}$$

Now we can directly insert the expressions (5.1.15) for M and $\sum S^0 M$.

$$\psi_{\mathbf{R}L} = \sum_{L'} n_{\mathbf{R}L'} Y_{\mathbf{R}L'} \left(t^{(1)}_{\mathbf{R}L} \delta_{\mathbf{R},\mathbf{R}} \delta_{L',L} - t^{(3)}_{\mathbf{R}L'} S^{\alpha}_{\mathbf{R}L',\mathbf{R}L} \right) \tag{5.1.17}$$

$$+ \sum_{L''} j_{\mathbf{R}L''} Y_{\mathbf{R}L''} \left(t^{(2)}_{\mathbf{R}L} \delta_{\mathbf{R},\mathbf{R}} \delta_{L'',L} - t^{(4)}_{\mathbf{R}L''} S^{\alpha}_{\mathbf{R}L'',\mathbf{R}L} \right) \tag{5.1.18}$$

$$= \left(n_{\mathbf{R}l} t^{(1)}_{\mathbf{R}l} + j_{\mathbf{R}l} t^{(2)}_{\mathbf{R}l} \right) Y_{\mathbf{R}L} - \sum_{L'} \left(n_{\mathbf{R}l'} t^{(3)}_{\mathbf{R}l'} + j_{\mathbf{R}l'} t^{(4)}_{\mathbf{R}l'} \right) Y_{\mathbf{R}L'} S^{\alpha}_{\mathbf{R}L',\mathbf{R}L} \,, \tag{5.1.19}$$

which is precisely the expression above. The SSW belonging to $\mathbf{R}'$ expressed in spherical waves originating at $\mathbf{R}$ takes the form

$$\psi_{\mathbf{R}'L} = -\sum_{L'} \left(t^{(3)}_{\mathbf{R}l'} n_{\mathbf{R}l'} + t^{(4)}_{\mathbf{R}l'} j_{\mathbf{R}l'} \right) Y_{\mathbf{R}L'} S^{\alpha}_{\mathbf{R}L',\mathbf{R}'L} \,. \tag{5.1.20}$$

The actual matrix element is on the KPW basis, i.e. $|\Phi\rangle$. The KPWs are distinguished through their $\mathbf{R}L$ label. In the following, we omit $\mathbf{R}$ (but not $\mathbf{R}' \neq \mathbf{R}$ or $\mathbf{R}'' \neq \mathbf{R}$) for clarity.

$$\begin{aligned}
\langle \Phi_{L\sigma} | \hat{H}_{\mathrm{soc}} | \Phi_{L'\sigma'} \rangle &= \langle (\phi_{l\sigma} - \varphi_{l\sigma}) Y_{lm} | \hat{H}_{\mathrm{soc}} | (\phi_{l'\sigma'} - \varphi_{l'\sigma'}) Y_{l'm'} \rangle \\
&\quad + \langle \psi_{L\sigma} | \hat{H}_{\mathrm{soc}} | (\phi_{l'\sigma'} - \varphi_{l'\sigma'}) Y_{l'm'} \rangle \\
&\quad + \langle (\phi_{l\sigma} - \varphi_{l\sigma}) Y_{lm} | \hat{H}_{\mathrm{soc}} | \psi_{L'\sigma'} \rangle + \langle \psi_{L} | \hat{H}_{\mathrm{soc}} | \psi_{L'\sigma'} \rangle
\end{aligned}$$

This is the simplest matrix element. The matrix elements of $\hat{L}\cdot\hat{S}$ are such that any element with $l \neq l'$ vanishes

$$\begin{aligned}
&\langle(\phi_{l\sigma}-\varphi_{l\sigma})\,Y_{lm}|\hat{H}_{\mathrm{soc}}\,|(\phi_{l'\sigma'}-\varphi_{l'\sigma'})\,Y_{l'm'}\rangle \\
&\qquad = \iiint r^2\sin\theta dr d\theta d\phi\,(\phi_{l\sigma}(r)-\varphi_{l\sigma}(r))^\dagger\,Y^\dagger_{lm}\frac{1}{c^2r}\frac{dV^{\sigma\sigma'}}{dr}\hat{L}\cdot\hat{S}\,(\phi_{l'\sigma'}-\varphi_{l'\sigma'})\,Y_{l'm'} \\
&\qquad = \int r^2dr\;(\phi_{l\sigma}-\varphi_{l\sigma})^\dagger\,\frac{1}{c^2r}\frac{dV^{\sigma\sigma'}}{dr}\,(\phi_{l'm'}-\varphi_{l'm'})\iint\sin\theta d\phi d\theta\,Y^\dagger_{lm}\hat{L}\cdot\hat{S}\,Y_{l'm'} \\
&\qquad = \langle\phi_{l\sigma}-\varphi_{l\sigma}|\,\frac{1}{c^2r}\frac{dV^{\sigma\sigma'}}{dr}\,|\phi_{l\sigma'}-\varphi_{l\sigma'}\rangle\,\langle lm\sigma|\,\hat{L}\cdot\hat{S}\,|l'm'\sigma'\rangle\;,
\end{aligned} \tag{5.1.21}$$

$$\begin{aligned}
&\langle\phi_{L\sigma}|\hat{H}_{\mathrm{soc}}\,|(\phi_{l'\sigma'}-\varphi_{l'\sigma'})\,Y_{l'm'}\rangle \\
&\quad = \iiint r^2\sin\theta dr d\theta d\phi\left[\left(n_lt^{(1)}_l+j_lt^{(2)}_l\right)S^\alpha_{\mathbf{R}L'',\mathbf{R}L}Y_{lm}-\sum_{L''}\left(n_{l''}t^{(3)}_{l''}+j_{l''}t^{(4)}_{l''}\right)Y_{l''m''}\right]^\dagger \\
&\quad \times\frac{1}{c^2r}\frac{dV^{\sigma\sigma'}}{dr}\hat{L}\cdot\hat{S}\,(\phi_{l'\sigma'}-\varphi_{l'\sigma'})\,Y_{l'm'} \\
&\quad = \left\langle n_lt^{(1)}_{l\sigma}+j_lt^{(2)}_{l\sigma}-\left(n_lt^{(3)}_{l\sigma}+j_lt^{(4)}_{l\sigma}\right)S^\alpha_{\mathbf{R}L,\mathbf{R}L}\right|\frac{1}{c^2r}\frac{dV^{\sigma\sigma'}}{dr}\,|\phi_{l\sigma'}-\varphi_{l\sigma'}\rangle\,\langle lm\sigma|\,\hat{L}\cdot\hat{S}\,|l'm'\sigma'\rangle \\
&\quad -\left\langle n_lt^{(3)}_{l\sigma}+j_lt^{(4)}_{l\sigma}\right|\frac{1}{c^2r}\frac{dV^{\sigma\sigma'}}{dr}\,|\phi_{l\sigma'}-\varphi_{l\sigma'}\rangle\sum_{m''\neq m}\left(S^\alpha_{\mathbf{R}lm'',\mathbf{R}L}\right)^*\langle lm''\sigma|\,\hat{L}\cdot\hat{S}\,|l'm'\sigma'\rangle\;.
\end{aligned} \tag{5.1.22}$$

In the above, matrix elements of $\hat{L}\cdot\hat{S}$ ensure that from the sum over angular momenta L'' in the SSW, only the integral with the L channel is nonzero. Indeed, as we show in a subsequent section, the matrix elements of $\hat{L}\cdot\hat{S}$ are only nonzero for $l = l'$. When we take the matrix element between

SSWs, we cannot do this: we must include every L'' in the sum.

$$\begin{aligned}
&\langle\psi_{L\sigma}|\,\hat{H}_{\mathrm{soc}}\,|\psi_{L'\sigma'}\rangle\\
&=\iiint r^2\sin\theta dr d\theta d\phi\left[\left(n_l t_l^{(1)}+j_l t_l^{(2)}\right)Y_{lm}-\sum_{L''}\left(n_{l''}t_{l''}^{(3)}+j_{l''}t_{l''}^{(4)}\right)S^{\alpha}_{\mathbf{R}L'',\mathbf{R}L}Y_{l''m''}\right]^{\dagger}\\
&\times\frac{1}{c^2r}\frac{dV^{\sigma\sigma'}}{dr}\hat{L}\cdot\hat{S}\left[\left(n_{l'}t_{l'\sigma'}^{(1)}+j_{l'}t_{l'\sigma'}^{(2)}\right)Y_{l'm'}-\sum_{L'''}\left(n_{l'''}t_{l'''\sigma'}^{(3)}+j_{l'''}t_{l'''\sigma'}^{(4)}\right)S^{\alpha}_{\mathbf{R}L''',\mathbf{R}L'}Y_{l'''m'''}\right]\\
&=\left\langle n_l t_{l\sigma}^{(1)}+j_l t_{l\sigma}^{(2)}-\left(n_l t_{l\sigma}^{(3)}+j_l t_{l\sigma}^{(4)}\right)S^{\alpha}_{\mathbf{R}L,\mathbf{R}L}\right|\frac{1}{c^2r}\frac{dV^{\sigma\sigma'}}{dr}\left|n_l t_{l\sigma'}^{(1)}+j_l t_{l\sigma'}^{(2)}-\left(n_l t_{l\sigma}^{(3)}+j_l t_{l\sigma}^{(4)}\right)S^{\alpha}_{\mathbf{R}L,\mathbf{R}L}\right\rangle\\
&\times\langle lm\sigma|\,\hat{L}\cdot\hat{S}\,|l'm'\sigma'\rangle\\
&-\left\langle n_l t_{l\sigma}^{(3)}+j_l t_{l\sigma}^{(4)}\right|\frac{1}{c^2r}\frac{dV^{\sigma\sigma'}}{dr}\left|n_l t_{l\sigma'}^{(1)}+j_l t_{l\sigma'}^{(2)}\right\rangle\sum_{m''\neq m'}\left(S^{\alpha}_{\mathbf{R}lm'',\mathbf{R}L}\right)^*\langle lm''\sigma|\,\hat{L}\cdot\hat{S}\,|l'm'\sigma'\rangle\\
&-\left\langle n_l t_{l\sigma}^{(1)}+j_l t_{l\sigma}^{(2)}\right|\frac{1}{c^2r}\frac{dV^{\sigma\sigma'}}{dr}\left|n_l t_{l\sigma'}^{(3)}+j_l t_{l\sigma'}^{(4)}\right\rangle\sum_{m'''\neq m}S^{\alpha}_{\mathbf{R}lm''',\mathbf{R}L'}\langle lm\sigma|\,\hat{L}\cdot\hat{S}\,|l'm'''\sigma'\rangle\\
&+\sum_{L''\neq L}\sum_{L'''\neq L}\delta_{l'',l'''}\left(S^{\alpha}_{\mathbf{R}L'',\mathbf{R}L}\right)^*\left\langle n_{l''}t_{l''\sigma}^{(3)}+j_{l''}t_{l''\sigma}^{(4)}\right|\frac{1}{c^2r}\frac{dV^{\sigma\sigma'}}{dr}\left|n_{l'''}t_{l'''\sigma'}^{(3)}+j_{l'''}t_{l'''\sigma'}^{(4)}\right\rangle S^{\alpha}_{\mathbf{R}L''',\mathbf{R}L'}\\
&\times\langle l''m''\sigma|\,\hat{L}\cdot\hat{S}\,|l'''m'''\sigma'\rangle
\end{aligned}\tag{5.1.23}$$

The actual matrix element then becomes

$$\begin{aligned}
&\langle\Phi_L|\,\hat{H}_{\mathrm{soc}}\,|\Phi_{L'}\rangle\\
&=\left\langle\phi_{l\sigma}-\varphi_{l\sigma}+n_l t_{l\sigma}^{(1)}+j_l t_{l\sigma}^{(2)}-\left(n_l t_{l\sigma}^{(3)}+j_l t_{l\sigma}^{(4)}\right)S^{\alpha}_{\mathbf{R}L,\mathbf{R}L}\right|\frac{1}{c^2r}\frac{dV^{\sigma\sigma'}}{dr}\\
&\times\left|\phi_{l\sigma'}-\varphi_{l\sigma'}+n_l t_{l\sigma'}^{(1)}+j_l t_{l\sigma'}^{(2)}-\left(n_l t_{l\sigma'}^{(3)}+j_l t_{l\sigma'}^{(4)}\right)S^{\alpha}_{\mathbf{R}L,\mathbf{R}L}\right\rangle\langle lm\sigma|\,\hat{L}\cdot\hat{S}\,|l'm'\sigma'\rangle\\
&-\left\langle n_l t_{l\sigma}^{(3)}+j_l t_{l\sigma}^{(4)}\right|\frac{1}{c^2r}\frac{dV^{\sigma\sigma'}}{dr}\left|\phi_{l\sigma'}-\varphi_{l\sigma'}+n_l t_{l\sigma'}^{(1)}+j_l t_{l\sigma'}^{(2)}\right\rangle\sum_{m''\neq m'}\left(S^{\alpha}_{\mathbf{R}lm'',\mathbf{R}L}\right)^*\langle lm''\sigma|\,\hat{L}\cdot\hat{S}\,|l'm'\sigma'\rangle\\
&-\left\langle\phi_{l\sigma}-\varphi_{l\sigma}+n_l t_{l\sigma}^{(1)}+j_l t_{l\sigma}^{(2)}\right|\frac{1}{c^2r}\frac{dV^{\sigma\sigma'}}{dr}\left|n_l t_{l\sigma'}^{(3)}+j_l t_{l\sigma'}^{(4)}\right\rangle\sum_{m'''\neq m}S^{\alpha}_{\mathbf{R}lm''',\mathbf{R}L'}\langle lm\sigma|\,\hat{L}\cdot\hat{S}\,|l'm'''\sigma'\rangle\\
&+\sum_{L''\neq L}\sum_{L'''\neq L}\delta_{l'',l'''}\left(S^{\alpha}_{\mathbf{R}L'',\mathbf{R}L}\right)^*\left\langle n_{l''}t_{l''\sigma}^{(3)}+j_{l''}t_{l''\sigma}^{(4)}\right|\frac{1}{c^2r}\frac{dV^{\sigma\sigma'}}{dr}\left|n_{l'''}t_{l'''\sigma'}^{(3)}+j_{l'''}t_{l'''\sigma'}^{(4)}\right\rangle S^{\alpha}_{\mathbf{R}L''',\mathbf{R}L'}\\
&\times\langle l''m''\sigma|\,\hat{L}\cdot\hat{S}\,|l'''m'''\sigma'\rangle
\end{aligned}\tag{5.1.24}$$

Three types of integrals can be identified. The first are pure angular momentum integrals, which only take into account the interaction between functions of pure lm and $l'm'$ character respectively. In the second generation LMTO method, there are only these kinds of integrals. The second type mixes the m states as a result of the non-pure l character of the SSW. In effect, the SSW perturbs the pure angular momentum character of the partial waves, as well as those terms within the SSW which have lm character. The third type are integrals between the SSW and itself, resulting in a double sum over *all* l'' channels, since the SSW itself is a sum over spherical waves of l'' character. The properties of the $\hat{L}\cdot\hat{S}$ matrix elements limit the double sum to only the diagonal. Still, a simple expression like $\mathbf{M}\otimes\xi$ which could be constructed for the second generation LMTO method is not possible here. For comparison, the matrix element in the 2nd generation was

$$\langle \phi_{l\sigma} Y_{lm} | \hat{H}_{\mathrm{soc}} | \phi_{l'\sigma'} Y_{l'm'} \rangle = \langle \phi_{l\sigma} | \frac{1}{c^2 r} \frac{dV^{\sigma\sigma'}}{dr} | \phi_{l'\sigma'} \rangle \langle lm\sigma | \hat{L}\cdot\hat{S} | l'm'\sigma' \rangle \ , \tag{5.1.25}$$

which is much more simple. An alternative formulation to (5.1.24) is

$$\begin{aligned}
&\langle \Phi_L | \hat{H}_{\mathrm{soc}} | \Phi_{L'} \rangle \\
&= \left\langle \phi_{l\sigma} - \varphi_{l\sigma} + n_l t^{(1)}_{l\sigma} + j_l t^{(2)}_{l\sigma} \right| \frac{1}{c^2 r} \frac{dV^{\sigma\sigma'}}{dr} \left| \phi_{l\sigma'} - \varphi_{l\sigma'} + n_l t^{(1)}_{l\sigma'} + j_l t^{(2)}_{l\sigma'} \right\rangle \langle lm\sigma | \hat{L}\cdot\hat{S} | l'm'\sigma' \rangle \\
&- \left\langle n_l t^{(3)}_{l\sigma} + j_l t^{(4)}_{l\sigma} \right| \frac{1}{c^2 r} \frac{dV^{\sigma\sigma'}}{dr} \left| \phi_{l\sigma'} - \varphi_{l\sigma'} + n_l t^{(1)}_{l\sigma'} + j_l t^{(2)}_{l\sigma'} \right\rangle \sum_{m''=-l}^{l} \left(S^{\alpha}_{\mathbf{R}lm'',\mathbf{R}L} \right)^* \langle lm''\sigma | \hat{L}\cdot\hat{S} | l'm'\sigma' \rangle \\
&- \left\langle \phi_{l\sigma} - \varphi_{l\sigma} + n_l t^{(1)}_{l\sigma} + j_l t^{(2)}_{l\sigma} \right| \frac{1}{c^2 r} \frac{dV^{\sigma\sigma'}}{dr} \left| n_l t^{(3)}_{l\sigma'} + j_l t^{(4)}_{l\sigma'} \right\rangle \sum_{m'''=-l'}^{l'} S^{\alpha}_{\mathbf{R}lm''',\mathbf{R}L'} \langle lm\sigma | \hat{L}\cdot\hat{S} | l'm'''\sigma' \rangle \\
&+ \sum_{l''} \left\langle n_{l''} t^{(3)}_{l''\sigma} + j_{l''} t^{(4)}_{l''\sigma} \right| \frac{1}{c^2 r} \frac{dV^{\sigma\sigma'}}{dr} \left| n_{l''} t^{(3)}_{l''\sigma'} + j_{l''} t^{(4)}_{l''\sigma'} \right\rangle \sum_{m''=-l''}^{l''} \sum_{m'''=-l''}^{l''} \left(S^{\alpha}_{\mathbf{R}L'',\mathbf{R}L} \right)^* S^{\alpha}_{\mathbf{R}L'',\mathbf{R}L'} \\
&\times \langle l''m''\sigma | \hat{L}\cdot\hat{S} | l''m'''\sigma' \rangle \ ,
\end{aligned} \tag{5.1.26}$$

where we have moved the terms containing S^{α} from the first integral to all the other ones, which allows us to express the matrix element in terms of a vector-vector or vector-matrix-vector multiplication. This allows for a shorthand notation

$$\begin{aligned}
&\langle \Phi_{lm\sigma} | \hat{H}_{\mathrm{soc}} | \Phi_{l'm'\sigma'} \rangle \\
&= M_{lm\sigma,l'm'\sigma'} \xi^{(0)}_{l\sigma\sigma'} - \left[\sum_{m''=-l}^{l} \left(S^{\alpha}_{lm'',lm} \right)^* M_{lm''\sigma,l'm'\sigma'} \right] \left(\xi^{(1)}_{l\sigma\sigma'} \right)^* \\
&- \left[\sum_{m'''=-l'}^{l'} M_{lm\sigma,l'm'''\sigma'} S^{\alpha}_{lm''',l'm'} \right] \xi^{(1)}_{l\sigma\sigma'} \\
&+ \sum_{l''} \left[\sum_{m''=-l}^{l''} \sum_{m'''=-l''}^{l''} \left(S^{\alpha}_{lm'',lm} \right)^* M_{l''m''\sigma,l'''m'''\sigma'} S^{\alpha}_{l''m''',l'm'} \right] \xi^{(2)}_{l''\sigma\sigma'} \\
&= M_{lm\sigma,l'm'\sigma'} \xi^{(0)}_{l\sigma\sigma'} - \left(M^{\alpha}_{lm\sigma,l'm'\sigma'} \xi^{(1)}_{l\sigma\sigma'} \right)^* - M^{\alpha}_{lm\sigma,l'm'\sigma'} \xi^{(1)}_{l\sigma\sigma'} + \sum_{l''} [M^{\alpha}_{\alpha}]^{(l'')}_{lm\sigma,l'm'\sigma'} \, \xi^{(2)}_{l''\sigma\sigma'}
\end{aligned} \tag{5.1.27}$$

where

$$\begin{aligned}
M_{lm\sigma,l'm'\sigma'} &= \langle lm\sigma|\, \hat{L}\cdot\hat{S}\, |l'm'\sigma'\rangle \\
M^{\alpha}_{lm\sigma,l'm'\sigma'} &= \sum_{m''=-l}^{l} M_{lm\sigma,l'm''\sigma'} S^{\alpha}_{lm'',l'm'} \\
[M^{\alpha}_{\alpha}]^{(l'')}_{lm\sigma,l'm'\sigma'} &= \sum_{m''=-l}^{l''}\sum_{m'''=-l''}^{l''} \left(S^{\alpha}_{lm'',lm}\right)^{*} M_{l''m''\sigma,l''m'''\sigma'} S^{\alpha}_{l''m''',l'm'} \\
\xi^{(0)}_{l\sigma\sigma'} &= \left\langle \phi_{l\sigma} - \varphi_{l\sigma} + n_l t^{(1)}_{l\sigma} + j_l t^{(2)}_{l\sigma}\right| \frac{1}{c^2 r}\frac{dV^{\sigma\sigma'}}{dr} \left|\phi_{l\sigma'} - \varphi_{l\sigma'} + n_l t^{(1)}_{l\sigma'} + j_l t^{(2)}_{l\sigma'}\right\rangle \\
\xi^{(1)}_{l\sigma\sigma'} &= \left\langle \phi_{l\sigma} - \varphi_{l\sigma} + n_l t^{(1)}_{l\sigma} + j_l t^{(2)}_{l\sigma}\right| \frac{1}{c^2 r}\frac{dV^{\sigma\sigma'}}{dr} \left|n_l t^{(3)}_{l\sigma'} + j_l t^{(4)}_{l\sigma'}\right\rangle \\
\xi^{(2)}_{l\sigma\sigma'} &= \left\langle n_l t^{(3)}_{l\sigma} + j_l t^{(4)}_{l\sigma}\right| \frac{1}{c^2 r}\frac{dV^{\sigma\sigma'}}{dr} \left|n_l t^{(3)}_{l\sigma'} + j_l t^{(4)}_{l\sigma'}\right\rangle .
\end{aligned} \tag{5.1.28}$$

Now we can write down the SOC matrix between KPWs associated with $\mathbf{R}$.

$$\langle\Phi|\,\hat{H}_{\text{soc}}\,|\Phi\rangle = \mathbf{M}\otimes\xi^{(0)} - \left(\mathbf{M}^{\alpha}\otimes\xi^{(1)}\right)^{\dagger} - \mathbf{M}^{\alpha}\otimes\xi^{(1)} + \sum_{l}[\mathbf{M}^{\alpha}_{\alpha}]^{(l)}\otimes\xi^{(2)}_{l} \tag{5.1.29}$$

This is the matrix element between the KPWs labeled by $\mathbf{R}L\sigma$ and one labeled $\mathbf{R}L'\sigma'$. In practice, only the first term will contribute significantly, since the integrand for ξ parameters contains $1/rdV/dr$, which goes as $\propto \frac{1}{r^3}$. The contribution near the atom ($r \to 0$) dominates, and only the $\xi^{(0)}$ term exists there. Despite this, all terms have been implemented to ensure that proper testing can be done. There might exist systems for which the $\xi^{(1)}$ and $\xi^{(2)}$ terms are non-negligible. In the results section, we test whether we can neglect $\xi^{(1)}$ and $\xi^{(2)}$.

5.2 Non-spherical correction on atomic potentials

Another perturbative effect that will increase the accuracy of the implemented EMTO-transport code are non-spherical corrections to the atomic potentials. In the implemented code, the atomic potentials are assumed to be perfectly spherically symmetric, while in reality, the non-spherically symmetric crystal structure will introduce non-spherical character to the atomic potentials. This is part of the reason the atomic sphere approximation used in conventional LMTO calculations breaks down for non-close packed structures.

We use the same trick as in the above, i.e. we project the general non-spherically symmetric potential $V(r, \theta, \phi)$ onto a sum of spherical harmonics.

$$V(r, \theta, \phi) = \sum_{lm} V_{lm}(r) Y_{lm}(\theta, \phi)\,, \tag{5.2.1}$$

where

$$V_{lm}(r) = \int d\theta d\phi\, V(r, \theta, \phi) Y_{lm}(\theta, \phi)\,. \tag{5.2.2}$$

This way, we can separate the radial and angular integrals in first-order perturbation term. Explicitly,

$$\langle\chi|\, V_{lm}(r) Y_{lm}(\theta, \phi)\, |\chi\rangle = \langle\phi(r)|\, V_{lm}(r)\, |\phi(r)\rangle \times \langle\psi(\theta, \phi)|\, Y_{lm}(\theta, \phi)\, |\psi(\theta, \phi)\rangle\ . \tag{5.2.3}$$

The angular function we call $\psi(\theta, \phi)$ here has a particular form. For the (back-extrapolated) partial wave, it equals one particular spherical harmonic. For the SSW, it equals some sum of spherical harmonics. Fortunately we are working in a linear space, so we can simply split our integral into a sum of integrals, and there is only type of integral to consider. It is

$$\int d\theta d\phi\, Y_{lm}(\theta, \phi) Y_{l'm'}(\theta, \phi) Y_{l''m''}(\theta, \phi) \tag{5.2.4}$$

i.e. the integral over θ, ϕ of the product of three spherical harmonics. The fact that we can contract the product of two spherical harmonics into a sum of spherical harmonics together with the orthogonality of spherical harmonics makes these expressions easy to evaluate. The radial part, as always, can be numerically integrated.

6. RESULTS

6.1 EMTO implementation

The computational scheme mentioned above for Exact Muffin-Tin Orbitals (EMTO) has been implemented into a version of the Twente transport code. It is written in FORTRAN90, which is a low-level programming language well suited for efficient calculations. The code consists of two programs, meant for different types of calculations, but they are based on the same subroutines. The first is the transport code, with which most calculations are done. The formalism section above describes the way this code operates. The second program is a band structure generator based on the same principles. Here, the input geometry is assumed to be periodic in z, such that a band structure plot as a function of k_z can be calculated. By varying the energy E and finding the k_z for which E is an eigenstate of $H(k_z)$ we directly calculate the band structure along some direction, depending on the input geometry. We can produce a full band structure along all high symmetry directions by rotating the input geometry appropriately and recalculating.

The implementation of the new EMTO scheme was completed and tested in the band structure code. Some bugs remain in the transport code, however, in particular in the calculation of the transmission and reflection coefficients. Figures 6.1 and 6.2 show the calculated band structures for *spd*(f) EMTO basis functions along the [111] and [001] directions, as well as the band structures calculated with the Vienna Ab-initio Simulation Package (VASP), which is the most widely used DFT software package. The bands agree reasonably well, where the *spdf* bands show noticably better agreement with the VASP bands. However, the difference is small enough that we can safely use only *spd* bands in actual transport calculations. This is a nontrivial assessment, as having to use the f states considerably slows down the calculation. Instead of just 9 basis functions in *spd*, we would be forced to use 16 basis functions instead, should the *spd* not suffice.

The atomic potentials used in these calculations were extracted from a first-principles calculation using WIEN2K, another DFT program. The potential is fitted through an algorithm designed by M. Zwierzycki and O.K. Andersen [17]. Within this procedure, one can freely choose the degree of overlap between the atomic spheres. It is reported that an overlap of 30% between neighbouring atomic spheres is the optimum, as this is the best tradeoff between an accurate potential (the potential becomes more accurate with higher overlap) and the second order error in the overlap (as the EMTOs only solve the muffin-tin problem up to *first* order in the overlap). The fitting procedure gives no indication what the radius of the smaller hard sphere should be. The radius for this sphere is thus found empirically. It is set to 0.7 times the radius of the overlapping sphere, since this has been found to give the best result for Pt. There is virtually no difference between the calculations using only the $\xi^{(0)}$ term in Eq. 5.1.29 and calculations which involve the higher-order $\xi^{(1,2)}$ terms.

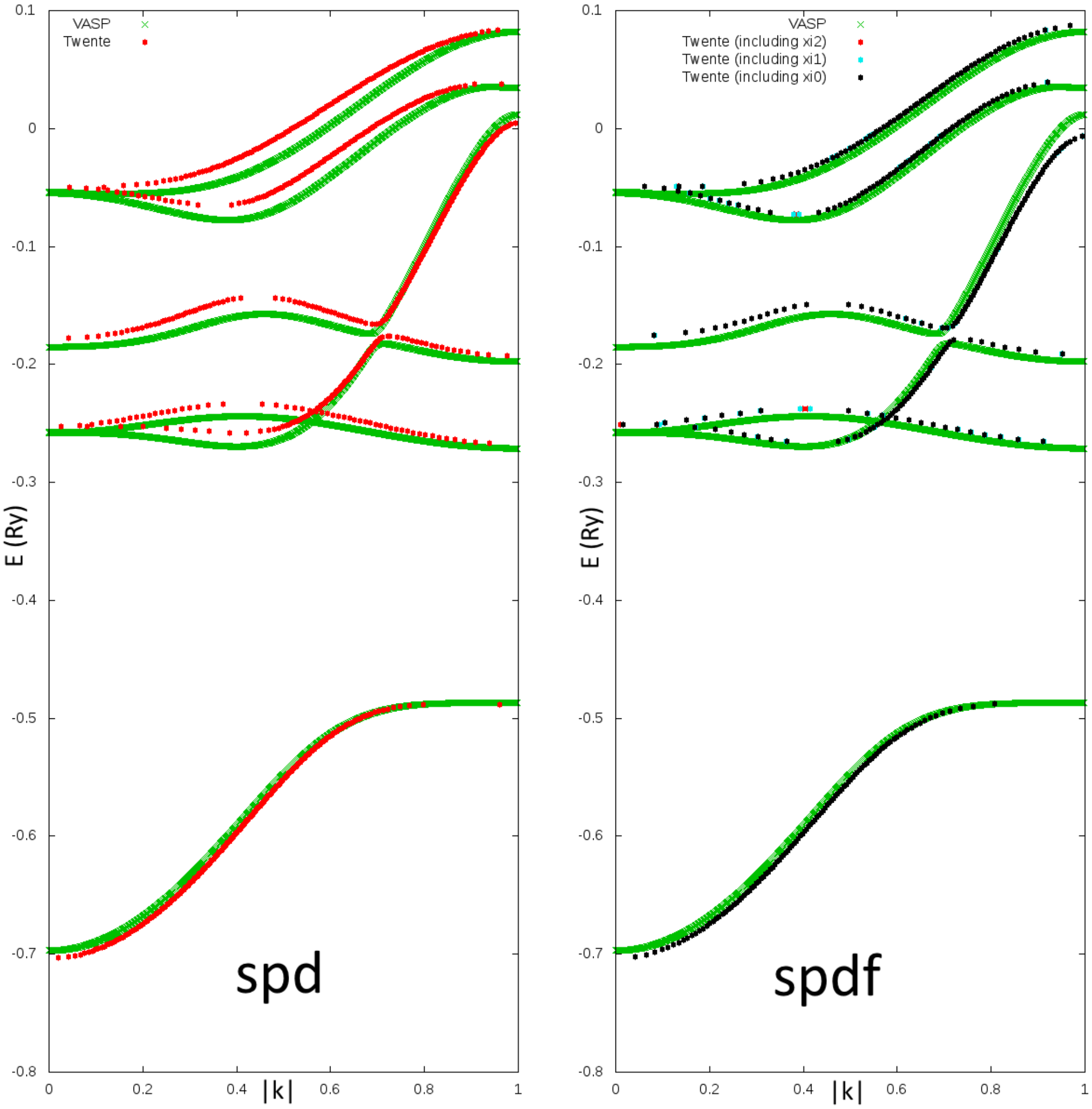

Fig. 6.1: Band structure of Pt along the [111] high symmetry direction. The basis functions on the left are *spd* and on the right are *spdf*. In green is the band structure produced by VASP and in red (black) the spd(f) EMTO band structure.

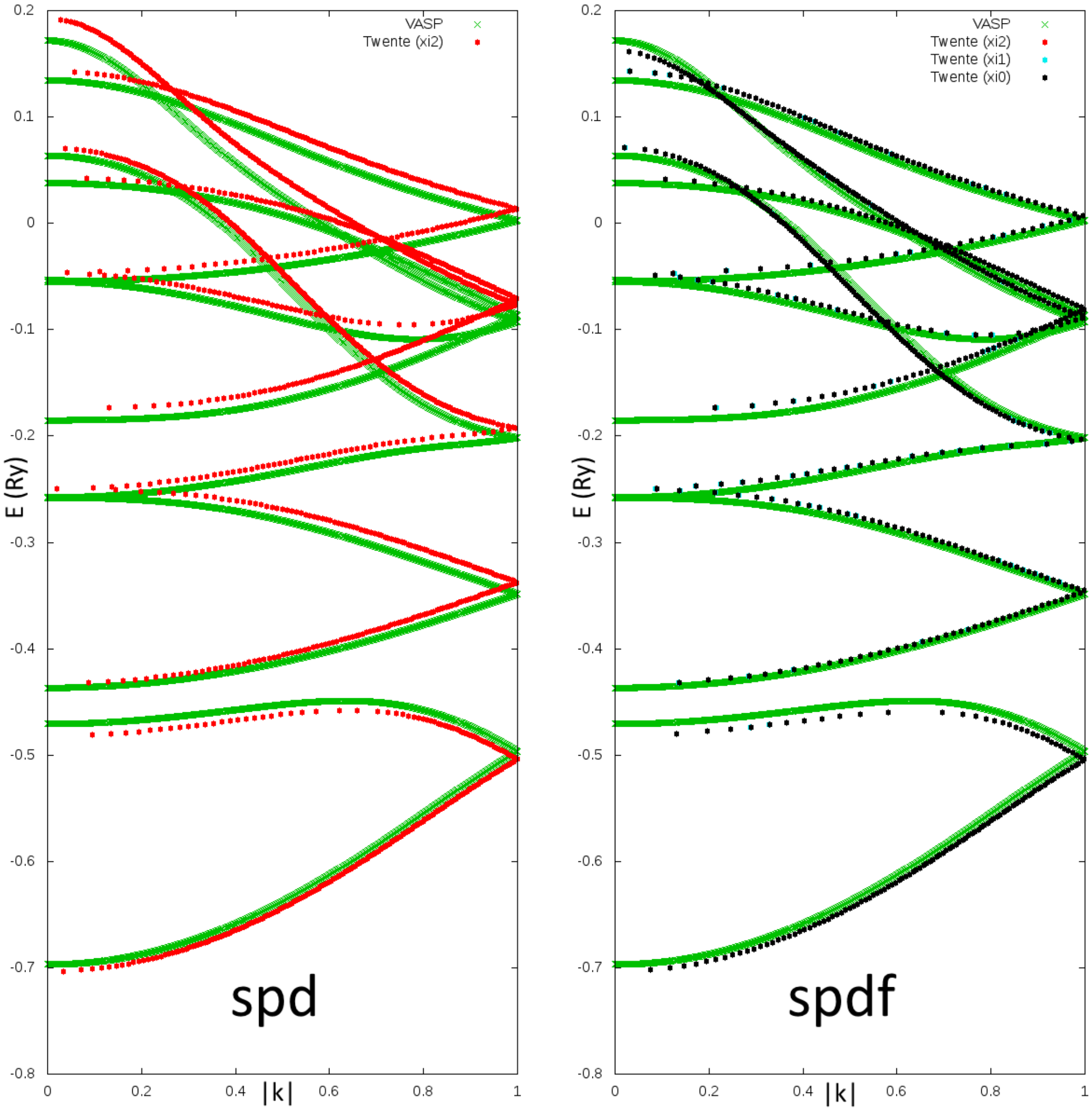

Fig. 6.2: Band structure of Pt along the [001] high symmetry direction. The basis functions on the left are *spd* and on the right are *spdf*. In green is the band structure produced by VASP and in red (black) the spd(f) EMTO band structure.

6.2 Comparison to analytical results

There is a very limited number of analytical results we can use to test our Galerkin implementation in the context of transport. We first consider the simplest possible example, transport through a rectangular barrier.

6.2.1 Transport through a rectangular potential barrier

We consider a one-dimensional space with coordinate z. Our geometry is completely empty except for some rectangular potential barrier, i.e. the potential $V(z)$ is equal to zero everywhere except for the region $0 < z < a$, for some $a \in \mathbb{R}$, where the potential is $V(z) = V_0$. The time-independent Schrödinger equation can be solved for all three regions of space separately. Before doing so, we expand our space to be three-dimensional, since our eventual numerical implementation within the LMTO/NMTO transport codes will also be three-dimensional. The Schrödinger equation for all space becomes

$$\begin{cases} -\dfrac{\hbar^2}{2m}\nabla^2\psi_L(x,y,z) = E\psi_L(x,y,z) & z < 0, \{x,y\} \in \mathbb{R}^2\,, \\ \left[-\dfrac{\hbar^2}{2m}\nabla^2 + V_0\right]\psi_S(x,y,z) = E\psi_S(x,y,z) & 0 < z < a, \{x,y\} \in \mathbb{R}^2\,, \\ -\dfrac{\hbar^2}{2m}\nabla^2\psi_R(x,y,z) = E\psi_R(x,y,z) & z > a, \{x,y\} \in \mathbb{R}^2\,, \end{cases} \tag{6.2.1}$$

where the ∇^2 operator is the Laplace operator

$$\nabla^2 = \left(\frac{\partial^2}{\partial x^2} + \frac{\partial^2}{\partial y^2} + \frac{\partial^2}{\partial z^2}\right)\,.$$

Solving these equations for all three regions of space is straightforward. The solutions are

$$\begin{cases} \psi_L(x,y,z) = \left[A^+ e^{ik_z z} + A^- e^{-ik_z z}\right] e^{i\mathbf{k}_\parallel\cdot\{x,y\}} & z < 0, \{x,y\} \in \mathbb{R}^2\,, \\ \psi_S(x,y,z) = \left[B^+ e^{ik_z^0 z} + B^- e^{-ik_z^0 z}\right] e^{i\mathbf{k}_\parallel\cdot\{x,y\}} & 0 < z < a, \{x,y\} \in \mathbb{R}^2\,, \\ \psi_R(x,y,z) = \left[C^+ e^{ik_z z} + C^- e^{-ik_z z}\right] e^{i\mathbf{k}_\parallel\cdot\{x,y\}} & z > a, \{x,y\} \in \mathbb{R}^2\,. \end{cases} \tag{6.2.2}$$

In the above, k_z and k_z^0 are uniquely determined by the values we pick for k_x and k_y, which together form the vector $\mathbf{k}_\parallel$.

$$\begin{aligned} k_z^2 &= \frac{2mE}{\hbar^2} - \mathbf{k}_\parallel^2 \\ \left(k_z^0\right)^2 &= \frac{2m\left(E - V_0\right)}{\hbar^2} - \mathbf{k}_\parallel^2 \end{aligned}$$

There is a slight ambiguity to this formulation, as we allow k_x and k_y to assume any value that satisfies $k_x^2 + k_y^2 \leq \frac{2mE}{\hbar^2}$, i.e. we allow for negative values. We force k_z to be positive, to highlight the fact that we have a left-going and a right-going (in z) state simultaneously.

The next step in the solution is to evaluate the boundary conditions. One of the postulates of quantum mechanics is the continuity of the wave function and its first derivative.

$$\begin{aligned} \psi_L(x,y,z=0) &= \psi_S(x,y,z=0) \\ \left.\frac{\partial \psi_L}{\partial z}\right|_{z=0} &= \left.\frac{\partial \psi_S}{\partial z}\right|_{z=0} \\ \psi_S(x,y,z=a) &= \psi_R(x,y,z=a) \\ \left.\frac{\partial \psi_S}{\partial z}\right|_{z=a} &= \left.\frac{\partial \psi_R}{\partial z}\right|_{z=a} . \end{aligned}$$

Using these equations, we can eliminate $B^{\pm}$ from the system of equations and find an expression for C^+ and A^- in terms of A^+ and $\mathbf{k}$, after setting $C^- = 0$ there is assumed to be no left-going wave on the right side of the barrier. A^+ is the amplitude of the inital incoming wave, which is arbitrary, so we set it to $A^+ = 1$. The amplitudes A^- and C^+ are precisely the reflection and transmission coefficients, since they are the amplitudes of the left-going wave left of the barrier and the right-going wave right of the barrier, respectively. The amplitude of these complex values are the transmission and reflection probabilities.

$$T(E,\mathbf{k}_{\|}) = \begin{cases} \dfrac{4k_z^2\left(k_z^0\right)^2}{4k_z^2\left(k_z^0\right)^2 + V_0^2\sinh^2(\left|k_z^0\right|a)} & \left(k_z^0\right)^2 < 0 \\ \dfrac{4k_z^2\left(k_z^0\right)^2}{4k_z^2\left(k_z^0\right)^2 + V_0^2\sin^2(k_z^0 a)} & \left(k_z^0\right)^2 \geq 0 \end{cases} \tag{6.2.3}$$

In order to illustrate the behaviour of a wave incident on the barrier, we set $\mathbf{k}_{\|} = 0$, which is the set of waves travelling perpendicular to the barrier. As can be seen in fig. 6.3, the transmission probability resembles the classical result, which is $T = 0$ for any energy $E < V_0 = 1$. In the quantum mechanical case, there is a small probability for waves with $E < V_0$ to propagate through the barrier. This is quantum tunneling. For higher energies, the transmission probability is equal to unity only for resonant energies with respect to the length of the barrier.
In the above, the first case describes the quantum tunneling regime. For small energies E, this part of the equation is important, but as E grows the number of allowed transmitted states grows, and the influence of the tunneling regime reduces.

Our implementation of the local discontinuous Galerkin method can unfortunately not be tested using the exact same wave functions. The reason for this is simple: whereas the analytical model assumes an infinite region of space to the left and right of the barrier to construct plane wave solutions, our implementation necessarily has a finite domain, so that we have to construct some other, more realistic wave function to study transmission through the barrier. We will use a Gaussian wave packet for this, given by

$$\psi(x) = e^{-(x-x_0)^2/4\sigma^2} e^{-ik_0 x} , \tag{6.2.4}$$

which is a plane wave solution with wave number k_0, but with a Gaussian distribution in real space centered at x_0 with a standard deviance of σ. Using this wave function as an initial condition allows us to study the transport through any potential barrier directly within the Galerkin method we

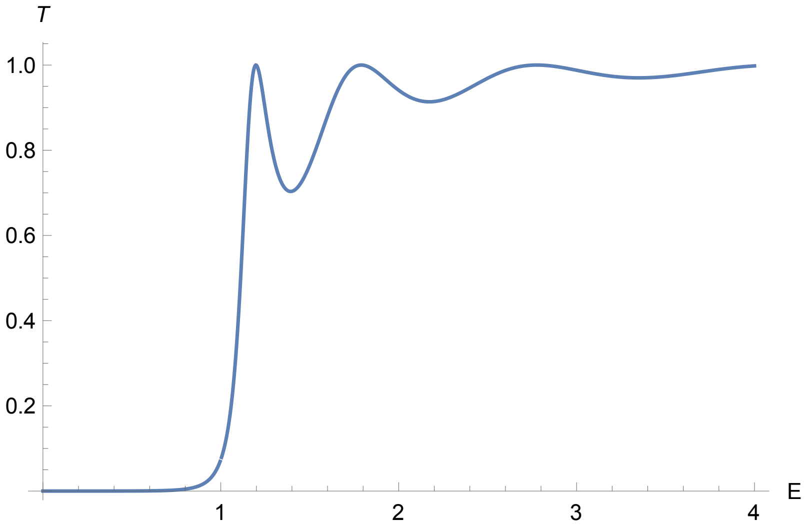

Fig. 6.3: Transmission probability as a function of energy for a wave incident on a rectangular potential barrier.

have implemented. We initialize the wave function with some velocity k_0, which also determines its energy through $E = \sqrt{2mE}/\hbar^2$ and calculate the norm of the wave function over the region beyond the barrier and divide it by the total norm of the wave function

$$t = \frac{\int_b^L |\psi(x)|^2 dx}{\int_0^L |\psi(x)|^2 dx} . \tag{6.2.5}$$

Here b is the rightmost point of the barrier. The transmission probability is then simply $T = t^2$. It must be noted that using this method to calculate transmission probabilities will necessarily give slightly different results. The Gaussian distribution in real space introduces components of all frequencies, not just k_0, into the wave function, as a result of the Heisenberg uncertainty principle. This means that any wave function we construct this way will have high frequency components which will be transmitted through the barrier. Similarly, the wave function will necessarily include low-frequency (and thus energy) components which have a very low probability of transmission. We see both of these effects in the actual results, which are shown in fig. 6.4. The transmission peaks belonging to the resonant energies are still present, although they no longer are equal to unity. In this calculation, the domain was $x = [0, 100]$, the number of elements was $N = 150$ and the polynomial order of approximation was $k = 1$. The height of the barrier is $V_0 = 1$.

6.2.2 Transport through a sawtooth potential barrier

One slightly more involved transport problem is the transport through a triangular barrier. The example is almost identical to the previous one, except now instead of a constant potential within

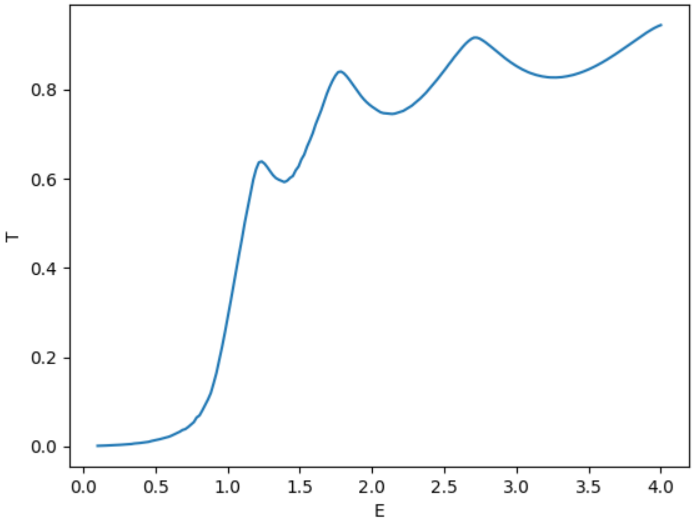

Fig. 6.4: Transmission probability as a function of average energy of a Gaussian wave packet incident on a rectangular potential barrier as calculated via the local discontinuous Galerkin method. The length of the domain is $L = 200$, the number of elements is $N = 300$ and polynomial order of approximation is $k = 1$.

the region $0 < z < a$, we have a potential which grows as z, i.e. $V(z) = V_0 z$.

$$\begin{cases} -\dfrac{\hbar^2}{2m}\nabla^2\psi_L(x,y,z) = E\psi_L(x,y,z) & z < 0, \{x,y\} \in \mathbb{R}^2 \\ \left[-\dfrac{\hbar^2}{2m}\nabla^2 + V_0 z\right]\psi_S(x,y,z) = E\psi_S(x,y,z) & 0 < z < a, \{x,y\} \in \mathbb{R}^2 \\ -\dfrac{\hbar^2}{2m}\nabla^2\psi_R(x,y,z) = E\psi_R(x,y,z) & z > a, \{x,y\} \in \mathbb{R}^2 \end{cases} \tag{6.2.6}$$

The first and third Schrödinger equations are identical, but the equation inside the barrier is more involved.

$$\left[-\frac{\hbar^2}{2m}\left(\frac{\partial^2}{\partial x^2} + \frac{\partial^2}{\partial y^2} + \frac{\partial^2}{\partial z^2}\right) + V_0 z\right]\psi(x,y,z) = E\psi(x,y,z) \tag{6.2.7}$$

We employ separation of variables, i.e. $\psi(x,y,z) = f(x)g(y)h(z)$. Then the x, y components of the equation are the same as before.

$$\begin{aligned} f(x) &= e^{ik_x x}\,, \\ g(y) &= e^{ik_y y}\,. \end{aligned}$$

Inserting this *ansatz*, we can isolate a differential equation for $h(z)$

$$\begin{aligned} \left(\frac{\partial^2}{\partial x^2} + \frac{\partial^2}{\partial y^2} + \frac{\partial^2}{\partial z^2}\right) f(x)g(y)h(z) &= -\frac{2m}{\hbar^2}\left(E - V_0 z\right) f(x)g(y)h(z)\,, \\ -\left(k_x^2 + k_y^2\right) f(x)g(y)h(z) + f(x)g(y)\frac{\partial^2}{\partial z^2}h(z) &= -\frac{2m}{\hbar^2}\left(Ef(x)g(y)h(z) - f(x)g(y)V_0 z h(z)\right)\,, \\ f(x)g(y)\left[-\big((k_x^2 + k_y^2\big)\,h(z) + \frac{\partial^2}{\partial z^2}h(z)\right] &= -\frac{2m}{\hbar^2} f(x)g(y)\left[Eh(z) - V_0 z h(z)\right]\,. \end{aligned}$$

We arrive at the differential equation

$$\frac{\partial^2}{\partial z^2}h(z) = \left[\frac{-2mE}{\hbar^2} + \left(k_x^2 + k_y^2\right) + \frac{2mV_0}{\hbar^2}z\right]h(z)\,, \tag{6.2.8}$$

which, for simplicity, we will abbreviate as

$$\frac{\partial^2}{\partial z^2}h(z) = \left[\alpha + \beta z\right]h(z)\,.$$

This equation is analytically solvable. Its solutions are linear combinations of Airy functions

$$h(z) = c_1\mathrm{Ai}\left(\frac{\alpha + \beta z}{\beta^{2/3}}\right) + c_2\mathrm{Bi}\left(\frac{\alpha + \beta z}{\beta^{2/3}}\right)\,, \tag{6.2.9}$$

where the Airy functions themselves are most elegantly defined in integral form

$$\mathrm{Ai}(x) = \frac{1}{\pi}\int_0^\infty \cos\left(\frac{t^3}{3} + xt\right)dt \tag{6.2.10}$$

$$\mathrm{Bi}(x) = \frac{1}{\pi}\int_0^\infty \left[\exp\left(-\frac{t^3}{3} + xt\right) + \sin\left(\frac{t^3}{3} + xt\right)\right]dt\,. \tag{6.2.11}$$

It is obvious that inserting the boundary conditions as we did in the previous example is not nearly as simple this time around. The boundary conditions are the same,

$$\begin{aligned}\psi_L(x,y,z=0) &= \psi_S(x,y,z=0)\\ \left.\frac{\partial\psi_L}{\partial z}\right|_{z=0} &= \left.\frac{\partial\psi_S}{\partial z}\right|_{z=0}\\ \psi_S(x,y,z=a) &= \psi_R(x,y,z=a)\\ \left.\frac{\partial\psi_S}{\partial z}\right|_{z=a} &= \left.\frac{\partial\psi_R}{\partial z}\right|_{z=a}\,,\end{aligned}$$

so the total wave function after setting $A^+ = 1$ and $C^- = 0$ becomes

$$\begin{cases}\psi_L(x,y,z) = \left[e^{ik_z z} + A^- e^{-ik_z z}\right] e^{i\mathbf{k}_\parallel\cdot\{x,y\}} & z<0, \{x,y\}\in\mathbb{R}^2\,,\\ \psi_S(x,y,z) = \left[c_1\mathrm{Ai}\left(\frac{\alpha+\beta z}{\beta^{2/3}}\right) + c_2\mathrm{Bi}\left(\frac{\alpha+\beta z}{\beta^{2/3}}\right)\right] e^{i\mathbf{k}_\parallel\cdot\{x,y\}}\,, & \\ \psi_R(x,y,z) = \left[C^+ e^{ik_z z}\right] e^{i\mathbf{k}_\parallel\cdot\{x,y\}} & z>a, \{x,y\}\in\mathbb{R}^2\,.\end{cases} \tag{6.2.12}$$

As a reminder, the parameter α and β are

$$\begin{aligned}\alpha &= \frac{-2mE}{\hbar^2} + \left(k_x^2 + k_y^2\right) = -k_z^2\,,\\ \beta &= \frac{2mV_0}{\hbar^2}\,.\end{aligned}$$

The boundary conditions become

$$\begin{aligned}1 + A^- &= c_1\mathrm{Ai}\left(\frac{\alpha}{\beta^{2/3}}\right) + c_2\mathrm{Bi}\left(\frac{\alpha}{\beta^{2/3}}\right)\,,\\ ik_z\left[1 - A^-\right] &= c_1\beta^{1/3}\mathrm{Ai}'\left(\frac{\alpha}{\beta^{2/3}}\right) + c_2\beta^{1/3}\mathrm{Bi}'\left(\frac{\alpha}{\beta^{2/3}}\right)\,,\\ c_1\mathrm{Ai}\left(\frac{\alpha+\beta a}{\beta^{2/3}}\right) + c_2\mathrm{Bi}\left(\frac{\alpha+\beta a}{\beta^{2/3}}\right) &= C^+ e^{ik_z a}\,,\\ c_1\beta^{1/3}\mathrm{Ai}'\left(\frac{\alpha+\beta a}{\beta^{2/3}}\right) + c_2\beta^{1/3}\mathrm{Bi}'\left(\frac{\alpha+\beta a}{\beta^{2/3}}\right) &= ik_z C^+ e^{ik_z a}\,.\end{aligned}$$

The Airy functions are quite convoluted, and even more so with the arguments we have given them, but we can simply consider them to be constants for now.

$$\begin{aligned}\alpha_1 &= \mathrm{Ai}\left(\frac{\alpha}{\beta^{2/3}}\right)\,, & \alpha_2 &= \mathrm{Ai}\left(\frac{\alpha+\beta a}{\beta^{2/3}}\right)\,,\\ \beta_1 &= \mathrm{Bi}\left(\frac{\alpha}{\beta^{2/3}}\right)\,, & \beta_2 &= \mathrm{Bi}\left(\frac{\alpha+\beta a}{\beta^{2/3}}\right)\,,\\ \alpha_1' &= \mathrm{Ai}'\left(\frac{\alpha}{\beta^{2/3}}\right)\,, & \alpha_2' &= \mathrm{Ai}'\left(\frac{\alpha+\beta a}{\beta^{2/3}}\right)\,,\\ \beta_1' &= \mathrm{Bi}'\left(\frac{\alpha}{\beta^{2/3}}\right)\,, & \beta_2' &= \mathrm{Bi}'\left(\frac{\alpha+\beta a}{\beta^{2/3}}\right)\,.\end{aligned}$$

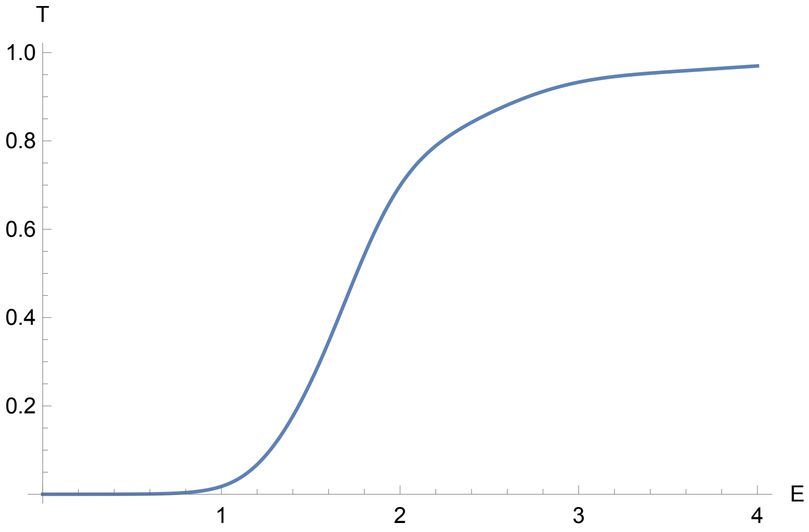

Fig. 6.5: Transmission probability as a function of energy for a wave incident on a sawtooth potential barrier.

The system of equations can be solved for A^- and C^+ separately, to yield the expressions for the reflection and transmission coefficients. To save on paper, we will use Mathematica for this. The full expression for the transmission amplitude is

$$C^+ = \frac{2\beta^{1/3}k_z e^{-iak_z}(\alpha_2'\beta_2 - \alpha_2\beta_2')}{i\beta^{2/3}(\alpha_1'\beta_2' - \alpha_2'\beta_1') - ik_z^2(\alpha_2\beta_1 - \alpha_1\beta_2) + \beta^{1/3}k_z(-\alpha_1\beta_2' + \alpha_1'\beta_2 - \alpha_2\beta_1' + \alpha_2'\beta_1)} . \qquad (6.2.13)$$

The transmission probability is

$$T(E, \mathbf{k}_\parallel) = \frac{4\beta^{2/3}k_z^2\left(\alpha_2'\beta_2 - \alpha_2\beta_2'\right)^2}{\left(\beta^{2/3}\left(\alpha_1'\beta_2' - \alpha_2'\beta_1'\right) + k_z^2\left(\alpha_2\beta_1 - \alpha_1\beta_2\right)\right)^2 + \beta^{2/3}k_z^2\left(-\alpha_1\beta_2' + \alpha_1'\beta_2 - \alpha_2\beta_1' + \alpha_2'\beta_1\right)^2} , \qquad (6.2.14)$$

where the dependence on E and $\mathbf{k}_\parallel$ comes from

$$k_z^2 = \frac{2mE}{\hbar^2} - \mathbf{k}_\parallel^2$$

together with

$$\begin{aligned}
\alpha_1 &= \mathrm{Ai}\left(-k_z^2\left(\frac{2mV_0}{\hbar^2}\right)^{-2/3}\right), & \alpha_2 &= \mathrm{Ai}\left(\left[-k_z^2+\frac{2mV_0}{\hbar^2}a\right]\left(\frac{2mV_0}{\hbar^2}\right)^{-2/3}\right), \\
\beta_1 &= \mathrm{Bi}\left(-k_z^2\left(\frac{2mV_0}{\hbar^2}\right)^{-2/3}\right), & \beta_2 &= \mathrm{Bi}\left(\left[-k_z^2+\frac{2mV_0}{\hbar^2}a\right]\left(\frac{2mV_0}{\hbar^2}\right)^{-2/3}\right), \\
\alpha_1' &= \mathrm{Ai}'\left(-k_z^2\left(\frac{2mV_0}{\hbar^2}\right)^{-2/3}\right), & \alpha_2' &= \mathrm{Ai}'\left(\left[-k_z^2+\frac{2mV_0}{\hbar^2}a\right]\left(\frac{2mV_0}{\hbar^2}\right)^{-2/3}\right), \\
\beta_1' &= \mathrm{Bi}'\left(-k_z^2\left(\frac{2mV_0}{\hbar^2}\right)^{-2/3}\right), & \beta_2' &= \mathrm{Bi}'\left(\left[-k_z^2+\frac{2mV_0}{\hbar^2}a\right]\left(\frac{2mV_0}{\hbar^2}\right)^{-2/3}\right).
\end{aligned}$$

As before, the conductance is

$$G(E) = \frac{2e^2}{h}\frac{1}{(2\pi)^2}\int d\mathbf{k}_\parallel T(E,\mathbf{k}_\parallel)/,. \tag{6.2.15}$$

Evaluating this expressions analytically would be a nightmare, assuming the expression is even integrable. Rather than go through this process, we will investigate the expression for the conductance numerically, where Mathematica will perform the numerical integration as well as the evaluation of the Airy functions. These are conveniently implemented. The transmission is shown in fig. 6.5.

We calculate the transmission probability as a function of energy with the local discontinuous Galerkin method using Gaussian wave packets to localise the wave function in space. The graph closely resembles the analytical one, as can be seen in fig. 6.6, but the same effects from the Gaussian wave packets as before can be seen. We have used the same parameters, i.e. $x = [0, 100]$, $N = 150$, $k = 1$, but with a sawtooth potential with $V_0 = 2$.

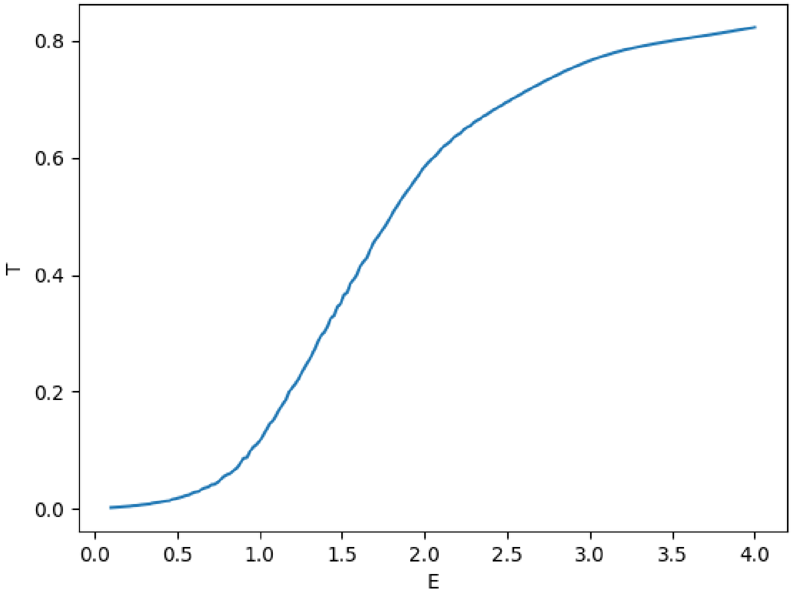

Fig. 6.6: Transmission probability as a function of average energy of a Gaussian wave packet incident on a sawtooth potential barrier as calculated via the local discontinuous Galerkin method. The length of the domain is $L = 200$, the number of elements is $N = 300$ and polynomial order of approximation is $k = 1$.

Tab. 6.1: Orders of convergence q^2 and q^∞, for respectively the L^2 and L^∞ errors, for the trivial solution to the 1D Schrödinger equation.

k	N	L^2 error	q^2	L^∞ error	q^∞
1	10	0.307063696	-	0.306426617	-
	20	0.044972351	2.77	0.042073604	2.86
	40	5.91E-03	2.93	0.005473214	2.94
	80	7.48E-04	2.98	0.000693084	2.98
2	10	1.76E-01	-	0.134734662	-
	20	0.023075097	2.93	0.017719628	2.93
	40	2.91E-03	2.99	0.002249528	2.98
	80	3.65E-04	3.00	0.000281837	3.00
3	10	4.48E-03	-	0.003143747	-
	20	1.44E-04	4.96	0.000101484	4.95
	40	4.53E-06	4.98	3.21E-06	4.98
	80	1.42E-07	5.00	1.00E-07	5.00
4	10	7.51E-04	-	0.000472179	-
	20	2.48E-05	4.92	1.56E-05	4.92
	40	7.85E-07	4.98	4.95E-07	4.98
	80	2.65E-08	4.89	1.66E-08	4.90

6.3 Numerical evaluation of the Galerkin method

The implementation of a finite element method such as Galerkin can be verified by direct comparison to analytical results. For instance, let us consider the 1D Schrödinger equation with $V(x) = 0$. If we set the boundary condition $\psi(0) = \psi(L) = 0$ for the domain $[0, L]$, we are precisely simulating the particle-in-a-box problem, for which the exact solutions are very well known indeed. They are

$$\begin{aligned} \psi_n(x,t) &= \sqrt{\frac{2}{L}} \sin\Big(\frac{n\pi x}{L}\Big) e^{-iE_n t/\hbar} \\ E_n &= \frac{\hbar^2}{2m}\Big(\frac{n\pi}{L}\Big)^2 . \end{aligned} \tag{6.3.1}$$

We can test our 1D implementation of the Schrödinger equation by running a calculation with

$$\psi(x,0) = \sqrt{\frac{2}{L}} \sin\Big(\frac{n\pi x}{L}\Big)$$

and computing the L^2 and L^∞ errors after some time. Moreover, by setting the polynomial order k of approximation and varying the number of cells N, we can calculate the order of convergence q for each. The numerical values can be found in table 6.1. The order of convergence shows interesting behaviour. It is equal to $k + 2$ for the odd k, but $k + 1$ for even values.

The exact solution to the 2D Schrödinger equation for a constant potential, with boundary conditions $\psi(\partial\Omega) = 0$, where $\partial\Omega$ is the boundary of the computation domain, are easily generated from the 1D solution, simply by considering a product of 1D solutions.

$$\psi_{n,m}(x,y,t) = \frac{2}{L} \sin\Big(\frac{n\pi x}{L}\Big) \sin\Big(\frac{m\pi x}{L}\Big) e^{-i(E_n+E_m)t/\hbar} \tag{6.3.2}$$

Tab. 6.2: Orders of convergence q^2 and q^∞, for respectively the L^2 and L^∞ errors, for the trivial solution to the 2D Schrödinger equation.

k	N	L^2 error	q^2	L^∞ error	q^∞
1	25	1.51E-01	-	8.09E-01	-
	100	1.51E-02	3.32	0.091734332	3.14
	225	4.19E-03	3.16	2.07E-02	3.67
	400	1.65E-03	3.23	8.15E-03	3.25
2	25	2.33E-02	-	8.56E-02	-
	100	3.05E-03	2.93	1.52E-02	2.49
	225	7.90E-04	3.37	3.63E-03	3.53
	400	2.96E-04	3.41	0.001326713	3.50
3	25	4.71E-03	-	0.016736933	-
	100	1.27E-04	5.22	0.000584286	4.84
	225	1.35E-05	5.52	5.45E-05	5.85
	400	2.98E-06	5.25	1.19E-05	5.30
4	25	4.08E-04	-	1.24E-03	-
	100	1.36E-05	4.90	5.37E-05	4.53
	225	1.56E-06	5.34	5.65E-06	5.56
	400	3.29E-07	5.42	1.17E-06	5.47

We have assumed a square domain $[0, L] \times [0, L]$. The 2D computation shows the same general behaviour. Although the orders of convergence are slightly above the $k + 2$ and $k + 1$ values that the 1D computation produced, the values are close, as can be seen in table 6.2.

The power of the Galerkin method in this specific case is the ability to admit different potentials $V(x)$ and calculate the time evolution of the quantum mechanical wave function with high accuracy. As an example, let us consider one of the simplest nonconstant potentials, the harmonic potential. We consider the one-dimensional case, with $\alpha > 0$.

$$V(x) = \alpha x^2 \,. \tag{6.3.3}$$

Analytical results for the Schrödinger equation with a harmonic potential exist, but for the purposes of this example, we will not derive them here. In general, they are the product of some polynomial and a Gaussian function, where the order of the polynomial determines the energy level. The (unnormalized) first excited state is

$$u_1(x) = xe^{-\beta x^2} \,, \tag{6.3.4}$$

and it is only an energy eigenstate when the condition $\beta = \sqrt{\alpha/4}$ holds. The energy then equals $E_1 = 6\beta$. An illustration of the wave function at some point in time is illustrated in fig. 6.7. The errors can be found in table 6.3. The very first computation with $k = 1$ and $N = 10$ is evidently unstable. The orders of convergence show roughly the same behaviour as in the trivial case, although the values themselves are more messy. Another interesting point is the calculated order of the very last calculation, which is much lower than expected (2 rather than 6). Apparently, this particular implementation has a minimum accuracy in the order of 10^{-9}, which might be related to the finiteness of the domain.

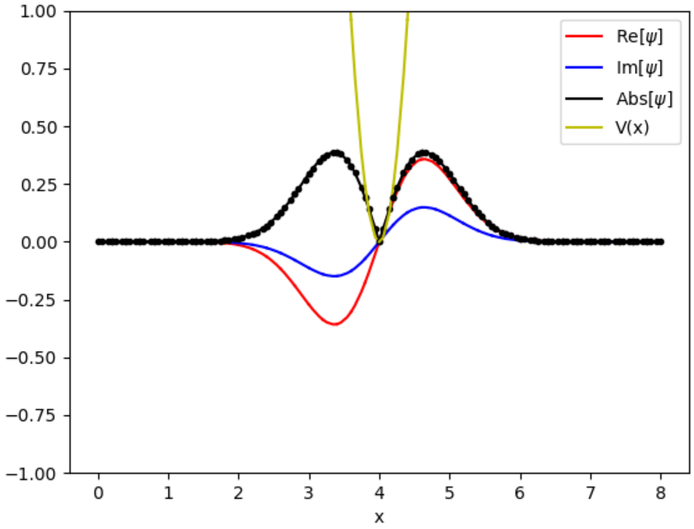

Fig. 6.7: Snapshot in time of the first excited state of the one-dimensional quantum harmonic oscillator, as calculated via the local discontinuous Galerkin method. Here the number of elements is $N = 40$ and the polynomial order of the approximation is $k = 2$.

The Gaussian element of the solution to the quantum harmonic oscillator results in a relatively localised, but in principle infinitely long range of the wave function. When we cut the domain short, the boundary conditions which force the wave function to be zero on the boundary inevitably affect the rest of the solution. If we cut the domain even shorter, this becomes more evident: after choosing the length of the domain to be $L = 3$ we calculate the L^2 and L^∞ errors to be around 0.003 for all orders k and number of cells N, without any particular improvement when we increase k or N.

The harmonic potential in two dimensions is simply a sum of one-dimensional potentials:

$$V(x, y) = \alpha_1 x^2 + \alpha_2 y^2 \, , \tag{6.3.5}$$

so that the solutions are products of one-dimensional solutions. For convenience, we set $\alpha_1 = \alpha_2 = \alpha$ and find

$$\psi_{1,1}(x, y) = xye^{-\beta(x^2+y^2)} \, . \tag{6.3.6}$$

The errors and orders of convergence are shown in table 6.4. The orders of convergence are the most erratic of all the reported values, but there is still a clear upward trend in the orders of k.

Tab. 6.3: Orders of convergence q^2 and q^∞ for the solution to the 1D Schrödinger equation with a harmonic potential, also known as the quantum harmonic oscillator, in the L^2 and L^∞ errors. Here, $\alpha = 5$ and the length of the domain is $L = 8$.

k	N	L^2 error	q^2	L^∞ error	q^∞
1	10	1.76E+20	-	1.28E+21	-
	20	0.001050831536	77.1	6.13E-03	77.5
	40	1.19E-04	3.14	0.0007851441977	2.97
	80	1.52E-05	2.97	9.96E-05	2.98
2	10	0.001880792732	-	0.01060144481	-
	20	1.24E-04	3.93	6.00E-04	4.14
	40	6.99E-06	4.15	4.51E-05	3.73
	80	3.41E-07	4.36	2.04E-06	4.47
3	10	5.50E-05	-	0.0002525452597	-
	20	1.01E-05	2.45	4.81E-05	2.39
	40	3.23E-07	4.97	2.14E-06	4.49
	80	6.34E-09	5.67	3.50E-08	5.94
4	10	6.32E-05	-	3.10E-04	-
	20	6.67E-07	6.57	3.59E-06	6.43
	40	9.48E-09	6.14	5.30E-08	6.08
	80	1.94E-09	2.29	1.29E-08	2.03

Tab. 6.4: Orders of convergence q^2 and q^∞ for the solution to the 2D Schrödinger equation with a harmonic potential, also known as the quantum harmonic oscillator, in the L^2 and L^∞ errors. Here, $\alpha = 5$ and the area of the domain is $L^2 = 8 \times 8$.

k	N	L^2 error	q^2	L^∞ error	q^∞
1	25	0.004448009064	-	0.06828330944	-
	100	0.0009785209507	2.18	0.0190117508	1.84
	225	0.000355693742	2.50	0.007101701792	2.43
	400	0.0001670237578	2.63	0.003035863874	2.95
2	25	0.003167640688	-	0.04285813287	-
	100	0.0003460341739	3.19	0.006169300041	2.80
	225	5.22E-05	4.66	0.001039597602	4.39
	400	1.62E-05	4.06	0.0003003996308	4.32
3	25	0.001103131019	-	0.01317221249	-
	100	1.57E-05	6.14	0.0002389669303	5.78
	225	6.42E-06	2.20	9.96E-05	2.16
	400	1.57E-06	4.89	2.84E-05	4.36
4	25	2.16E-04	-	0.002477268584	-
	100	8.34E-06	4.70	0.0001068040636	4.54
	225	6.77E-07	6.19	1.04E-05	5.74
	400	1.09E-07	6.36	1.54E-06	6.64

6.4 Structural defects in Pt

The LMTO transport code has in the past been used to calculated various material properties, such as the inverse spin Hall effect (ISHE) [12], the interface enhancement of Gilbert damping [6, 16] as well as spin flip diffusion lengths l_{sf} and spin Hall angles Θ_{sH} [13]. Although interfaces have been investigated as well, there is still a gap to bridge between the performed calculations and the experimental results. As outlined in [13], the experiments show a great spread in values, particularly for the SHA Θ_{sH}, which in part can be attributed to the relative lack of knowledge about the structural characteristics of the samples. Indeed, it is known that Pt crystallizes in an face-centered cubic (fcc) structure, but different depositing methods give different degrees of long-range order, such that stacking faults (SF), twins, vacancies and grain boundaries are almost certainly present in the samples, but the analysis of the experiments do not take this into account. In the present work, we will attempt to shed light on the effects of these structural defects on the properties related to spintronics, being l_{sf}, Θ_{sH} and any interface-like spin-memory loss δ or interface-like spin Hall effects Θ_I resulting from planar defects.

To start, there are some computational matters to consider. We need to generate atomic potentials for the Pt atoms, which we will do with the QUESTAAL suite, which is a DFT implementation using LMTOs which includes spin-orbit coupling (SOC) self-consistently, something the Stuttgart LMTO code used in previous works does not. The potential for the vacancies will be approximated to be an empty sphere, i.e. $V(r) = 0$. We will not perform structural relaxation of either the planar defects or the crystal around the vacancies. This would introduce a very expensive extra step in the calculation procedure, since we would need to put our geometry into an auxiliary DFT application. This auxiliary application would need to calculate the forces accurately, which means we would have to use a plane-wave based DFT code, which scale notoriously badly with the number of atoms and cannot reasonably handle the geometries we are dealing with, which consist of up to thousands of atoms. We assume the effect of the relaxation of the atoms around the defects to be small compared to the thermal disorder.

6.5 Vacancies

Different electronic properties have been studied as a function of the percentage of vacancies in the scattering region. Only small percentages have been considered, as they are the most physically reasonable. The resistivity of Pt with vacancies is expected to be linear in the number of vacancies, as predicted by perturbation theory. The results are shown in fig. 6.8. With the exception of the very small scattering region with length <5 nm, the calculated resistance follow the expected linear behaviour closely.

This behaviour is preserved when we introduce thermal disorder, as can be seen in fig. 6.9. In fact, the slope of the resistivity as a function of vacancy percentage stays the same, it is only the offset of the curve that changes, precisely by the value of $\rho_{\mathrm{T}=300K} = 10.8\ \mu\Omega$. The same holds for the SHA, which also scales linearly in the vacancy concentration with and with thermal disorder. The thermal disorder introduces an offset comparable to the SHA resulting from thermal disorder only, $\Theta_{\mathrm{sf}} \approx 4.2\%$.

In figure 6.10, the transverse spin currents for different vacancy percentages in crystalline Pt (mean-

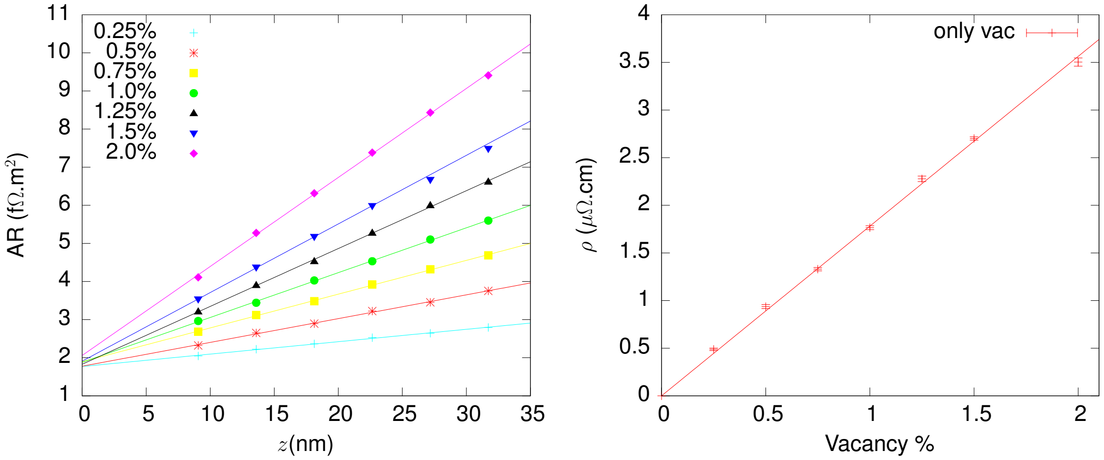

Fig. 6.8: On the left, the total resistance as a function of length of the scattering region for different vacancy percentages in Pt. The slope of the curve is the restivity, shown on the right as a function of vacancy percentage.

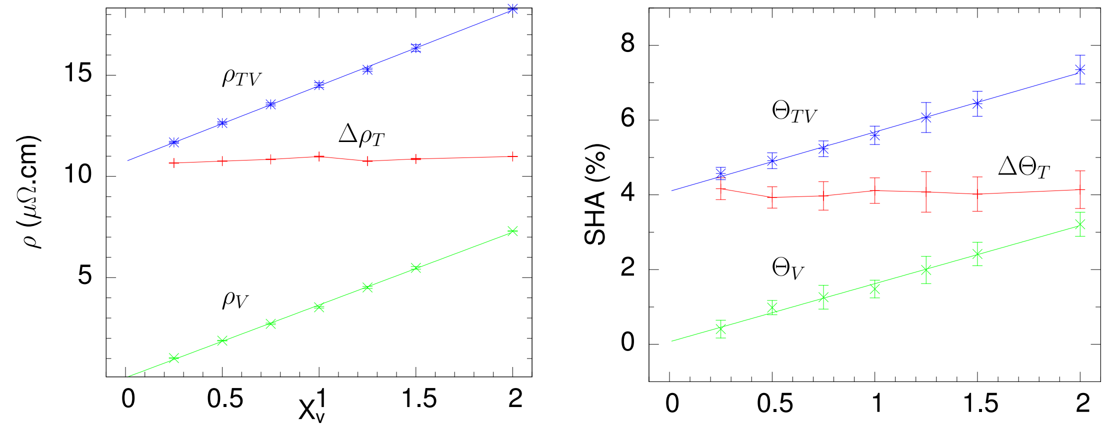

Fig. 6.9: Resistivity (left) and spin Hall angle (right) of Pt with and without thermal disorder (subscript T) as a function of vacancy percentage (subscript V).

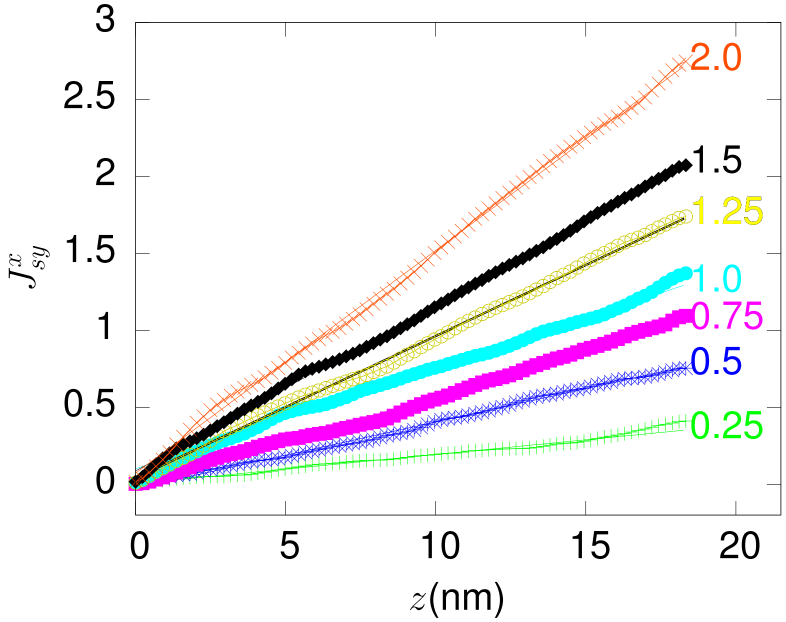

Fig. 6.10: Integrated transverse spin currents J^x_{sy} resulting from the spin Hall effect in Pt for different vacancy percentages. No thermal disorder was implemented in these calculations. Each line is the average of 10 different configurations of random placements of the vacancies within the scattering region.

ing no thermal disorder) are shown. The erraticity of the currents can be understood to be the result of the very localised effect of the vacancies. In fig. 6.11, we see that the spin currents in each layer where there are one or more vacancies present jumps significantly. In layers without vacancies, the spin currents quickly decay close to zero. This is precisely what one would expect. The impurities directly cause the spin Hall effect.

A similar calculation is performed to find l_{sf}, the spin flip diffusion length, as a function of the vacancy percentage. The results are shown in fig. 6.12. Four plots are shown; the blue and green lines are the value for l_{sf} as directly calculated by injecting a spin-polarized current and fitting the value of l_{sf} to the resulting exponential function. The pink and red plots are estimated values for $l_{\mathrm{sf}}^{\mathrm{T=300K}}$ and $l_{\mathrm{sf}}^{\mathrm{T=300\ K+vac\%}}$, calculated by the equation given by the assumption of parallel additivity of l_{sf}, i.e.

$$\frac{1}{l_{\mathrm{sf}}^{\mathrm{T=300K\ +\ vac\%}}} = \frac{1}{l_{\mathrm{sf}}^{\mathrm{T=300K}}} + \frac{1}{l_{\mathrm{sf}}^{\mathrm{vac\%}}} \,. \tag{6.5.1}$$

In other words, the pink line shows an estimation of $l_{\mathrm{sf}}^{\mathrm{T=300K}}$ extracted from the calculations of l_{sf} as a function of vacancy percentage with and without thermal disorder. Comparing this to the value of $l_{\mathrm{sf}}^{\mathrm{T=300K}}$ calculated directly, which is the value of the blue plot at zero vacancy percentage, we see that the estimated values agree reasonably well, within roughly ±0.25 nm. The red plot shows the converse calculation; an estimation of $l_{\mathrm{sf}}^{\mathrm{T=300\ K+vac\%}}$ based on the values directly calculated

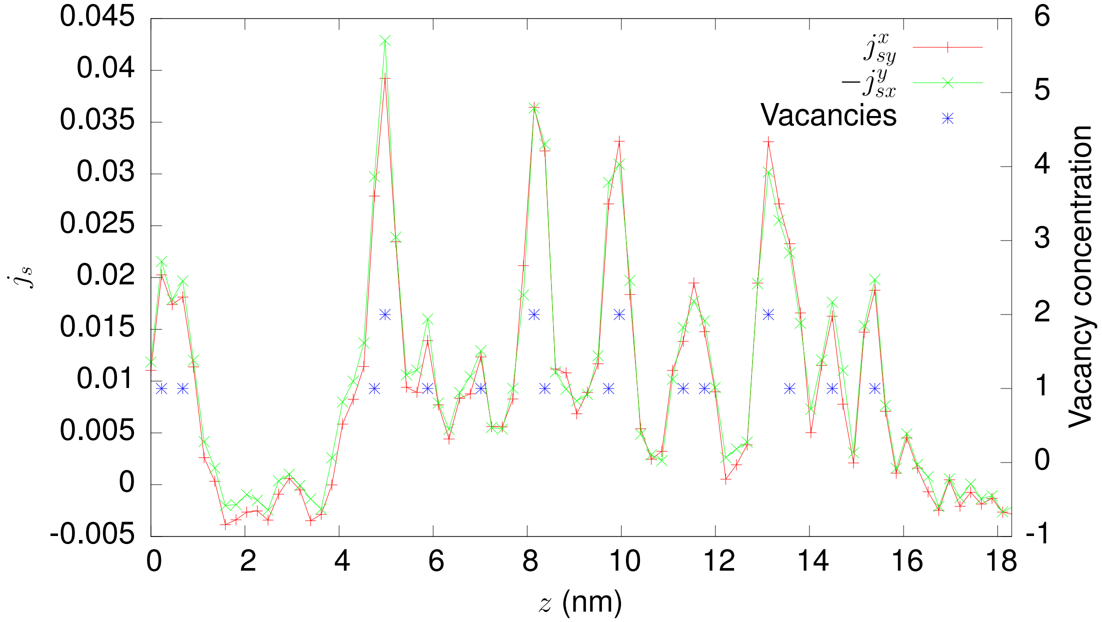

Fig. 6.11: Transverse spin currents j^x_{sy} and j^y_{sx} resulting from the spin Hall effect in Pt of one particular configuration, with the points symbolizing the location and number of vacancies within each layer.

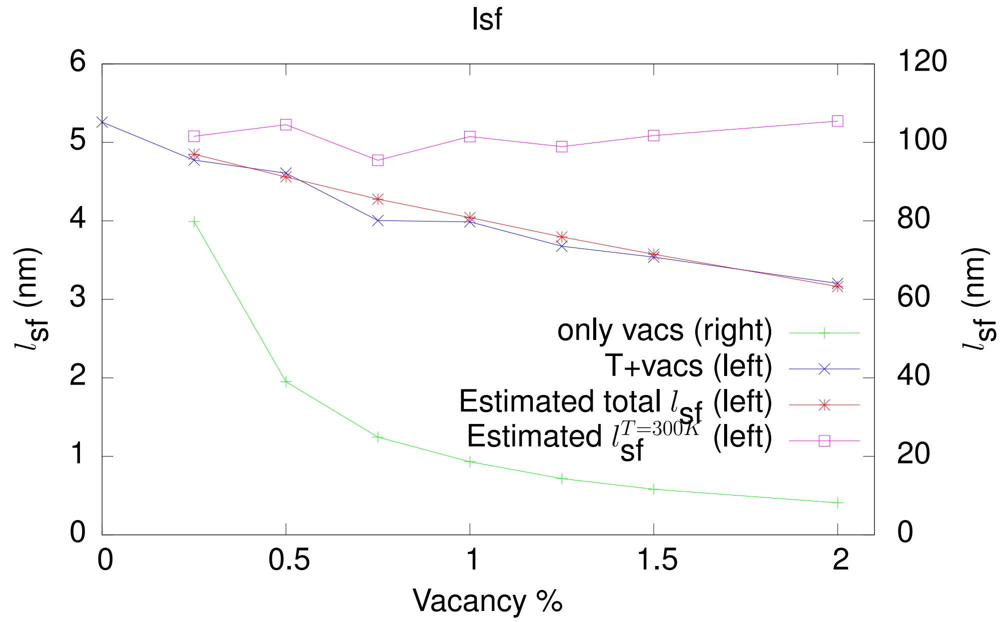

Fig. 6.12: Spin flip diffusion length ($l_{\rm sf}$) of Pt with and without thermal disorder as a function of vacancy percentage.

for $l_{\rm sf}^{\rm T=300K}$ and $l_{\rm sf}^{\rm vac\%}$. In short, the resistivity and spin flip diffusion length are additive in the temperature and vacancy percentage, but the SHA is not. As a result, the product $\rho l_{\rm sf}$ is roughly a constant within these calculations.

6.6 Planar defects

Two elementary planar defects were examined. They are the twin and the stacking fault (SF), which are the simplest planar defects that occur in the fcc crystal. In the (111) direction, the fcc crystal is made up of close-packed planes with three possible positions, called the A, B and C planes. The fcc structure is formed by ABCABC stacking. When the stacking order is reversed at some layer, this is called a twin. The stacking order becomes e.g. ABCACBA, when the twin layer is an A layer. It is presumably called a twin because the grains on either side of the twin are mirror images of each other. The SF is what happens when one layer is missing, e.g. ABCBCAB.

6.6.1 Current perpendicular to plane

Examining the transverse spin currents around the twin and SF, we see a peak resembling an interface spin Hall effect. This is shown in fig. 6.13. An interesting detail is the dip in the current at the precise layer of the twin, which is lower than the layers surrounding it. These calculations include thermal disorder, which can be seen in the value of the SHA away from the defect. The SF

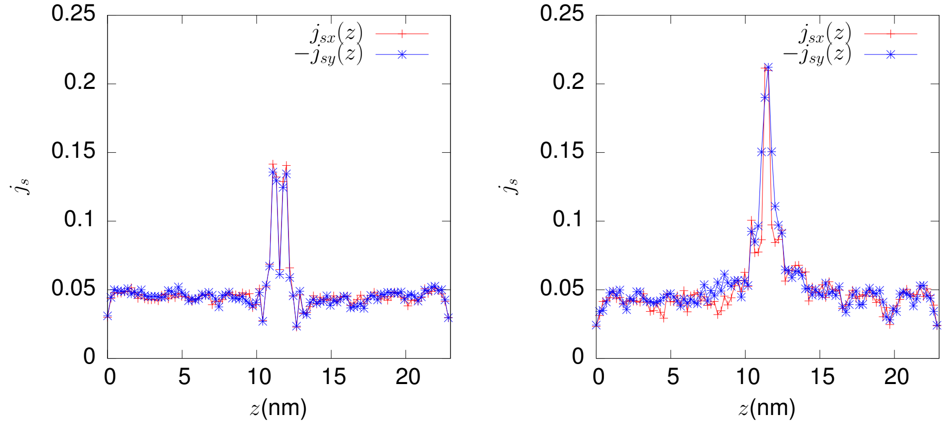

Fig. 6.13: On the left, the tranverse spin currents around a twin defect, and on the right those for the stacking fault.

has a much more greater impact on the SHA, both in amplitude and in spatial range.

The planar defects, being an interface-like contribution, do not contribute to the resistivity, but rather introduce an offset to the resistance curve, as a Sharvin contribution. The resistances of the twin and SF are calculated to be $AR_{\text{twin}} = 0.018 \pm 0.002$ fΩ·m^2 and $AR_{\text{SF}} = 0.056 \pm 0.004$ fΩ·m^2 respectively.

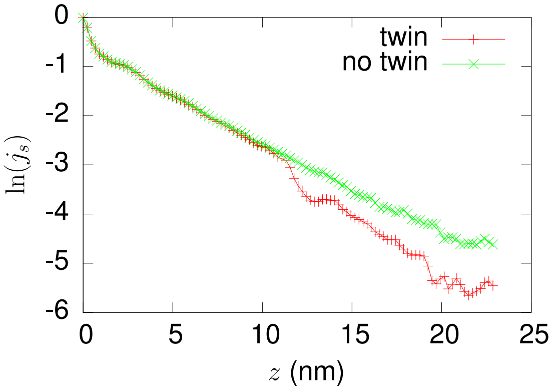

Fig. 6.14: The spin current as a function of position z within the scattering region, with and without a twin in the middle, averaged over 10 configurations of thermal disorder, where the atomic positions before the twin are identical in both cases.

The effect of the twin defect on the spin current when injecting a polarized current into Pt can be seen in figure 6.14. The effect of the twin can be clearly seen; it introduces an offset to the linear decay in the spin current. The positions of the Pt atoms within the scattering regions are identical, it is only after the twin layer that the geometries are different. The spin currents in the first approx. 5 nm of the scattering region are indistinguishable, but even at a distance of around 5 nm before the twin, the spin current in the scattering region with the twin is already lower than in the one without the twin. This is probably related to some reflective properties of the planar defect.

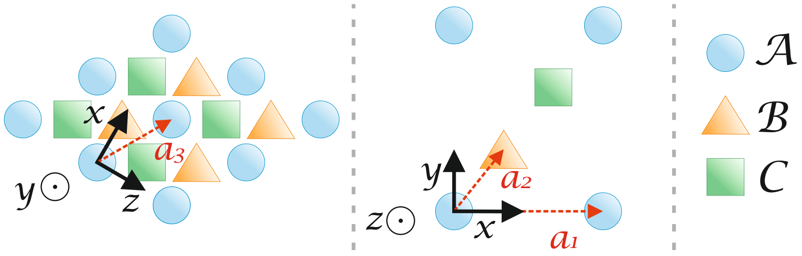

Fig. 6.15: The fcc lattice oriented such that the close-packed planes are stacked in the y direction parallel to an xz plane.

6.6.2 Current in plane

In the previous calculations, the close-packed planes of the fcc structure were always stacked in the z-direction. When one wishes to calculate the properties of a TB or SF parallel to the transport direction, the close-packed planes must be stacked so as to contain the z axis. If we want one SF per unit cell, this puts a restriction on the possible lateral supercell sizes in the direction of stacking through the periodic boundary conditions. For example, if five close-packed layers are stacked as ...|ABCBC|ABC..., there is exactly one SF within the scattering region. Using six layers, ...|ABCBCA|ABC... would result in two A layers on top of each other, which introduces an additional defect (and an energetically unlikely one). A schematic of the new geometry is shown in fig. 6.15. We only look at SFs and stack the close-packed planes in the y direction. The smallest possible supercell sizes are 5×10, 6×8 and 5×11, where we have chosen the supercell dimension in the x direction so that every supercell has approximately the same number of atoms within each xy plane. We insert one SF in the 6×8 and 5×11 supercells and two SFs in the 5×10 supercell.

The resistance calculated as a function of the length and the resulting in-plane resistivities are shown in 6.16. The inset shows the resistivity as a function of the SF concentration, i.e. the number of SFs per close-packed plane. For the supercells with SFs, the resistivity seems to grow linearly with the SF density, albeit with a higher predicted resistivity for Pt without SFs.

The same effect can be seen in Fig. 6.17, which shows the SHA for different supercell sizes. Although slightly obscured by the error bars, there is a slight difference between the two transverse directions. For the highest SF density, which in this case was a 5×10 supercell with two SFs, the gap is noticeably large.

The spin flip diffusion length is more severely affected. Fig. 6.18a shows the exponential decay of the polarized spin current and a clear distinction can be made. The supercells with a SF have

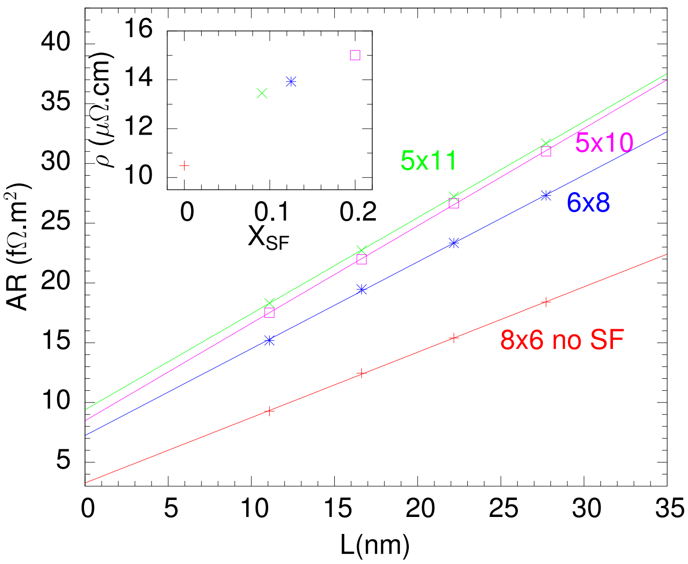

Fig. 6.16: The resistance and resistivities for different fcc Pt with different densities of stacking faults. The close-packed planes are stacked in the y direction, so that the lateral supercell size determines the SF density. The 5x11 and 6x8 supercells have one SF and the 5x10 supercell has two SFs.

significantly lower l_{sf}, between 1.4 and 2 nm. Higher SF density corresponds to a smaller l_{sf}. The product of ρ and l_{lsf} is shown in Fig. 6.18b. Evidently, l_{sf} decreases more rapidly than ρ increases as a function of X_{SF}, so that an Elliot-Yafet- like relationship does not hold.

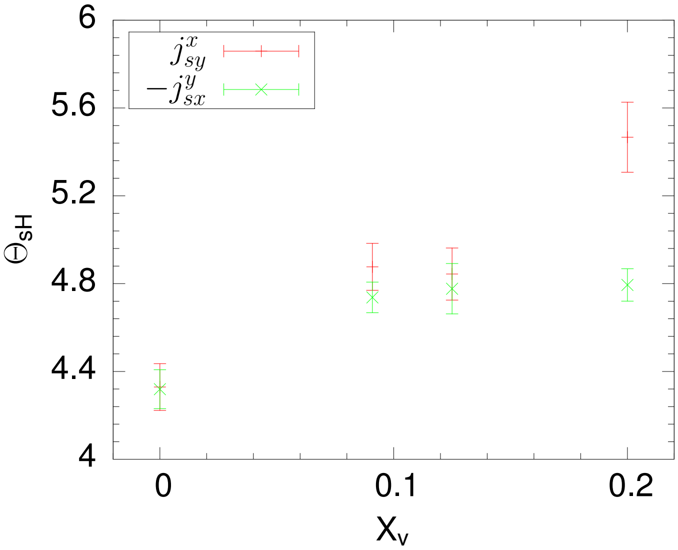

Fig. 6.17: Transverse spin currents for different SF densities, normalized on the charge current in the z direction. The same supercell sizes as in the previous figure were used.

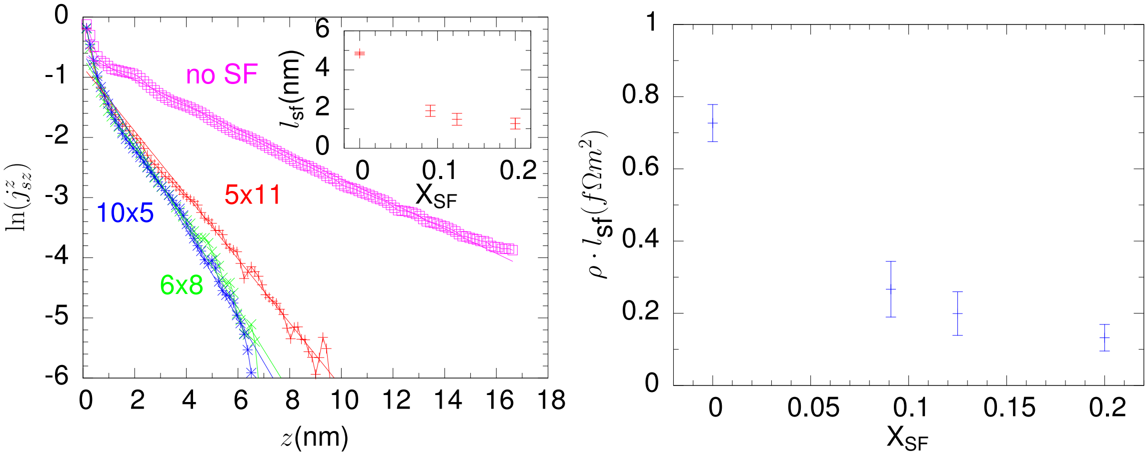

(a) Spin flip diffusion lengths l_{sf} for different concentrations of stacking faults (SFs).

(b) The product of ρ and l_{sf}, which according to the Elliot-Yafet mechanism should be a constant.

6.7 Conclusions and Recommendations

This report has in effect concerned itself with three main topics. Since the topics do not overlap in scope much, we will conclude them separately.

6.7.1 Vacancies and planar defects in Pt

Calculations were performed on the effects of structural defects on the spintronic properties of Pt, most notably the spin Hall angle (SHA) and the spin-flip diffusion length (ℓ_{sf}). When the spin current was perpendicular to the planar defect, the results agree with the Elliot-Yafet relationship, which is believed to be the dominant mechanism in spin relaxation in Pt. The calculations show that structural defects can make a significant contribution to the spin-flip scattering within a material. The results do not conclusively show that the spread in experimental data for the SHA and ℓ_{sf} are solely due to the structural defects studied in this work, and a satisfactory explanation for the discrepencancies is still lacking. We recommended that the work on structural defects is continued. One obvious continuation would be to consider more general grain boundaries, as the studied twin and stacking fault defects are not necessarily the most common.

The results for current in the plane of defects are less intuitive and may result in more insightful follow-up calculations. The fact that the Elliot-Yafet relationship is not fulfilled indicates that something interesting might be going on.

6.7.2 EMTO implementation

Spin orbit coupling was implemented into an existing version of the EMTO transport code. The correct expressions for the spin-orbit coupling Hamiltonian were found and implemented, although time restrictions meant that the transport code was not fully updated. Significant steps in the generation of a next-generation transport code were done, but there still remains much work to be done. The band structure code works well, and although the transport code is almost completely based on the same subroutines, this code is still dysfunctional. The ability of the EMTO formalism to treat a larger class of materials than the convential LMTO formalism will be a boon to any future spintronic calculations, as many interesting materials cannot be accurately described by the LMTO formalism.

The next step would be to first fix the bugs that plague the EMTO transport code that includes SOC. The next thing would be to incorporate the currents calculation into the code, which would bring the level of functionality of the EMTO code up to the LMTO code. Then, one could start to do interesting calculations. Another feature, which is discussed above, can also be implemented, which are the non-spherical corrections on the atomic potentials. With this implemented, a very wide class of materials could be studied.

6.7.3 Numerical solutions using the Galerkin method

The local discontinuous Galerkin method for the Schrödinger equation in one and two dimensions for arbitrary potentials was implemented in Python. The order of convergence as a function of the polynomial order of approximation within each finite element was computed and was found to be $k+2$ for odd values of k, and $k+1$ for even values. This means that the method is an accurate means of calculating solutions to the 1D and 2D Schrödinger equations for arbitrary potentials, although the relatively large number of basis elements means that the method cannot be easily scaled to include large numbers of atoms. Nevertheless, the insights gained from writing a numerical solver like this are helpful to any mathematician or physicist who is interested in computation of any sort. There are certainly more topics to explore within the code that was written, e.g. an thorough investigation into why the orders of convergence are different for odd and even polynomial orders.

The transport calculations using the Galerkin implementation could also be refined further. In particular, the effect of using Gaussian wave packets rather than plane waves could be studied in greater detail and might yield interesting results, as real-world particle resemble Gaussian wave packets much more closely than plane waves.

6.7.4 Final remarks

It is clear that all three topics can be continued and combined to produce more interesting research. For instance, the new EMTO scheme can be used to more accurately calculate properties of the structural defects and in the end, produce more complete results. It is our recommendation to focus on the planar defects first, before finishing the implementation of EMTO scheme. The results thus found are interesting, but do not answer any outstanding questions, so more calculations are needed. Especially since the planar defects are closely related to interfaces, one of the essential aspects of spintronics which is largely ignored by most experimental work.

The implementation of Galerkin-like mathematical techniques into the MTO schemes is not straightforward or obvious. In fact, the Galerkin method essentially does the same job as the MTO scheme: it transforms the Schrödinger equation from a mathematical equation to a tangible computational scheme. The interesting part lies in the philosophy behind both schemes. Where the MTO formalism explicitly approximates the atomic potentials to be spherically symmetric, the Galerkin method can be formulated to work for any potential $V(\mathbf{r})$. It is here that its strength, but also its weakness lies. The MTO method is extraordinarily efficient precisely because it approximates before deriving the scheme. It does so based on physical principles: the potential near an ion will almost certainly be spherically symmetric, as it follows Coulomb's law. It is not the Galerkin method itself that will be useful in the further development of the EMTO transport code, but rather the ideas that make the Galerkin or other methods rooted in mathematics so versatile and stable. The mathematical mindset certainly helps when deriving ways to improve the existing transport code.

Development of the EMTO transport code based on physical principles as well as mathematical constructs should be the work following this report. With a more sophisticated code, more interesting physical problems can be studied and hopefully solved, or at the very least, better understood.

BIBLIOGRAPHY

[1] O. Andersen, C. Arcangeli, R. Tank, Tanusri Saha-Dasgupta, Georges Krier, O. Jepsen, and I. Dasgupta. Third-generation TB-LMTO. *Materials Research Society Symposium - Proceedings*, 491, 05 1998.

[2] O. K. Andersen and O. Jepsen. Explicit, First-Principles Tight-Binding Theory. *Phys. Rev. Lett.*, 53:2571–2574, Dec 1984.

[3] Jan S. Hesthaven. *Nodal Discontinuous Galerkin Methods: Algorithms, Analysis, and Applications (Texts in Applied Mathematics Book 54)*. Springer, dec 2007.

[4] P. Hohenberg and W. Kohn. Inhomogeneous Electron Gas. *Phys. Rev.*, 136:B864–B871, Nov 1964.

[5] W. Kohn and L. J. Sham. Self-Consistent Equations Including Exchange and Correlation Effects. *Phys. Rev.*, 140:A1133–A1138, Nov 1965.

[6] Yi Liu, Zhe Yuan, R. J. H. Wesselink, Anton A. Starikov, and Paul J. Kelly. Interface Enhancement of Gilbert Damping from First Principles. *Phys. Rev. Lett.*, 113:207202, Nov 2014.

[7] Wenying Lu, Yunqing Huang, and Hailiang Liu. Mass preserving discontinuous Galerkin methods for Schrödinger equations. *Journal of Computational Physics*, 282, 02 2015.

[8] Mark H. Carpenter and David Gottlieb and Saul Abarbanel. The Stability of Numerical Boundary Treatments for Compact High-Order Finite-Difference Schemes. *Journal of Computational Physics*, 108(2):272 – 295, 1993.

[9] Anton A. Starikov, Yi Liu, Zhe Yuan, and Paul J. Kelly. Calculating the transport properties of magnetic materials from first principles including thermal and alloy disorder, noncollinearity, and spin-orbit coupling. *Phys. Rev. B*, 97:214415, Jun 2018.

[10] R.W. Tank and C. Arcangeli. An Introduction to the Third-Generation LMTO Method. *physica status solidi (b)*, 217(1):89–130, 2000.

[11] Qi Tao and Yinhua Xia. Error estimates and post-processing of local discontinuous Galerkin method for Schrdinger equations. *Journal of Computational and Applied Mathematics*, 356:198 – 218, 2019.

[12] Lei Wang, R. J. H. Wesselink, Yi Liu, Zhe Yuan, Ke Xia, and Paul J. Kelly. Giant Room Temperature Interface Spin Hall and Inverse Spin Hall Effects. *Phys. Rev. Lett.*, 116:196602, May 2016.

[13] R. J. H. Wesselink, K. Gupta, Z. Yuan, and Paul J. Kelly. Calculating spin transport properties from first principles: Spin currents. *Phys. Rev. B*, 99:144409, Apr 2019.

[14] J.H Williamson. Low-storage Runge-Kutta schemes. *Journal of Computational Physics*, 35(1):48 – 56, 1980.

[15] Yan Xu and Chi-Wang Shu. Local discontinuous Galerkin methods for nonlinear Schrödinger equations. *Journal of Computational Physics*, 205(1):72 – 97, 2005.

[16] Zhe Yuan, Kjetil M. D. Hals, Yi Liu, Anton A. Starikov, Arne Brataas, and Paul J. Kelly. Gilbert Damping in Noncollinear Ferromagnets. *Phys. Rev. Lett.*, 113:266603, Dec 2014.

[17] Maciej Zwierzycki and O. Andersen. The Overlapping Muffin-Tin Approximation. *Acta Physica Polonica Series a*, 115, 09 2008.